IS-T 1904

Analytical Chemistry at the Interface Between Materials Science and Biology

by

O'Brien, Janese C.

PHD Thesis submitted to Iowa State University

Ames Laboratory, U.S. DOE

Iowa State University

Ames, Iowa 50011-3020

Date Transmitted: September 21, 2000

PREPARED FOR THE U.S. DEPARTMENT OF ENERGY

UNDER CONTRACT NO. W-7405-Eng-82.

DISCLAIMER

Graduate College

Iowa State University

This is to certify that the Doctoral dissertation of

Janese Christine O'Brien

has meet the dissertation requirements of Iowa State University

Marc D Portt

Major Professor

Patricia A. Thiel

For the Major Program

For the Graduate College

DEDICATION

"I am not afraid of storms, for I am learning how to sail my ship."

Louisa May Alcott

TABLE OF CONTENTS

ACKNOWLEDGEMENTS

Graduate research is a journey. Often the road is ill-defined or even non-existent; at best, it is rocky and always under construction. Occasionally, human guides will give direction to the graduate traveler, advise on up-coming pitfalls and delays, and encourage when the road appears impassable. Several people have guided me through my graduate journey and I would like to acknowledge them here. Without their support and confidence in my abilities, I would have not attempted the journey, let alone completed it.

I would like to thank: Marc Porter for giving me a job when I really needed one; Dennis Johnson for convincing the admissions committee that I deserved a chance to prove myself; Brent Dawson, Jeremy Kenseth, and Jing Ni for encouraging me when things looked bleak, making me work hard to keep up with their tremendous talent, and providing their camaraderie; Dr. Chuan-Jian Zhong for his open door; Dr. Hajimie Takano and Dr. Vivian Jones for their leadership and technical expertise; Dr. David Peterson for his precious time; and Becky Staedtler for her humor in trying times.

I would like to especially thank those closest to me: my parents Ivan and Linda O'Brien for their personal sacrifices and commitment to their children's futures and finally, my husband John Stickney for believing in me when I didn't even believe in myself. I couldn't have done it without you.

This work was performed at the Microanalytical Instrumentation Center and Ames Laboratory under Contract No. W-7406-Eng-82 with the U.S. Department of Energy. The National Science Foundation under grant number BIR-9601789 provided financial support for portions of this work. The United States government has assigned the DOE Report number IS-T 1904 to this thesis.

CHAPTER 1. GENERAL INTRODUCTION

Dissertation Organization

Like all essential sciences, analytical chemistry continues to reinvent itself. Moving beyond its traditional roles of identification and quantification, analytical chemistry is now expanding its frontiers into areas previously reserved to other disciplines. This work describes several research efforts that lie at the new interfaces between analytical chemistry and two of these disciplines, namely materials science and biology. In the materials science realm, the search for new materials that may have useful or unique chromatographic properties motivated the synthesis and characterization of electrically conductive sol-gels. In the biology realm, the search for new surface fabrication schemes that would permit or even improve the detection of specific biological reactions motivated the design of miniaturized biological arrays. Collectively, this work represents some of analytical chemistry's newest forays into these disciplines.

The introduction section to this dissertation provides a literature review on several of the key aspects of this work. In advance of the materials science discussion, a brief introduction into electrochemically-modulated liquid chromatography (EMLC) and sol-gel chemistry is provided. In advance of the biological discussions, brief overviews of scanning force microscopy (SFM) and the oxidative chemistry used to construct our biological arrays are provided. This section is followed by four chapters, each of which is presented as a separate manuscript, and focuses on work that describes some of our cross-disciplinary efforts within materials science and biology. This dissertation concludes with a general summary and future prospectus.

Literature Review

The first portion of this literature review provides background information pertinent to the design and characterization of potential chromatographic stationary phase materials. Specifically, a brief description of the chromatographic technique relevant to this work is provided. Next, a brief overview of sol-gel chemistry, the synthetic route used to prepare these materials, is presented. This portion of this review concludes with background information describing key aspects of vanadium sol-gel chemistry and conductivity, areas central to our own work reported in an upcoming chapter.

Electrochemically-Modulated Liquid Chromatography (EMLC). In an attempt to reduce the multiple column nature of separations in liquid chromatography (LC), our laboratory developed a separation technique termed Electrochemically-Modulated Liquid Chromatography (EMLC).[1-8] The primary strength of this technique is its use of a single or "universal" column. In liquid chromatography, regardless of the column used, analyte retention is traditionally manipulated by making changes in the mobile phase composition. However, in EMLC, the exact opposite is done. Instead of changing the mobile phase, the stationary phase is changed via potential application. By applying an electrochemical potential to a conductive stationary phase, the properties of that stationary phase can be altered to affect a change in analyte retention. Figure 1 illustrates this effect.

In EMLC, the column is directly analogous to the working electrode in a three-electrode electrochemical cell. When an electrochemical potential equal to the PZC, or potential of zero charge, is applied to the column, the column is electrically neutral as excess charge density on the column side of the column/solution interface is equal to that on the solution side of that interface. At this potential, analytes interact with the column in a

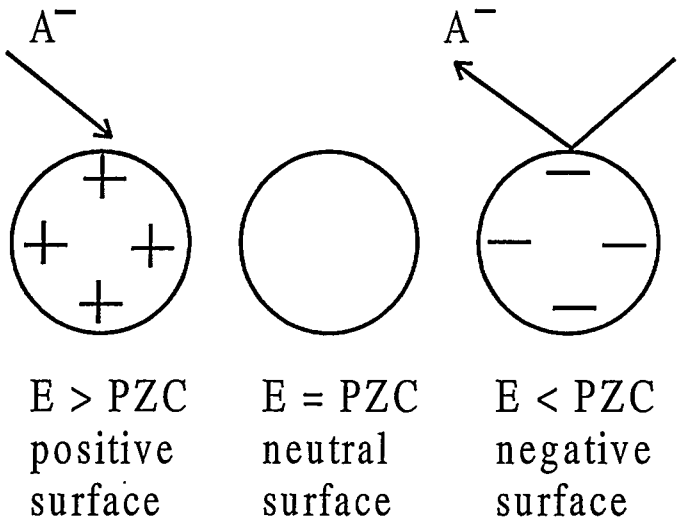

Figure 1. The retention mechanism in Electrochemically-Modulated Liquid Chromatography (EMLC)

number of modes, such as solvophobic, dipole-dipole, etc. However, when an electrochemical potential greater than the PZC is applied to the column, the column becomes positively charged. In this mode, analyte retention of electron-donating species such as an anion, for example, increases while analyte retention of an electron deficient species, such as a cation, decreases. The opposite effect can be achieved by applying a potential less than the PZC to the column. In this scenario, the retention of an electron-donating species is decreased while that of an electron deficient species is enhanced. While this is an admittedly simple interpretation of EMLC separations, numerous investigations are currently underway in our laboratory to further elucidate the separation mechanism(s) operating in this technique. Nevertheless, our laboratory has successfully separated a large number of compounds by EMLC including alkanes, amino acids, priority pollutants such as polycyclic aromatic hydrocarbons (PAHs), and inorganic ions.

The stationary phase currently used in our laboratory is porous graphitic carbon

(PGC). While this material has been used successfully to separate a wide range of compounds, current research efforts are underway to develop alternative materials that may have unique or useful separating properties. The synthetic route that we are currently pursuing to create these alternative materials is sol-gel processing. The next portion of this section will discuss the chemistry behind this technology.

Sol-Gel Chemistry. Sol-gel chemistry is a rich and extremely diverse field of synthesis that has been used to create micrometer size spheres,[9] powders,[10] films,[11] catalytic supports[12] and sensors,[13] fiber optics,[14] and coatings,[15] just to name a few examples. Sol-gel chemistry involves the acid or base catalyzed hydrolysis and condensation of precursor molecules to ultimately form porous ceramic and glass materials. Figure 2 illustrates traditional silicon-based sol-gel chemistry.

During hydrolysis, one or more of the alkoxy groups in the precursor molecule is replaced by hydroxyl groups to create silanol functionalities. During condensation, siloxane bonds are formed from silanol functionalities; water and alcohol are by-products of the reaction. By carefully choosing the starting material, catalyst, water content, and drying conditions, materials can be created that possess the desired degree of porosity, hydrophobicity, chemical reactivity or inertness.

Traditional precursors in sol-gel chemistry are alkoxy silane materials and, in fact, sol-gel materials derived from such precursors have already been used as stationary phases for open tubular reverse phase liquid chromatography and open tubular electrokinetic chromatography.[16] Here, C_8 and C_{18} functionalized alkoxy silanes have been used to mimic the hydrophobicity and retention properties of more traditional packing materials constructed from non sol-gel routes. Successful separations of aromatic hydrocarbons have been

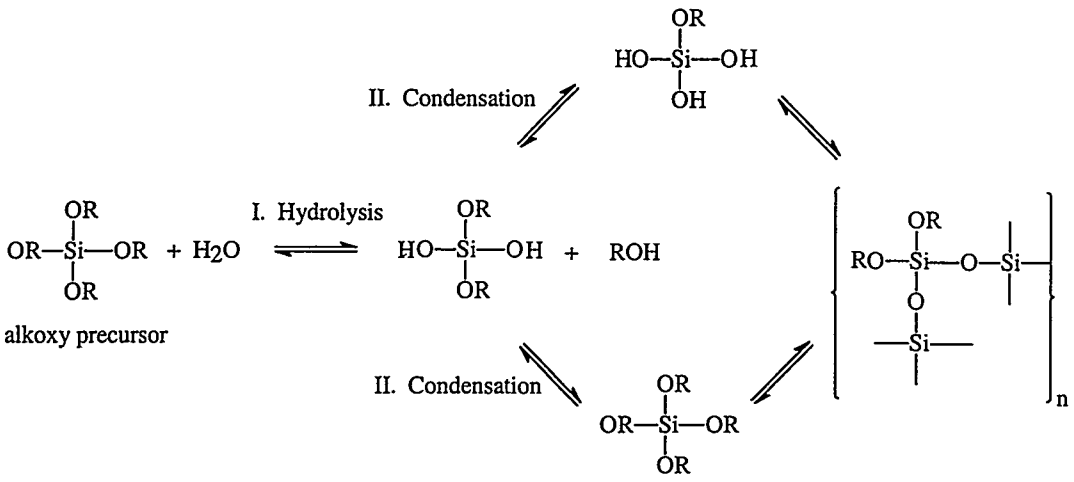

Figure 2. Overview of sol-gel chemistry

performed[17] using these sol-gel columns and in some systems, sol-gel columns appear to have comparable if not superior reproducibility, resolution, and efficiency to columns constructed from more traditional stationary phase materials.

It is important to note that the sol-gel stationary phases used in the techniques mentioned above cannot be used in EMLC because silicon-based sol-gels are electrical insulators. EMLC stationary phases must be electrically conductive, thereby requiring the use of a metal-based sol-gel system. Current research efforts into the construction of electrically conductive sol-gels are focusing vanadium-based materials. The following paragraphs of this section discuss the motivation behind the use of vanadium-based materials and the factors that influence their electrical conductivity.

Vanadium Sol-Gels. The preparation and characterization of electrically conductive sol-gel materials have recently become active areas of research in sol-gel chemistry and a

significant number of reports on this subject have appeared in the scientific literature during the last several years. Electrically conductive sol-gels have been created from antimony-doped tin oxide,[18] niobium pentoxide,[19] cobalt oxides,[20] ruthenium and titanium dioxides,[21] cesium and titanium oxides,[22] zirconium, scandium, and lanthanide oxides,[23] and vanadium oxides.[24-37] As these references demonstrate, precedence for the creation of these materials exists in the literature.

In our laboratory, preliminary investigations into the creation of electrically conductive sol-gels are focusing on vanadium-based materials. Vanadium was chosen as a starting point for research for four reasons. First, preparation strategies for the creation of vanadium sol-gel are extensively reported in the literature. Second, vanadium sol-gels have a rich intercalation chemistry. For example, vanadium sol-gels have been known to intercalate alkyl amines,[38] charge transfer complexes such as tetrathiofulvalene,[39] and inorganic cations.[40] It follows, then, that vanadium sol-gel stationary phases may prove to useful in separating these types of compounds. Third, the conductivity of vanadium sol-gels, ranging from semiconductor regime to the metallic regime, has been well characterized in the literature. Finally, vanadium alkoxy precursors are commercially available, an attribute that makes the creation of vanadium-based materials attractive. For these reasons, among others, vanadium sol-gels have been widely used as anti-static coatings,[41] humidity sensors,[41] liquid crystals,[31] cathodes,[37] oxidation catalysts,[42] and even glucose biosensors.[26]

The conductivity of vanadium sol-gels is strongly dependent upon several factors, including vanadium-to-oxygen stoichiometry, oxidation state of the vanadium centers, and water content. Each one of these factors will be briefly introduced below to provide a rational for the vanadium sol-gel preparation strategies that will presented in a subsequent

data chapter.

Vanadium forms numerous oxide phases[43,44] ranging from the fully oxidized pentoxide, V_2O_5, to the monooxide, VO. Furthermore, the conductivity of the oxides varies greatly. For example, vanadium pentoxide is an n-type semiconductor[45] with a band gap of approximately 2 eV,[46] whereas vanadium monooxide exhibits metallic conductivity.[47] Therefore, sol-gel preparation strategies that favor formation of high vanadium-to-oxygen stoichiometries will be employed.

In addition to oxide stoichiometry, the oxidation state of vanadium within vanadium sol-gels also affects the conductivity (σ) of these materials. This dependence is particularly well documented in the case of vanadium pentoxide. The electrical conductivity in V_2O_5 arises via a polaron hopping from a vanadium center of lower oxidation state, typically 4^+, to a completely oxidized vanadium center in the 5^+ oxidation state. In these materials, the higher the vanadium 4^+ content, the more conductive the material. For example, a vanadium xerogel with a V(IV) of 1%, $\sigma = 4 \times 10^{-5}\ \Omega^{-1}\ cm^{-1}$. However, when V(IV) is 10%, $\sigma = 3 \times 10^{-3}\ \Omega^{-1}\ cm^{-1}$.[48] Here, a one order of magnitude increase in V(IV) results in an approximate two order of magnitude increase in conductivity. Therefore, preparation strategies that preserve or even enhance reduced oxidation states of vanadium are important.

In addition to oxide stoichiometry and the amount of vanadium in the 4^+ oxidation state, the water content of vanadium sol-gels is also an extremely important parameter affecting the conductivity of these materials. When dried in the laboratory ambient, vanadium sol-gels contain intercalated water molecules within its layered structure. When the material is heated, the water separating the layers is removed and the conductivity of the

material is enhanced most likely due to the formation of V-O-V bonds between layers.[30] Therefore, the preparation strategies pursued in an upcoming data chapter will involve a drying step.

To summarize, sol-gel chemistry can be used to create electrically conductive materials, the conductivity of which is dependent upon several factors including the vanadium-to-oxygen stoichiometry, the oxidation state of the vanadium center, and water content. Manipulation of each of these parameters is possible and allows the creation of a material with the desired conductivity.

The final portion of this literature review provides background information pertinent to the interrogation and fabrication of miniaturized biological arrays. Specifically, an overview of scanning force microscopy (SFM), the primary tool used to interrogate the biological surfaces presented in future data chapters, is given. Next, a brief overview of the chemistry used to construct arrays amenable to interrogation by SFM is presented. Finally, this section will introduce the use of the topographic imaging capabilities of SFM to perform height-based chemical and biochemical analysis. This section will then conclude with a dissertation overview and references.

Scanning Force Microscopy (SFM). The introduction of the atomic force microscope (AFM), also known as the scanning force microscope (SFM), in 1986 by Binnig, Quate, and Gerber[49] has revolutionized the field of surface science. SFM and its numerous variations have been used to measure interaction forces between single molecules,[50-54] map the chemical composition of surfaces,[55-59] and to image the topography of DNA[60-65] and its complexes[66-68] with a degree of resolution unimaginable only about a decade ago.

A SFM consists of four major components: a cantilever-mounted tip, a piezoelectric

micropositioner, a cantilever deflection sensor, and an electrical feedback mechanism for the micropositioner. The most popular mode of detecting cantilever deflection, which is depicted in an instrument schematic in Figure 3, uses an optical lever and a quadrant, position-sensitive photodiode. This detection system can be used to follow the normal displacement (vertical motion) and the torsion (lateral motion) of the cantilever simultaneously.

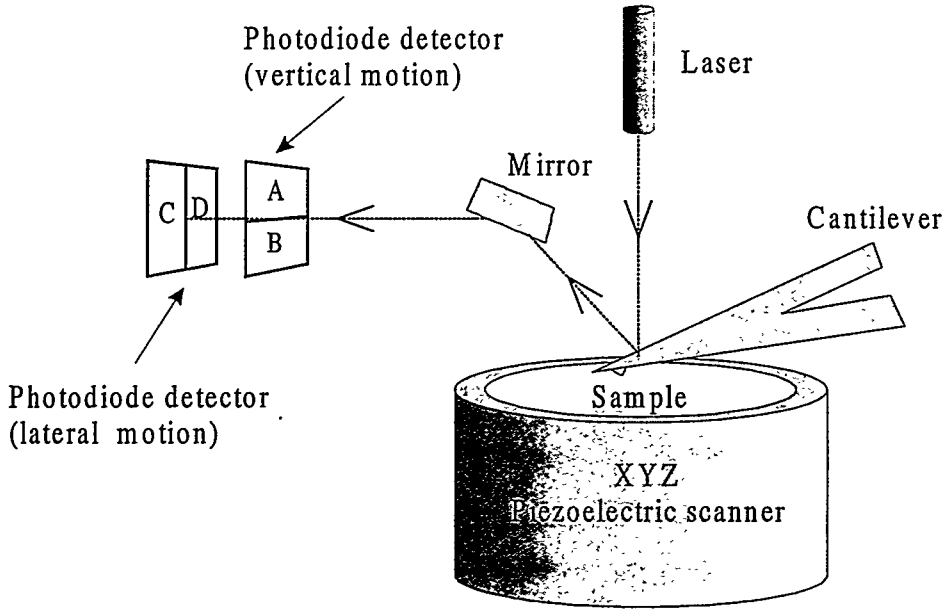

Figure 3. The components of an optical lever scanning force microscope

In Figure 4, a scanning electron micrograph of a commercially available, microfabricated silicon nitride (Si_3N_4) cantilever with a pyramidal tip is shown. Since normal spring constants (k_N) for cantilevers are 0.01-100 N/m and instrumental sensitivities for normal deflection are ~0.01 nm, the corresponding limits in force detection are 10^{-13}-10^{-8} N.[69] These limits reflect a combination of the thermal excitation of the cantilever

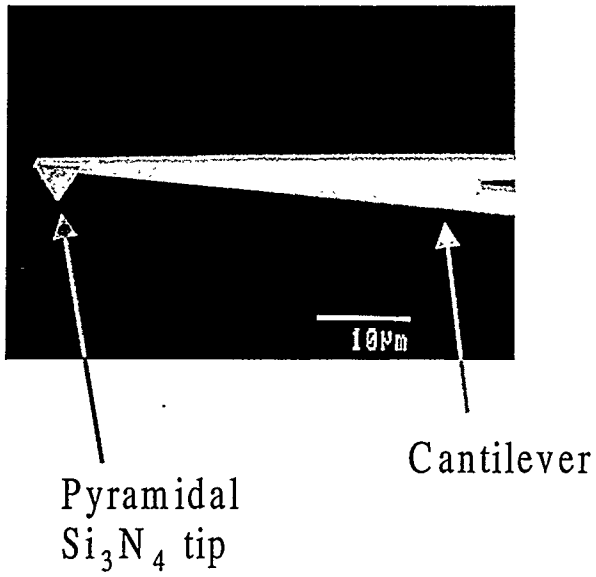

Figure 4. A scanning electron micrograph of a commercially available Si_3N_4 cantilever

as well as optical and electrical noise.

SFM can be operated in various modes. The most popular instrumental mode of SFM is the contact mode where the tip is brought into physical contact with the sample. The micropositioners are slaved to the feedback electronics in order to maintain a preset imaging parameter (e.g., force) that is monitored by the vertical deflection sensor while the sample is scanned under the tip, or vice versa. Two-dimensional plots of the feedback signal are then used to develop a topographic image of the sample. A map of surface composition, for example, can be constructed if there are differences in topography that can be directly correlated with compositional and/or other structural expectations.

Although contact mode SFM has been used extensively for chemical mapping analysis, there are occasions where lower imaging forces, such as in the characterization of soft biological and polymer materials, are required. That is, highly compliant samples may

be destructively and therefore unreliably imaged at the shear forces operative in contact mode imaging. Tapping mode SFM (TM-SFM) reduces this problem by periodically "tapping" the surface with the tip as the sample is translated under the tip.[70-72] In this mode, the oscillation of the cantilever is driven at or near its resonant frequency via a piezoelectric crystal. The changes in oscillation amplitude during scanning are used to map topography. Moreover, the phase changes of the oscillation during a scan can be recorded as phase images that are related to variations in adhesion, friction, and/or viscoelasticity.[72-74]

The next portion of this literature review will discuss a particular strategy employed in subsequent data chapters to control the chemical landscape of surfaces. This strategy, based on the photooxidation of alkanethiolate monolayers on gold, is very amenable to interrogation by SFM. Here, a brief overview of the pertinent chemistry will be provided as well as a description of the use of SFM to perform height-based analysis.

Photopatterning of Alkanethiolate Monolayers on Gold. An important issue when preparing substrates for chemical analysis by SFM is the design of the chemical landscape. Techniques that provide for the control over the placement or delivery of chemical reagents and calibration standards onto discrete regions of a surface are critical. Ideally, this localization would be done within the typical scan area of SFM so that both reaction and calibration information can be gained in a single scan.

One method that provides for localization is photolithography. Photolithography involves the irradiation of a surface comprised of photolabile groups through a photomask, which chemically transforms the irradiated areas and results in a compositionally-patterned surface. One of the more popular photolithographic systems in this area involves the photooxidation of alkanethiolate monolayers on gold.[75-77] Figure 5 represents the ideal

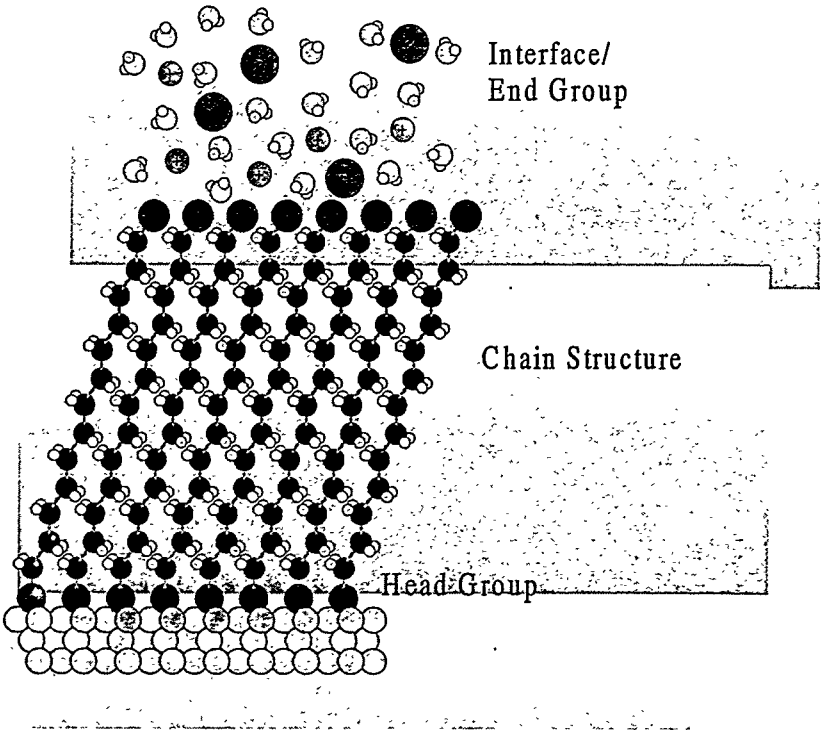

Figure 5. Idealized representation of an alkanethiolate monolayer on Au(111)
Reproduced from ref. 82

structure of these monolayers on gold. There are effectively three regions to the monolayer film: 1) the adsorbate-substrate interface; 2) adsorbate; and 3) the adsorbate-environment interface.

The portion of the monolayer most pertinent to photolithography is the adsorbate-substrate interface. Chemisorption of organosulfur precursors onto gold results in the formation of a thiolate bond, the strength of which is ~40 kcal/mol.[78-80] Thus, these surfaces are relatively robust and stable. With this system, ultraviolet radiation in the presence of oxygen converts the gold-bound thiolate to various oxygenated forms of sulfur (e.g., RSO_3^-).[81] These oxygenated forms of sulfur weakly adhere to gold and are readily

rinsed from the surface with many organic solvents, such as ethanol, acetone, or tetrahydrofuran.

We have used transmission electron microscopy (TEM) grids as masks, where the mesh size of the grid defines the size and shape of the irradiated area. For example, irradiation of an octadecanethiolate (ODT) modified gold surface through a 2000 mesh grid followed by ethanol rinsing creates bare gold squares 7.5 μm x 7.5 μm in dimension that are surrounded by intact ODT grids 5.0 μm wide.[83] These exposed gold squares can then be back-filled with an alkanethiol that has a different terminal group (e.g., a terminal group that can function as a coupling agent), thereby providing spatial control over the placement of reactants on a surface.

Using the photopatterning of alkanethiol monolayers on gold, our group has recently demonstrated the ability of SFM to conduct height-based immunoassays in situ and in real-time using compositionally patterned antigen arrays.[83] Substrates composed of micrometer-sized square regions of antigen addresses were prepared by reacting rabbit IgG to a gold-bound coupling agent. These antigen-modified addresses were separated by grid regions that were composed of a hydrophobic octadecanethiolate monolayer. The addition of Tween 80 surfactant to the buffer solution upon the addition of goat anti-rabbit IgG antibody resulted in the strong minimization of nonspecific protein adsorption to the grid regions. This absence allowed the grid regions to function as an internal reference plane for the increase in height observed upon antigen-antibody binding in buffer solution. An approximate doubling in height of the antigen-modified regions from ~4 nm to ~8 nm occurred upon addition of antibody, consistent with the formation of a single antigen-antibody layer. Addition of a nonspecific antibody (e.g. goat anti-bovine IgG) to the antigen arrays did not result in a

subsequent height increase. Real-time monitoring revealed that the increase in height was complete in ~5 min, consistent with earlier antigen-antibody binding studies.[84]

The work described in three upcoming chapters expands the use of the SFM height-based assay. Specifically, Chapter 3 describes the use of the SFM probe tip to detect increases in height consistent with the binding of a solution antibody to an antigenic surface comprised of antibody fragments. Chapters 4 and 5 describe the use of the SFM probe tip to detect height decreases consistent with the sequence specific cleavage of immobilized oligonucleotides by a restriction enzyme in solution.

To summarize, SFM and its variants have proven invaluable to the study of interfacial structure and chemical phenomena. Moreover, the photopatterning of alkanethiolate monolayers on gold permits the placement of reactants and calibration standards within a single SFM scan, thereby allowing a degree of control over the chemical architecture of surfaces. Together, these techniques allow for the topographic imaging of surfaces, a new diagnostic tool capable of evaluating specific chemical and biochemical interactions.

Dissertation Overview

Centered on the main themes presented above, the body of this dissertation is divided into four data chapters. Each chapter is presented as a separate manuscript. Chapter 2 describes the synthesis and characterization of electrically conductive sol-gels derived from the acid-catalyzed hydrolysis of a vanadium alkoxide. In addition to conductivity data, results from characterizations using infrared spectroscopy, X-ray diffraction, and X-ray photoelectron spectroscopy will presented. Chapter 3 reports the construction of novel antigenic immunosensing platforms of increased epitope density using antibody fragments.

Here, X-ray photoelectron spectroscopy (XPS), thin-layer cell (TLC) and confocal fluorescence spectroscopies, and scanning force microscopy (SFM) are employed to characterize the fragment-substrate interaction, to quantify epitope density, and to demonstrate fragment viability and specificity. Chapter 4 introduces a novel fabrication scheme for the production of double-stranded DNA (dsDNA) microarrays suitable for screening specific protein:dsDNA interactions using scanning force microscopy (SFM). The restriction enzyme *ECo*R1 is used as a model protein for this investigation. Chapter 5 explores more fully the microarray fabrication process described in Chapter 4. Specifically, experiments characterizing the effect of oligonucleotide topography on deposition conditions as well as array density are presented. Chapter 6 presents general conclusions regarding the work presented in this dissertation and speculates on its extension.

References

(1) Deinhammer, R. S.; Ting, E. Y.; Porter, M. D. *J. Electroanal. Chem.* **1993**, *362*, 295.

(2) Deinhammer, R. S.; Ting, E. Y.; Porter, M. D. *Anal. Chem.* **1995**, *67*, 237.

(3) Ting, E.-Y.; Porter, M. D. *Anal. Chem.* **1997**, *69*, 675.

(4) Ting, E.-Y.; Porter, M. D. *J. Electroanal. Chem.* **1998**, *443*, 180.

(5) Ting, E.-Y.; Porter, M. D. *J. Chromatogr. A* **1998**, *793*, 204.

(6) Ting, E.-Y.; Porter, M. D. *Anal. Chem.* **1998**, *70*, 94.

(7) Ho, M.; Wang, S.; Porter, M. D. *Anal. Chem.* **1998**, *70*, 4314.

(8) Wang, S.; Porter, M. D. *J. Chromatogr. A* **1998**, *828*, 157.

(9) Ziemath, E.; Aegerter, M. A.; Moreira, J.; Figueiredo, M.; Zarzycki, J. In *Better Ceramics through Chemistry III*; Brinker, C. J., Clark, D. E., Ulrich, D. R., Eds.; Materials Research Society: Pittsburgh, 1988; p 311.

(10) Ayral, A.; Phalippou, J.; Droguet, J. C. In *Better Ceramics through Chemistry III*; Brinker, C. J., Clark, D. E., Ulrich, D. R., Eds.; Materials Research Society: Pittsburgh, 1988; p 239.

(11) Scriven, L. E. In *Better Ceramics through Chemistry III*; Brinker, C. J., Clark, D. E., Ulrich, D. R., Eds.; Materials Research Society: Pittsburgh, 1988; p 717.

(12) Pommier, B.; Teichner, S. J. *Proc. Int. Congr. Catal.* **1988**, *2*, 610.

(13) Ochoa, R.; Miranda, R. In *Better Ceramics through Chemistry VI*; Cheetham, A. K., Brinker, C. J., Mecartney, M. L., Sanchez, C., Eds.; Materials Research Society: Pittsburgh, 1994; p 553.

(14) L'Esperance, D.; Browne, C. A.; Chronister, E. L. In *Better Ceramics through Chemistry VI*; Cheetham, A. K., Brinker, C. J., Mecartney, M. L., Sanchez, C., Eds.; Materials Research Society: Pittsburgh, 1994; p 579.

(15) Nazeri-Eshghi, A.; Mackenzie, J. D.; Yang, J. M. In *Better Ceramics through Chemistry III*; Brinker, C. J., Clark, D. E., Ulrich, D. R., Eds.; Materials Research Society: Pittsburgh, 1988; p 561.

(16) Guo, Y.; Colon, L. A. *Anal. Chem.* **1995**, *67*, 2511.

(17) Fields, S. M. *Anal. Chem.* **1996**, *68*, 2709.

(18) Gonzalez-Oliver, C. J. R.; Kato, I. *J. Non-Cryst. Solids* **1986**, *82*, 400.

(19) Ozer, N.; Barreto, T.; Buyuklimanli, T.; Lampert, C. M. *Sol. Energy Mater. Sol. Cells* **1995**, *36*, 433.

(20) Spinolo, G.; Ardizzone, S.; Trasatti, S. *J. Electroanal. Chem.* **1997**, *423*, 49.

(21) Swider, K. E.; Merzbacher, C. I.; Hagains, P. L.; Rolison, D. R. *Chem. Mater.* **1997**, *9*, 1248.

(22) Tavcar, G.; Kalcher, K.; Ogorevc, B. *Analyst* **1997**, *122*, 371.

(23) Yamaji, A.; Ishii, T.; Kanzaki, M. In *Better Ceramics through Chemistry VI*; Cheetham, A. K., Brinker, C. J., Mecartney, M. L., Sanchez, C., Eds.; Materials Research Society: Pittsburgh, 1994; p 335.

(24) Baddour, R.; Pereira-Ramos, J. P.; Messina, R.; Perichon, J. *J. Electroanal. Chem.* **1990**, *277*, 359.

(25) Gharbi, R. C.; Ballutaud, D.; Michaud, M.; Livage, J.; Audiere, J. P.; Schiffmacher, G. *J. Non-Cryst. Solids* **1981**, *46*, 247.

(26) Glezer, V.; Lev, O. *J. Am. Chem. Soc.* **1993**, *115*, 2533.

(27) Hirashima, H.; Tsukimi, K.; Muratake, R. In *Ultrastructure Processing of Advanced Materials*; Uhlmann, D. R., Ulrich, D. R., Eds.; John Wiley & Sons, Inc.: New York, 1992; p 285.

(28) Kamiyama, T.; Itoh, T.; Suzuki, K. *J. Non-Cryst. Solids* **1988**, *100*, 466.

(29) Livage, J. *Prog. Solid State Chem.* **1988-1989**, *18-19*, 259.

(30) Livage, J. In *Better Ceramics through Chemistry*; Brinker, C. J., Clark, D. E., Ulrich, D. R., Eds.; Elsevier Science Publishing Company Inc.: New York, 1984; p 125.

(31) Livage, J.; Baffier, N.; Pereira-Ramos, J. P.; Davidson, P. In *Solid State Ionics IV*; Nazri, G.-A., Tarascon, J.-M., Schreiber, M., Eds.; Materials Research Society: Pittsburgh, 1995; p 179.

(32) Miyahara, H.; Kittaka, S. *Bull. Hiruzen Res.* **1992**, *18*, 1.

(33) Morales, E.; Acosta, J. L. *Solid State Ionics* **1997**, *95*, 269.

(34) Muller, Z. *Kolloides* **1911**, *8*, 302.

(35) Saidi, M. Y.; Olsen, I. I.; Koksbang, R.; Barker, J.; Pynenburg, R.; West, K.; Zachau-Christiansen, B.; Skaarup, S. In *Solid State Ionics IV*; Nazri, G.-A., Tarascon, J.-M., Schreiber, M., Eds.; Materials Research Society: Pittsburgh, 1995; p 201.

(36) Sanchez, C.; Nabavi, M.; Taulelle, F. In *Better Ceramics through Chemistry III*; Brinker, C. J., Clark, D. E., Ulrich, D. R., Eds.; Materials Research Society: Pittsburgh, 1988; p 93.

(37) West, K.; Zachau-Christiansen, B.; Ostergard, M. J. L.; Jacobsen, T. *J. Power Sources* **1987**, *20*, 165.

(38) Aldebert, P.; Baffier, N.; Legendre, J.-J.; Livage, J. *Rev. Chim. Miner.* **1982**, *19*, 485.

(39) Damme, H. V.; Letellier, M.; Tinet, D.; Kihal, B.; Erre, R. *Mater. Res. Bull.* **1984**, *19*, 1635.

(40) Aldebert, P.; V. Paul-Boncour *Mater. Res. Bull.* **1983**, *18*, 1263.

(41) Livage, J. *Chem. Mater.* **1991**, *3*, 578.

(42) Gasser, D.; Baiker, A. *J. Catal.* **1988**, *113*, 325.

(43) Gupta, C. K.; Krishnamurthy, N. *Extractive Metallurgy of Vanadium*; Elsevier: Amsterdam, 1992, p 384.

(44) Kachi, S.; Kosuge, K.; Okinaka, H. *J. Solid State Chem.* **1973**, *6*, 258.

(45) Gharbi, R. C.; Ballutaud, D.; Michaud, M.; Audiere, J. P.; Schiffmacher, G. *J. Non-Cryst. Solids* **1981**, *46*, 247.

(46) Bullot, J.; Cordier, P.; Gallais, O.; Gauthier, M.; Livage, J. *J. Non-Cryst. Solids* **1984**, *68*, 123.

(47) Gupta, C. K.; Krishnamurthy, N. *Extractive Metallurgy of Vanadium*; Elsevier: New York, 1992, p 389.

(48) Livage, J.; Barboux, P.; Badot, J. C.; Baffier, N. In *Better Ceramics through Chemistry III*; Brinker, C. J., Clark, D. E., Ulrich, D. R., Eds.; Materials Research Society: Pittsburgh, 1988; p 167.

(49) Binnig, G.; Quate, C. F.; Gerber, C. *Phys. Rev. Lett.* **1986**, *56*, 930.

(50) Hoh, J. H.; Cleveland, J. P.; Prater, C. B.; Revel, J.-P.; Hansma, P. K. *J. Am. Chem. Soc.* **1992**, *114*, 4917.

(51) Han, T.; Williams, J. M.; Beebe, Jr., T.P. *Anal. Chim. Acta* **1995**, *307*, 365.

(52) Williams, J. M.; Han, T.; Beebe, Jr., T.P. *Langmuir* **1996**, *12*, 1291.

(53) Wenzler, L. A.; Moyes, G. L.; Olson, L. G.; Harris, J. M.; Beebe, Jr., T.P. *Anal. Chem.* **1997**, *69*, 2855.

(54) Wenzler, L. A.; Moyes, G. L.; Raikar, G. N.; Hansen, R. L.; Harris, J. M.; Beebe, Jr., T.P. Wood, L. L.; Saavedra, S. S. *Langmuir* **1997**, *13*, 3761.

(55) Green, J.-B. D.; McDermott, M. T.; Porter, M. D.; Siperko, L. M. *J. Phys. Chem.* **1995**, *99*, 10960.

(56) Hayes, W. A.; Kim, H.; Yue, X.; Perry, S.; Shannon, C. *Langmuir* **1997**, *13*, *2511*.

(57) Lio, A.; Charych, D. H.; Salmeron, M. *J. Phys. Chem. B* **1997**, *101*, 3800.

(58) Overney, R. M.; Meyer, E.; Frommer, J.; Brodbeck, D.; Luthi, R.; Howald, L.; Guntherodt, H.-J.; Fujihira, M.; Takano, H.; Gotoh, Y. *Nature* **1992**, *359*, 133.

(59) Vezenov, D. V.; Noy, A.; Rozsnyai, L. F.; Lieber, C. M. *J. Am. Chem. Soc.* **1997**, *119*, 2006.

(60) Clemmer, C. R.; Beebe, Jr., T.P. *Science* **1991**, *251*, 640.

(61) Weisenhorn, A. L.; Gaub, H. E.; Hansma, H. G.; Sinsheimer, R. L.; Kelderman, G. L.; Hansma, P. K. *Scanning Microsc.* **1990**, *4*, 511.

(62) Hansma, H. G.; Sinsheimer, R. L.; Gould, S. A. C.; Weisenhorn, A. L.; Gaub, H. E.; Hansma, P. K. AIP Conference Proceedings, Santa Barbara, CA, 1991.

(63) Hansma, H. G.; Vesenka, J.; Siegerist, C.; Kelderman, G.; Morrett, H.; Sinsheimer, R. L.; Elings, V.; Bustamante, C.; Hansma, P. K. *Science* **1992**, *256*, 1180.

(64) Hansma, H. G.; Pietrasanta, L. *Curr. Opin. Chem. Biol.* **1998**, *2*, 579.

(65) Hansma, H. G. *J. Vac. Sci. Technol. B* **1996**, *14*, 1390.

(66) Hansma, H. G.; Bezanilla, M.; Nudler, E.; Hansma, P. K.; Hoh, J.; Kashlev, M.; Firouz, N.; Smith, B. L. *Probe Microsc.* **1998**, *1*, 127.

(67) Allison, D. P.; Kerper, P. S.; Doktycz, M. J.; Thundat, T.; Modrich, P.; Larimer, F. W.; Johnson, D. K.; Hoyt, P. R.; Mucenski, M. L.; Warmack, R. J. *Genomics* **1997**, *41*, 379.

(68) Bezanilla, M.; Drake, B.; Nudler, E.; Kashlev, M.; Hansma, P. K.; Hansma, H. G. *Biophys. J.* **1994**, *67*, 2454.

(69) Burnham, N. A.; Colton, R. J. In *Scanning Tunneling Microscopy and Spectroscopy*; Bonnell, D. A., Ed.; VCH Publisher, Inc.: New York, 1993; p 191.

(70) Magonov, S. N.; Reneker, D. H. *Annu. Rev. Mater. Sci.* **1997**, *27*, 175.

(71) Noy, A.; Sanders, C. H.; Vezenov, D. V.; Wong, S. S.; Lieber, C. M. *Langmuir* **1998**, *14*, 1508.

(72) Finot, M. O.; McDermott, M. T. *J. Am. Chem. Soc.* **1997**, *119*, 8564.

(73) Whangbo, M.-H.; Bar, G.; Brandsch, R. *Surf. Sci.* **1998**, *411*, L794.

(74) Magonov, S. N.; Eling, V.; Whangbo, M.-H. *Surf. Sci.* **1997**, *375*, L385.

(75) Huang, J.; Hemminger, J. C. *J. Am. Chem. Soc.* **1993**, *115*, 3342.

(76) Tarlov, M. J.; Burgess, Jr., D.R.F.; Gillen, G. *J. Am. Chem. Soc.* **1993**, *115*, 5305.

(77) Lewis, M.; Tarlov, M. *J. Am. Chem. Soc.* **1995**, *117*, 9574.

(78) Ulman, A. *An Introduction to Ultrathin Organic Films from Langmuir-Blodgett to Self-Assembly*; Academic Press: San Diego, 1991.

(79) Finklea, H. O. In *Electroanalytical Chemistry*; Bard, A. J., Ed.; Marcel Dekker Inc.: New York, 1996; Vol. 19; p 109.

(80) Nuzzo, R. G.; Zegarski, B. R.; Dubois, L. H. *J. Am. Chem. Soc.* **1987**, *109*, 733.

(81) Zhang, Y.; Terrill, R.; Tanzer, T.; Bohn, P. *J. Am. Chem. Soc.* **1998**, *120*, 2654.

(82) Green, J.-B. D. Ph.D. Dissertation, Iowa State University, 1996.

(83) Jones, V. W.; Kenseth, J. R.; Porter, M. D.; Mosher, C. L.; Henderson, E. *Anal. Chem.* **1998**, *70*, 1233.

(84) Browning-Kelley, M. E.; Wadu-Mesthrige, K.; Hari, V.; Liu, G. Y. *Langmuir* **1997**, *13*, 343.

CHAPTER 2. THE EFFECT OF ACID AND DRYING CONDITIONS ON THE CONDUCTIVITY OF VANADIUM SOL-GELS DERIVED FROM THE ACID-CATALYZED HYDROLYSIS OF A VANADIUM ALKOXIDE

A manuscript in preparation for submission to *Chemistry of Materials*

Janese C. O'Brien,[1] David T. Peterson,[2,3] and Marc D. Porter[1,4]

ABSTRACT

We report herein our attempts to increase the electrical conductivity of vanadium sol-gels derived from the acid-catalyzed hydrolysis of tri-n propoxide vanadium oxide by manipulating the acidic and drying conditions used during processing. We observed that the identity and concentration of acid used to initiate hydrolysis had a significant impact on conductivity. We theorize that several factors are responsible for this observation, including redox chemistry, the extent of hydrolysis of alkoxy side chains within the alkoxide precursor, and trace level impurities. In addition, the conductivity of vanadium sol-gels is dependent upon the heating conditions used to remove both physisorbed and chemisorbed water and those used to create materials of higher vanadium-oxygen stoichiometry. Specifically, the conductivity of vanadium sol-gels can be increased ~18,000 times by controlling carefully the heating conditions used during processing. In addition to four-probe conductivity data, results from characterizations using infrared spectroscopy, X-ray diffraction, and X-ray photoelectron spectroscopy will be described.

---

[1] Microanalytical Instrumentation Center, Ames Laboratory-DOE, and Department of Chemistry, Iowa State University, Ames, IA 50011
[2] Materials Preparation Center, Ames Laboratory-DOE, Iowa State University, Ames, IA 50011
[3] Deceased
[4] Corresponding Author

INTRODUCTION

Sol-gel chemistry is a diverse field of synthesis that has been exploited to create micrometer size spheres,[1] powders,[2] films,[3] catalytic supports[4] and sensors,[5] fiber optics,[6] and coatings,[7] just to name a few examples. Sol-gel chemistry involves the acid- or base-catalyzed hydrolysis and condensation of chemical precursors to form ultimately porous ceramics and glasses. Traditional precursors in sol-gel chemistry are silicon-based materials. In recent years, however, sol-gels derived from transition metal systems have been explored in a variety of fields. Unlike their silicon counterparts, sol-gels based on some transition metals are electrically conductive, including those created from antimony-doped tin oxide,[8,9] niobium pentoxide,[10] cobalt oxide,[11] ruthenium and titanium dioxides,[12] cesium and titanium oxides,[13] and vanadium oxides.[8,14-29] Sol-gels derived from vanadium oxides have been used as anti-static coatings,[30] humidity sensors,[30] liquid crystals,[31] cathodes,[32] glucose biosensors,[21] and oxidation catalysts.[15,33,34]

Our efforts to create electrically conductive sol-gel materials have focused on the acid-catalyzed hydrolysis of vanadium alkoxides, specifically tri-n propoxide vanadium oxide, in an attempt to create an electrochemically stable host material for the encapsulation of redox transformable species. Vanadium-based sol-gels were chosen because of their well-established conductivity[16,17,19,26,35] and rich intercalation chemistry,[18,36-44] attributes hypothesized to be of importance for our intended purpose. This paper reports our attempts to increase the conductivity of vanadium sol-gels by optimizing the acidic and drying conditions used during synthesis. While numerous reports on the creation of vanadium sol-gels by other synthetic routes (e.g., quick quenching or splat-cooling of molten V_2O_5[45-47]

and the polymerization of decavanadate acid prepared from vanadium salts[19,27,48-51]) have appeared, only a few deal with the properties of vanadium sol-gels derived from alkoxide precursors.[14,22,23,33,34,52-55] To our knowledge, the results herein are the first report on the effect of acidity on the conductivity of vanadium sol-gels derived from alkoxide precursors.

EXPERIMENTAL

Chemicals. Tri-n propoxide vanadium oxide was purchased from Gelest and the vanadium oxides V_2O_5 and V_2O_4 were purchased from Aldrich. All acids (ACS reagent grade) and n-propanol (HPLC-grade) were purchased from Fisher. All chemicals were used as received. Water was purified with a Millipore Mili-Q water system.

Sol-Gel Preparation. In a typical experiment, 1 mL of the vanadium alkoxide and 1 mL of n-propanol (n-PrOH) were mixed in a 20 mL scintillation vial. In a second vial, 1 mL of purified water and the desired amount of strong acid (if used) were mixed. The molar ratios of alkoxide:H_2O:n-PrOH are 1:12.6:3. The aqueous solution was then added dropwise to the alkoxide-alcohol mixture with vigorous swirling. Immediately upon addition, the portion of the alkoxide-alcohol mixture contacted by the aqueous mixture turned into a bright red viscous gel that subsequently turned into a dark red opaque solid within a few hours. The sample was then dried in the laboratory ambient for varying periods of time. Typically, a sample would turn dark green after ~2 days of drying and then dark blue or black ~2 days later. This color transition from red to dark green to blue or black is very characteristic of a reduction in the oxidation state of the vanadium centers within the sol-gel.[50,55]

Instrumentation. A horizontal tube furnace attached to a vacuum manifold line was used to heat all sol-gel samples. After ambient drying for a desired length of time, samples were ground using an agate mortar and pestle and placed into quartz crucibles that were then inserted into a quartz reaction tube. The tube was then evacuated to <1 mTorr and subsequently filled to ~500 Torr with the desired gas.

The conductivity of the resulting powders was determined using the home-built device illustrated in Figure 1. The device is designed to operate like a four-point probe in that the voltage drop across a fixed distance (l) of the sample is measured as a function of applied current. The device consists of a plexiglass tube threaded on both ends to accommodate brass screws which, when inserted into the tube, are separated by a gap of 0.40 cm. Two platinum wires (99.9%, diameter 0.25 mm, Aldrich) are inserted ~2 mm into this gap via holes drilled perpendicular to the long axis of the tube. The wires are separated by 2.0 mm and are held firmly in position with epoxy.

For the conductivity determinations, the sol-gel is first ground into a powder using an agate mortar and pestle. With one screw threaded into the tube, the powder is inserted into the open side of the tube and then pressed into a small pellet as the second screw is threaded into the tube. The surface area (A_s) of a screw contacting the pellet is 0.080 cm^2. A galvanostat (Amel model 2056) is used to pass a DC current (i_{app}) through the brass screws and the resulting voltage drop (ΔV) across the material is measured at the Pt wires using a multimeter. A plot of ΔV versus i_{app} via eqn. 1 can then be used to determine the conductivity (σ),

$$\sigma = \frac{i_{app} \bullet l}{A_s \bullet \Delta V} \qquad [1]$$

where σ has units of Ω^{-1} cm^{-1}.

To evaluate the reproducibility of this measurement, a sample was packed into the device, its conductivity determined, and the sample was removed from the device and repacked to repeat the measurement. This procedure was repeated twice to obtain three measurements of the conductivity for each sample. We note that when the direction of i_{app} was reversed, there was no evidence of polarization.

Infrared spectra were acquired with a Nicolet 750 FT-IR spectrometer that was purged with boil-off from liquid N_2. All measurements used a liquid N_2-cooled HgCdTe detector. Samples were mixed with potassium bromide (99+% FT-IR grade, Aldrich) and pressed into pellet form using a hydraulic press. Pellets were then mounted in the spectrometer using standard pellet holder accessories.

X-ray photoelectron spectroscopy (XPS) data were obtained using a Physical Electronics Industries 5500 surface analysis system, equipped with a hemispherical analyzer, torridal monochromator, and multichannel detector. The sampling area was ~2 mm^2. A pass energy of 187.85 eV was used with a resolution of ~0.3 eV. Monochromatic Al Kα radiation (1486.6 eV) at 250-W was used for excitation. Photoelectrons were collected at 45° from the surface normal, with an acquisition time of less than 15 min. The C(1s) peak served as the internal reference for binding energies. The base pressure of the XPS chamber was less than 9×10^{-10} Torr during all analyses. Spectral deconvolution of the V($2p_{3/2}$) feature was restricted to a 2-component system using Gaussian peak profiles.

X-ray powder diffraction experiments were performed at the Molecular Structure Laboratory housed in the University's Chemistry Department using a Scintag XRD 2000 diffractometer with a Cu (lambda 1.5418 Å) radiation source.

RESULTS AND DISCUSSION

The conductivity of vanadium sol-gels is dependent upon several factors, including the oxidation state of the vanadium center,[24,26,28] the water content of the sol-gel,[16,28,29] and the vanadium-oxygen stoichiometry.[56] The fully oxidized vanadium oxide, V_2O_5, is an n-type semiconductor[35] with a bandgap of ~2 eV.[16,17] However, the monooxide, VO, has metallic-type conductivity.[57] The effects of all of these parameters were investigated in our attempts to enhance the conductivity of vanadium sol-gels.

Effect of Acid on the Conductivity of Vanadium Sol-Gels. Tri-n propoxide vanadium oxide undergoes acid-catalyzed hydrolysis in a manner directly analogous to alkoxy silanes.[58] In fact, vanadium is much more electropositive than silicon and can undergo hydrolysis without a catalyst. However, when used, the identity and concentration of acid has a notable impact on the conductivity of the resulting sol-gel. Figure 2 plots ΔV vs i_{app} for vanadium sol-gels catalyzed with various acids; the Figure also contains a plot for a sample prepared without acid to serve as a control. The slope of these plots is inversely proportional to the conductivity of the samples. When H_2SO_4 is used as the catalyst (Fig. 2A), the conductivity of the material decreases with respect to the control sample (Fig. 2B). However, when either HNO_3 (Fig. 2C,D,F) or HCl (Fig. 2E,G) are used, the conductivity of the resulting sol-gel increases with respect to the control (Fig. 2B). Specifically, when equal moles of tri-n propoxide vanadium oxide and HCl are used (Fig. 2G), the conductivity of the sol-gel increases ~25 times.

We attribute these observations to several factors, all of which are well documented in the literature. Previous work demonstrated that when strong acids were used to catalyze the hydrolysis of vanadium alkoxides, all of the alkoxy groups were removed.[22] However, in

the absence of strong acid catalysts, evidence supported the persistence of non-hydrolyzed vanadium alkoxy moieties even in the presence of excess water.[55] These findings suggest that strong acid catalysts are necessary to ensure complete hydrolysis. We theorize that non-hydrolyzed alkoxy groups may be present in the control sample, reducing the conductivity by preventing optimal crosslinking within the structure. Therefore, the use of strong acid catalysts, e.g., HCl, HNO_3, or H_2SO_4, would ensure the more exhaustive completion of the hydrolysis of the starting alkoxide, yielding sol-gels with higher conductivity. We believe that this theory explains the data obtained from the HNO_3-catalyzed samples. However, our results, which show that the identity of the acid influences the conductivity of sol-gels, suggest that other factors are also operating in the HCl and H_2SO_4 systems.

We speculate that when HCl is used as a catalyst, in addition to ensuring the effective hydrolysis of the vanadium alkoxide, chloride ion reduces vanadium centers. This reduction results in the increased conductivity of these samples with respect to the HNO_3-treated samples. As mentioned, sol-gels with vanadium centers in reduced oxidation states are more conductive than those in which all vanadium centers are fully oxidized. We theorize that in samples treated with HCl, a portion of V(V) is converted to V(IV) with the concurrent oxidation of the chloride ion. Our speculation is supported by reports in the literature that document this phenomena. Vanadium (V) compounds are moderately strong oxidizing agents[59] and chlorine gas is evolved when V_2O_5 is dissolved in HCl.[59] Further, when HCl was used to catalyze the hydrolysis of vanadia-silica zerogels, electron spin resonance verified the slow reduction of V(V) to V(IV).[60] Finally, we note that HCl is often used as a reductant in the preparation of vanadium-phosphorus catalysts from V_2O_5.[61,62]

A different process is likely at work in H_2SO_4-treated samples. Samples catalyzed with H_2SO_4 are less conductive (Fig. 2A) than the control (Fig. 2B). We speculate that while H_2SO_4 drives the conversion of starting alkoxide to completion, sulfur from the acid may contaminate the sol-gels. Reports where H_2SO_4 was used to initiate hydrolysis of titanium and zirconium alkoxides observed via X-ray fluorescence large concentrations of sulfur in the product.[63] In addition, vanadia-based materials hydrolyzed with H_2SO_4 showed significantly decreased catalytic performance when compared to samples hydrolyzed with HNO_3,[34] resulting in speculation that the decrease in catalytic performance arose from sulfur-inhibition of the active vanadium sites within the material. Because reduced vanadium centers are responsible for both the catalytic properties of vanadia-based catalysts and increased material conductivity, processes that decreases the catalytic activity of these materials would most likely reduce their conductivity as well.

Based on these results, an alkoxide:HCl molar ratio of 1:0.5 was used in all subsequent experiments. Although an alkoxide:HCl molar ratio of 1:1 and an alkoxide HNO_3 molar ratio of 1:5 yielded samples with a higher conductivity than a 1:0.5 HCl molar ratio, the latter was used because of its ease of handling. The former samples had a softer consistency even after ~2 months of drying in the laboratory ambient which complicated subsequent characterizations.

Effect of Heat in Various Gas Environments on the Conductivity of Vanadium Sol-Gels. We next investigated the effect of drying conditions on the conductivity of vanadium sol-gels. When dried in the laboratory ambient, vanadium oxide gels have a layered structure that contains both physisorbed and chemisorbed water within the interlayer spacing.[28] Physisorbed water can be removed by heating up to 180 °C.[28] Removal of

chemisorbed water occurs at 300 ^{0}C and yields a crystalline material[49] of increased conductivity because of more extensive V-O-V bonding between layers.[28] When heated in air, the conductivity of vanadium sol-gels decreases dramatically as oxidation of reduced vanadium centers occurs. Therefore, to either preserve or enhance the amount of reduced vanadium centers, heating must be done in a non-oxidizing environment. This section examines the conductivity of vanadium sol-gels heated in either H_2, a reducing gas, or He, a control gas.

Figure 3 plots ΔV vs i_{app} for HCl-catalyzed vanadium sol-gels after drying to either 200 °C or 350 °C in a H_2 or He environment. When heated at 200 °C for 2 hours in either He (Fig. 3B) or H_2 (Fig. 3C), sample conductivity increased by nearly two orders of magnitude when compared to the control sample (Fig. 3A). Furthermore, the conductivity of the samples heated in either H_2 or He are statistically indistinguishable. This finding argues that H_2 treatment under these conditions is not reducing vanadium centers, suggesting that a change in oxidation state is not responsible for the increase in conductivity.

Inspection of samples heated to 350 °C shows a further increase in conductivity. In contrast to 200 °C, the identity of the gas at 350 °C had a strong effect on the conductivity of the sol-gel. Samples heated in H_2 (Fig. 3E) were ~16 times more conductive than those heated in He (Fig. 3D) and 1000 times more conductive than the control (Fig. 3A). If the loss of chemisorbed water was alone responsible for conductivity of these samples, one would expect the conductivity of the samples to be similar. This finding, however, suggests that reduction of vanadium centers may be occurring during the H_2 treatment, which would account for the increase in conductivity over the He-treated samples.

To examine structural changes in vanadium sol-gels upon heating, characterizations using infrared (IR) spectroscopy were conducted. Figure 4 presents a series of spectra obtained in KBr for the different sol-gels. The upper trace (Fig. 4A) is the spectra obtained from the control sample, that is, one dried only in the laboratory ambient and not subjected to further drying. Only the V=O vibration, centered at 998 cm^{-1}, is visible and its position agrees well with reported literature values for hydrated vanadium sol-gels.[64] The spectra obtained for the sample heated to 200 °C (Fig 4B), is similar to that obtained for the control and also contains the V=O vibration near 1000 cm^{-1}.

There are, however, dramatic differences upon heating samples to 350 °C (Fig. 4C). First, the V=O vibration is blue shifted by ~28 cm^{-1} to 1027 cm^{-1}. This shift reflects the loss of water within the sample and is consistent with reported values for dehydrated samples.[64] Also, the width of the spectral feature for the vibration is diminished, indicating a more homogeneous chemical environment after removal of water.

In addition to changes in the V=O stretch, new spectral features appear which can be assigned to V-O-V stretches. These vibrations arise from increased interlayer bonding as intercalated water is removed. Assignment of these peaks to particular V-O-V vibrations is difficult because X-ray diffraction of samples heated in this manner reveal the presence of a mixture of oxides including V_2O_5, V_2O_4, and V_4O_9 (data not shown). These vibrational features are sharpened in samples heated to 530 °C (Fig. 4D) and provide further evidence of interlayer bonding.

In an attempt to further increase the conductivity of vanadium sol-gels, we also examined the effect of heating to higher temperatures. Above ~500 °C, dissociation of the oxide begins, altering the vanadium-oxygen stoichiometry. There are at least 13 oxides of

vanadium[65] ranging from the fully oxidized pentoxide, V_2O_5, to the monooxide, VO, and, in general, the higher the V/O ratio, the more conductive the oxide. Specifically, we attempted to create vanadium trioxide, V_2O_3, by the following reaction:

$$V_2O_5 + 2H_2 \xrightarrow{600^\circ C - 650^\circ C} V_2O_3 + 2H_2O$$

Although our sol-gel product appears by X-ray powder diffraction analysis to be a mixture of oxides after 2 h at 350 °C in H_2 (data not shown), it does contain a significant amount of V_2O_5. Therefore, we theorized that by heating in a second step such a sample to 650 °C in H_2 for 2 hrs, the trioxide could be obtained.

Figure 5 is the XRD spectra of a vanadium sol-gel sample after using the two-step heating process just described, i.e., a second heating at 650 °C for 2 h in H_2 after the initial 350 °C heating for 2 h in the same gas. After such treatment, the material is very crystalline and exhibits a sharp diffraction pattern. Analysis of the spectrum reveals that all features match those of the reference V_2O_3 spectrum (not shown).

To characterize changes in vanadium oxidation states upon heating, characterizations using XPS were conducted. Figure 6 is a series of XPS spectra showing the V(2p) binding region for sol-gels treated with the one-step and two-step heating processes. Spectra for commercially available V_2O_5, and V_2O_4 are also included, for reference. The V(2p) region is characterized by a doublet (i.e., $V(2p_{1/2})$ and $V(2p_{3/2})$) between 510 and 530 eV that arises from spin-orbit coupling.[66-68] The $V(2p_{3/2})$ centered near 517 eV band is often used to characterize vanadium oxidation state, where broadening on the lower energy side of this peak is indicative of reduced vanadium species. Inspection of the $V(2p_{3/2})$ for the V_2O_5 standard (Fig. 6A) reveals a symmetric $V(2p_{3/2})$ peak with no evidence of shoulders. In

contrast, inspection of the $V(2p_{3/2})$ peak for the other samples (Fig. 6B-D) reveals identifiable shouldering toward the lower energy side, indicating the presence of vanadium in lower oxidation states.

To gain a more quantitative understanding of vanadium oxidation state, spectral deconvolution of the $V(2p_{3/2})$ peak in Fig. 6B-D was performed using the restrictions described in the Experimental section. The higher binding energy component of the $V(2p_{3/2})$ feature can be assigned to V(V) while the lower energy component represents vanadium in a lower oxidation state. While an exact assignment of the reduced oxidation state is difficult,[69] a comparison of the area under the lower binding energy component with respect to the area of the entire $V(2p_{3/2})$ peak reveals that reduced oxidation state(s) of vanadium comprise 12%, 20%, and 87% of all vanadium in V_2O_4 and sol-gels heated with the one-step and two-step processes, respectively. This trend in composition is consistent with that seen in the conductivity data.

Evaluation of the conductivity of the sample treated by the two-step heating process as described above revealed a conductivity of $5.2 \pm 0.5\ \Omega^{-1}\ cm^{-1}$ ($n = 4$), a value that remained constant even after exposure to the laboratory ambient for 25 h. This value of conductivity represents a significant improvement over that of samples not subjected to such treatment.

CONCLUSIONS AND FUTURE WORK

We observed that the identity and concentration of acid used to initiate hydrolysis of tri-n propoxide vanadium oxide had a significant impact on conductivity. While all strong acid ensure more complete hydrolysis of the alkoxy groups within the precursor with respect to the no-acid control, addition factors are responsible for observed differences among the acids. We theorize that redox chemistry is at work in the HCl-catalyzed samples and increases the reduced vanadium content of the sol-gels, whereas sulfur contaminants from H_2SO_4-catalyzed samples inhibit reduced vanadium centers and decrease the conductivity of the sol-gels. In contrast, HNO_3-catalyzed samples do not exhibit redox chemistry or contaminants and, therefore, have a conductivity intermediate to that of the other acids but one that is higher than that of the control. The conductivity of vanadium sol-gels is also dependent upon the heating conditions used to remove physisorbed and chemisorbed water. Specifically, samples treated in H_2 to 350 °C for 2 h displayed increased V-O-V bonding and a conductivity ~1000 times greater than that of the control. Further increases in conductivity were obtained by heating samples previous treated in H_2 at 350 °C for 2 h to 650 °C for 2 h in the same gas. This treatment created V_2O_3 sol-gels of high crystallinity that contained a significant portion of reduced vanadium, as determined by XPS. Further work in this area will examine more fully the role of strong acids in the hydrolysis process and also pursue alternative heating strategies to further increase the conductivity of these materials.

ACKNOWLEDGEMENTS

J.C.O. gratefully acknowledges the support of a Phillips Petroleum Corporation graduate research fellowship. We also express our appreciation to James Anderegg for the XPS characterizations as well as Larry Jones and Trevor Rhediemann of the Ames Laboratory Materials Preparation Center for the use of the tube furnace. We further acknowledge Ilia Guzei of the Molecular Structure Laboratory, Chemistry Department, Iowa State University for his assistance in obtaining the diffraction spectra. This work was supported in part by the Office of Basic Energy Science, Chemical Sciences Division of the U.S. Department of Energy. The Ames Laboratory is operated for the U.S. Department of Energy by Iowa State University under Contract W-7405-eng-82.

REFERENCES

(1) Ziemath, E.; Aegerter, M. A.; Moreira, J.; Figueiredo, M.; Zarzycki, J. In *Better Ceramics through Chemistry III*; Brinker, C. J., Clark, D. E., Ulrich, D. R., Eds.; Materials Research Society: Pittsburgh, 1988; p 311.

(2) Ayral, A.; Phalippou, J.; Droguet, J. C. In *Better Ceramics through Chemistry III*; Brinker, C. J., Clark, D. E., Ulrich, D. R., Eds.; Materials Research Society: Pittsburgh, 1988; p 239.

(3) Scriven, L. E. In *Better Ceramics through Chemistry III*; Brinker, C. J., Clark, D. E., Ulrich, D. R., Eds.; Materials Research Society: Pittsburgh, 1988; p 717.

(4) Pommier, B.; Teichner, S. J. *Proc. Int. Congr. Catal.* **1988**, *2*, 610.

(5) Ochoa, R.; Miranda, R. In *Better Ceramics through Chemistry VI*; Cheetham, A. K., Brinker, C. J., Mecartney, M. L., Sanchez, C., Eds.; Materials Research Society: Pittsburgh, 1994; p 553.

(6) L'Esperance, D.; Browne, C. A.; Chronister, E. L. In *Better Ceramics through Chemistry VI*; Cheetham, A. K., Brinker, C. J., Mecartney, M. L., Sanchez, C., Eds.; Materials Research Society: Pittsburgh, 1994; p 579.

(7) Nazeri-Eshghi, A.; Mackenzie, J. D.; Yang, J. M. In *Better Ceramics through Chemistry III*; Brinker, C. J., Clark, D. E., Ulrich, D. R., Eds.; Materials Research Society: Pittsburgh, 1988; p 561.

(8) Gonzalez-Oliver, C. J. R.; Kato, I. *J. Non-Cryst. Solids* **1986**, *82*, 400.

(9) Terrier, C.; Chatelon, J. P.; Roger, J. A. *Thin Solid Films* **1997**, *295*, 95.

(10) Ozer, N.; Barreto, T.; Buyuklimanli, T.; Lampert, C. M. *Sol. Energy Mater. Sol. Cells* **1995**, *36*, 433.

(11) Spinolo, G.; Ardizzone, S.; Trasatti, S. *J. Electroanal. Chem* **1997**, *423*, 49.

(12) Swider, K. E.; Merzbacher, C. I.; Hagains, P. L.; Rolison, D. R. *Chem. Mater.* **1997**, *9*, 1248.

(13) Tavcar, G.; Kalcher, K.; Ogorevc, B. *Analyst* **1997**, *122*, 371.

(14) Bay, N. T. B.; Tien, P. M.; Badilescu, S.; Djaoued, Y.; Bader, G.; Girouard, F. E.; Truong, V.-V.; Nguyen, L. Q. *J. Appl. Phys.* **1996**, *80 (12)*, 7041.

(15) Bielanski, A.; Ptwowarczyk, J.; Pozniczek, J. *J. Catal.* **1988**, *113*, 334.

(16) Bullot, J.; Cordier, P.; Gallais, O.; Gauthier, M.; Livage, J. *J. Non-Cryst. Solids* **1984**, *68*, 123.

(17) Chain, E. E. *Appl. Opt.* **1991**, *30, 19*, 2782.

(18) Damme, H. V.; Letellier, M.; Tinet, D.; Kihal, B.; Erre, R. *Mater. Res. Bull.* **1984**, *19*, 1635.

(19) Gharbi, N.; Sanchez, C.; Livage, J.; Lemerle, J.; Nejem, L.; Lefebvre, J. *Inorg. Chem.* **1982**, *21*, 2758.

(20) Gillis, E.; Boesman, E. *Phys. Status Solidi* **1966**, *14*.

(21) Glezer, V.; Lev, O. *J. Am. Chem. Soc.* **1993**, *115*, 2533.

(22) Hirashima, H.; Tsukimi, K.; Muratake, R. In *Ultrastructure Processing of Advanced Materials*; Uhlmann, D. R., Ulrich, D. R., Eds.; John Wiley & Sons, Inc.: New York, 1992; p 285.

(23) Honma, K.; Yoshinaka, M.; Hirota, K.; Yamaguchi, O.; Asm, J.; Makiyama, Y. *Int. J. Soc. Mater. Eng. Resour.* **1997**, *5 (1)*, 9.

(24) Ioffe, V. A.; Patrina, I. B. *Sov. Phys. S.S.* **1965**, *6*, 2425.

(25) Kamiyama, T.; Itoh, T.; Suzuki, K. *J. Non-Cryst. Solids* **1988**, *100*, 466.

(26) Kennedy, T. M.; Hakim, R.; Mackenzie, J. D. *Mater. Res. Bull.* **1967**, *2*, 193.

(27) Lemerle, J.; Nejem, L.; Lefebvre, J. *J. Inorg. Nucl. Chem.* **1980**, *42*, 17.

(28) Livage, J. In *Better Ceramics through Chemistry*; Brinker, C. J., Clark, D. E., Ulrich, D. R., Eds.; Elsevier Science Publishing Company Inc.: New York, 1984; p 125.

(29) Livage, J.; Barboux, P.; Badot, J. C.; Baffier, N. In *Better Ceramics through Chemistry III*; Brinker, C. J., Clark, D. E., Ulrich, D. R., Eds.; Materials Research Society: Pittsburgh, 1988; p 167.

(30) Livage, J. *Chem. Mater.* **1991**, *3*, 578.

(31) Livage, J.; Baffier, N.; Pereira-Ramos, J. P.; Davidson, P. In *Solid State Ionics IV*; Nazri, G.-A., Tarascon, J.-M., Schreiber, M., Eds.; Materials Research Society: Pittsburgh, 1995; p 179.

(32) West, K.; Zachau-Christiansen, B.; Ostergard, M. J. L.; Jacobsen, T. *J. Power Sources* **1987**, *20*, 165.

(33) Gasser, D.; Baiker, A. *J. Catal.* **1988**, *113*, 325.

(34) Schneider, M.; Maciejewski, M.; Tchudin, S.; Wokaun, A.; Baiker, A. *J. Catal.* **1994**, *149*, 326.

(35) Gharbi, R. C.; Ballutaud, D.; Michaud, M.; Audiere, J. P.; Schiffmacher, G. *J. Non-Cryst. Solids* **1981**, *46*, 247.

(36) Aldebert, P.; Baffier, N.; Gharbi, N.; Livage, J. *Mater. Res. Bull.* **1981**, *16*, 949.

(37) Aldebert, P.; Baffier, N.; Legendre, J.-J.; Livage, J. *Rev. Chim. Miner.* **1982**, *19*, 485.

(38) Aldebert, P.; Paul-Boncour, V. *Mater. Res. Bull.* **1983**, *18*, 1263.

(39) Arakei, B.; Mailhe, C.; Baffier, N.; Livage, J.; Vedel, J. *Solid State Ionics* **1983**, *9-10*, 439.

(40) Bouhaouss, A.; Aldebert, P. *Mater. Res. Bull.* **1983**, *18*, 1247.

(41) Bouhaouss, A.; Aldebert, P.; Baffier, N.; Livage, J. *Rev. Chim. Miner.* **1985**, *22*, 417.

(42) Lemordant, D.; Bouhaouss, A.; Aldebert, P.; Baffier, N. *Mater. Res. Bull.* **1986**, *21*, 273.

(43) Masbah, H.; Tinet, D.; Crespin, M.; Erre, R.; Setton, R.; Damme, H. V. *J. Chem. Soc. Chem. Commun.* **1985**, 935.

(44) Ruiz-Hitzky, E.; Casal, B. *J. Chem. Soc. Faraday Trans.* **1986**, *82*, 1597.

(45) Muller, Z. *Kolloides* **1911**, *8*, 302.

(46) Michaud, M.; Leroy, M. C.; Livage, J. *Mater. Res. Bull.* **1976**, *11*, 1425.

(47) Gharbi, R. C.; Ballutaud, D.; Michaud, M.; Livage, J.; Audiere, J. P.; Schiffmacher, G. *J. Non-Cryst. Solids* **1981**, *46*, 247.

(48) Lemerle, J.; Nejem, L.; Lefebvre, J. *J. Chem. Res.* **1978**, 5301.

(49) Aldebert, P.; Baffier, N.; Gharbi, N.; Livage, J. *Mater. Res. Bull.* **1981**, *16*, 669.

(50) Babonneau, F.; Barbous, P.; Josien, F. A.; Livage, J. *J. Chim. Phys.* **1985**, *82*, 761.

(51) Kittaka, S.; Sumida, M.; Kuroda, Y. In *Better Ceramics through Chemistry*; Cheetham, A. K., Brinker, C. J., Mecartney, M. L., Sanchez, C., Eds.; Materials Research Society: Pittsburgh, 1994; Vol. VI; p 697.

(52) Gasser, D; Baiker, A. *J. Catal.* **1988**, *113*, 325.

(53) Miyahara, H.; Kittaka, S. *Bull. Hiruzen Res.* **1992**, *18*, 1.

(54) Ozer, N. *Thin Solid Films* **1997**, *305*, 80.

(55) Sanchez, C.; Nabavi, M.; Taulelle, F. In *Better Ceramics through Chemistry III*; Brinker, C. J., Clark, D. E., Ulrich, D. R., Eds.; Materials Research Society: Pittsburgh, 1988; p 93.

(56) Nakamura, T.; Huruyama, S. *Bull. Chem. Soc. Jpn.* **1979**, *52*, 3253.

(57) Gupta, C. K.; Krishnamurthy, N. *Extractive Metallurgy of Vanadium*; Elsevier: Amsterdam, 1992.

(58) Brinker, C. J.; Scherer, G. W. *Sol-Gel Science: The Physics and Chemistry of Sol-Gel Processing*; Academic Press, Inc.: Boston, 1990.

(59) Cotton, F. A.; Wilkinson, F. *Advanced Inorganic Chemistry*; 5 ed.; John Wiley & Sons: New York, 1988.

(60) Curran, M. D.; Gedris, T. E.; Steigman, A. E. *Chem. Mater.* **1999**, *11*, 1120.

(61) Busca, G.; Cavank, F.; Centi, G.; Trifiro, F. *J. Catal.* **1986**, *99*, 400.

(62) Centi, G.; Trifiro, F.; Ebner, J. R.; Franchetti, V. M. *Chem. Rev.* **1988**, *88*, 55.

(63) Leaustic, A.; Riman, R. E. *J. Non-Cryst. Solids* **1991**, *135*, 259.

(64) Wachs, I. E. *J. Catal.* **1990**, *124*, 570.

(65) *Binary Alloy Phase Diagrams*; Massalski, T. B.; Murray, J. L.; Bennett, L. H.; Baker, H., Eds.; American Society for Metals: Metals Park, OH, 1986.

(66) Chiarello, G.; Robba, D.; Michele, G. D.; Parmigiani, F. *Appl. Surf. Sci.* **1993**, *64*, 91.

(67) Lu, S.; Hou, L.; Gan, F. *J. Mater. Sci.* **1993**, *2*, 2169.

(68) Sawatzky, G. A.; Post, D. *Phys. Rev. B.* **1979**, *20*, 1546.

(69) Eberhardt, M. A.; Proctor, A.; Houalla, M.; Hercules, D. M. *J. Catal.* **1996**, *160*, 27.

FIGURE CAPTIONS

Figure 1. Conductivity Device. The device consists of a plexiglass tube threaded on both ends to accommodate brass screws. When inserted, the screws (surface area (A_s) 0.080 cm^2) are separated by a gap of 0.40 cm. Powder samples are inserted into this gap and contacted on opposite ends by the screws. Conductivity data is obtained via the four probe method by passing a DC current (i_{app}) through the screws and measuring the voltage drop (ΔV) within the material at two platinum wires inserted into the material and held at a fixed distance of 2.0 mm from each other (l).

Figure 2. Effect of Acid on the Conductivity of Vanadium Sol-Gels. Samples were prepared as described in the Experimental section and subjected to 14 days drying in the laboratory ambient.. The identity and mole value of the acid used is listed below. Conductivity (σ) values represent the average of triplicate measurements; the error

bars indicate the standard deviation. (A,■): H_2SO_4, (0.5 mole), $\sigma = 5.3 \times 10^{-6}\ \Omega^{-1}\ cm^{-1}$; (B,•): control (no acid), $\sigma = 7.8 \times 10^{-5}\ \Omega^{-1}\ cm^{-1}$; (C,▲): HNO_3 (0.5 mole), $\sigma = 1.8 \times 10^{-4}\ \Omega^{-1}\ cm^{-1}$; (D,□): HNO_3 (1 mole), $\sigma = 2.4 \times 10^{-4}\ \Omega^{-1}\ cm^{-1}$; (E,♦): HCl (0.5 mole), $\sigma = 2.7 \times 10^{-4}\ \Omega^{-1}\ cm^{-1}$; (F,○): HNO_3 (5 mole), $\sigma = 4.5 \times 10^{-4}\ \Omega^{-1}\ cm^{-1}$; (G,▼): HCl (1 mole), $\sigma = 2.0 \times 10^{-3}\ \Omega^{-1}\ cm^{-1}$.

Figure 3. Effect of Heating on the Conductivity of Vanadium Sol-Gels. Samples were prepared as described in the Experimental section and subjected to 7 days drying in the laboratory ambient prior to heating. Samples were then heated for 2 hours at the temperature and in the gas environment indicated. Conductivity (σ) values represent the average of triplicate measurements; error bars indicate the standard deviation. (A,•): control (no heating), $\sigma = 5.3 \times 10^{-5}\ \Omega^{-1}\ cm^{-1}$; (B,■): 200 °C in He, $\sigma = 1.5 \times 10^{-3}\ \Omega^{-1}\ cm^{-1}$; (C,▲): 200 °C in H_2, $\sigma = 1.6 \times 10^{-3}\ \Omega^{-1}\ cm^{-1}$; (D,▼): 350 °C in He, $\sigma = 5.3 \times 10^{-3}\ \Omega^{-1}\ cm^{-1}$; (E,♦): 350 °C in H_2, $\sigma = 8.8 \times 10^{-2}\ \Omega^{-1}\ cm^{-1}$.

Figure 4. IR spectra (in KBr) of Vanadium Sol-Gels Heated for 2 h in H_2. (A): control (no heating); (B): 200 °C; (C): 350 °C; (D): 530 °C.

Figure 5. The powder X-ray diffraction spectra of a vanadium sol-gel subjected to the 2-step heating process in H_2. All features are consistent with V_2O_3.

Figure 6. The V(2p) binding region of vanadium sol-gels and commercially available oxides. (A): V_2O_5 (Aldrich); (B): V_2O_4 (Aldrich); (C): sol-gel heated to 350 °C for 2 h in H_2 (1-step heating process); (D): sol-gel heated to 350 °C for 2 hours in H_2 followed by an additional 2 h in H_2 at 650 °C (2-step heating process). Unrestricted two-component deconvolution using Gaussian profiles was used.

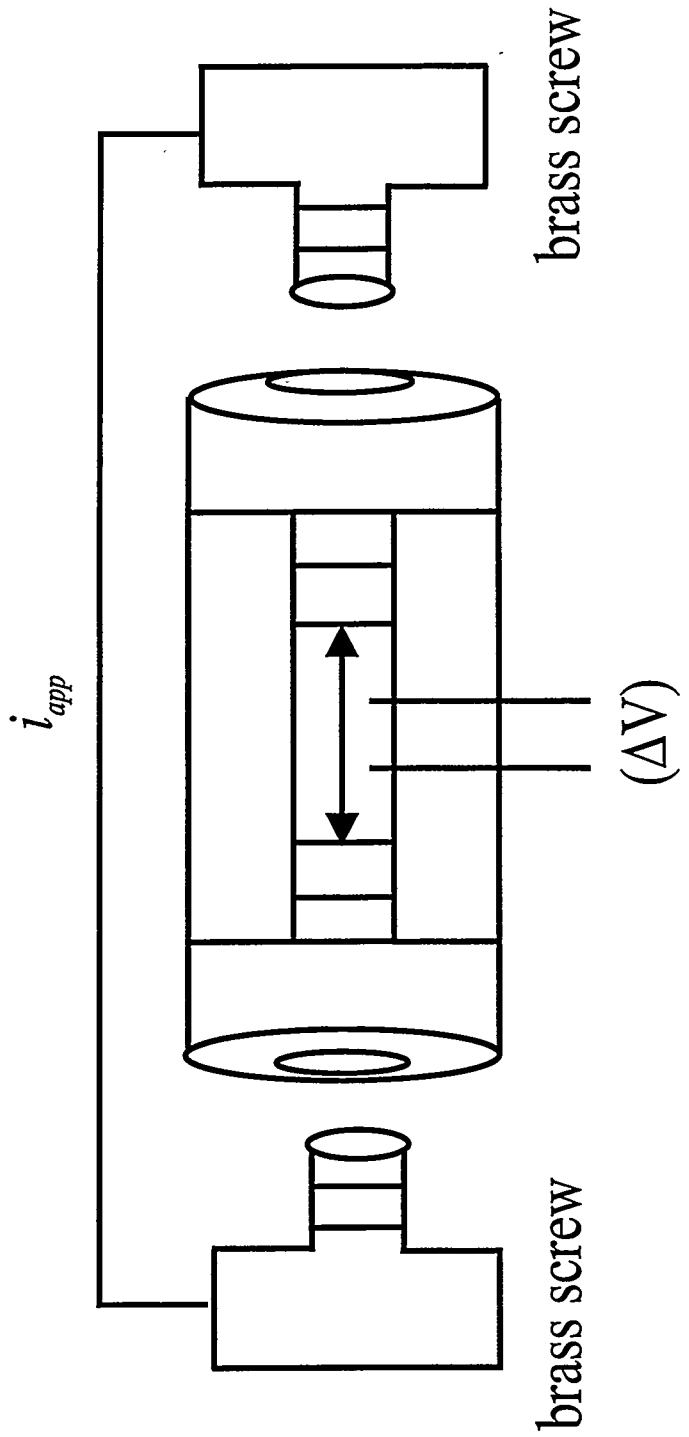

Figure 1.

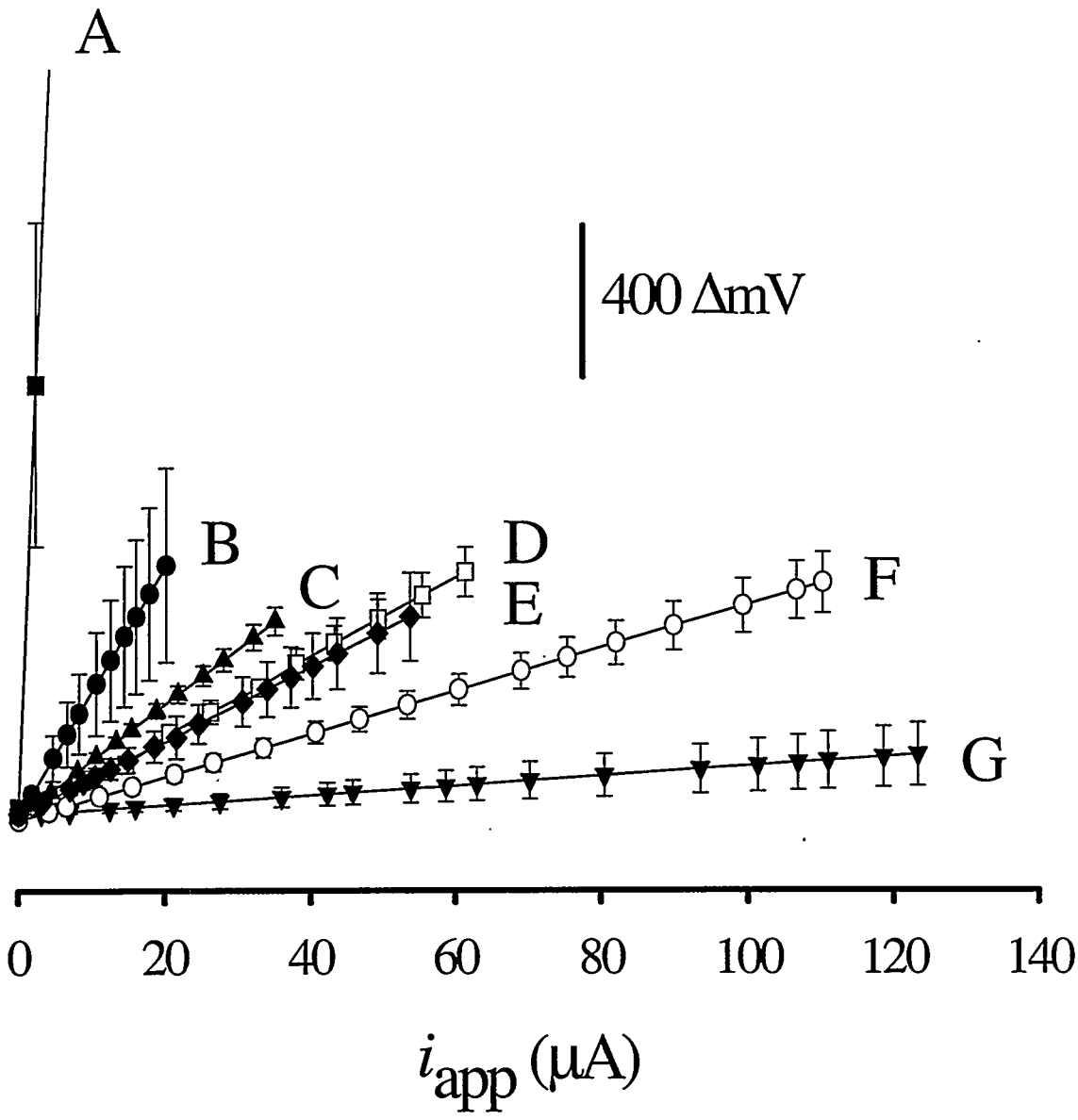

Figure 2.

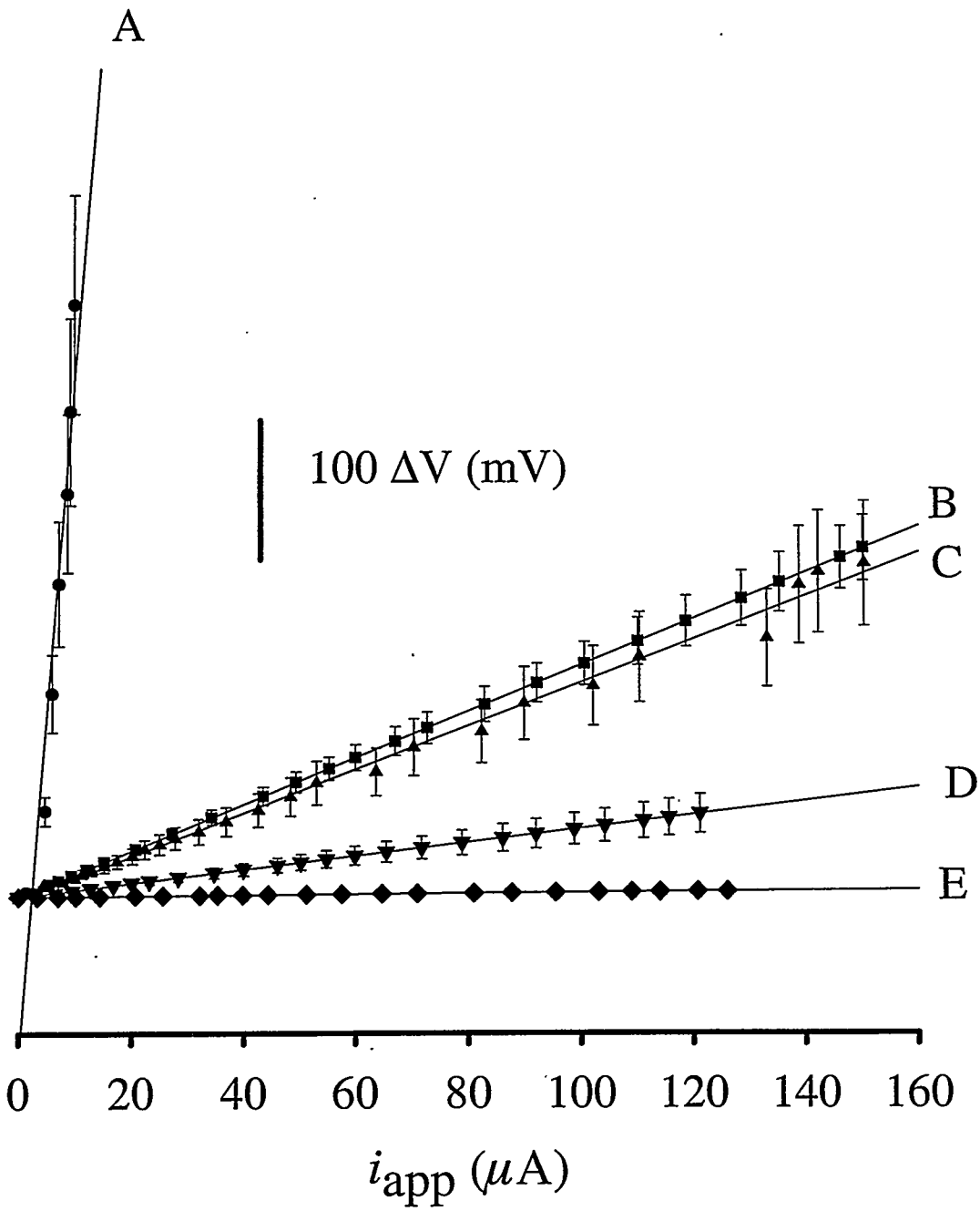

Figure 3.

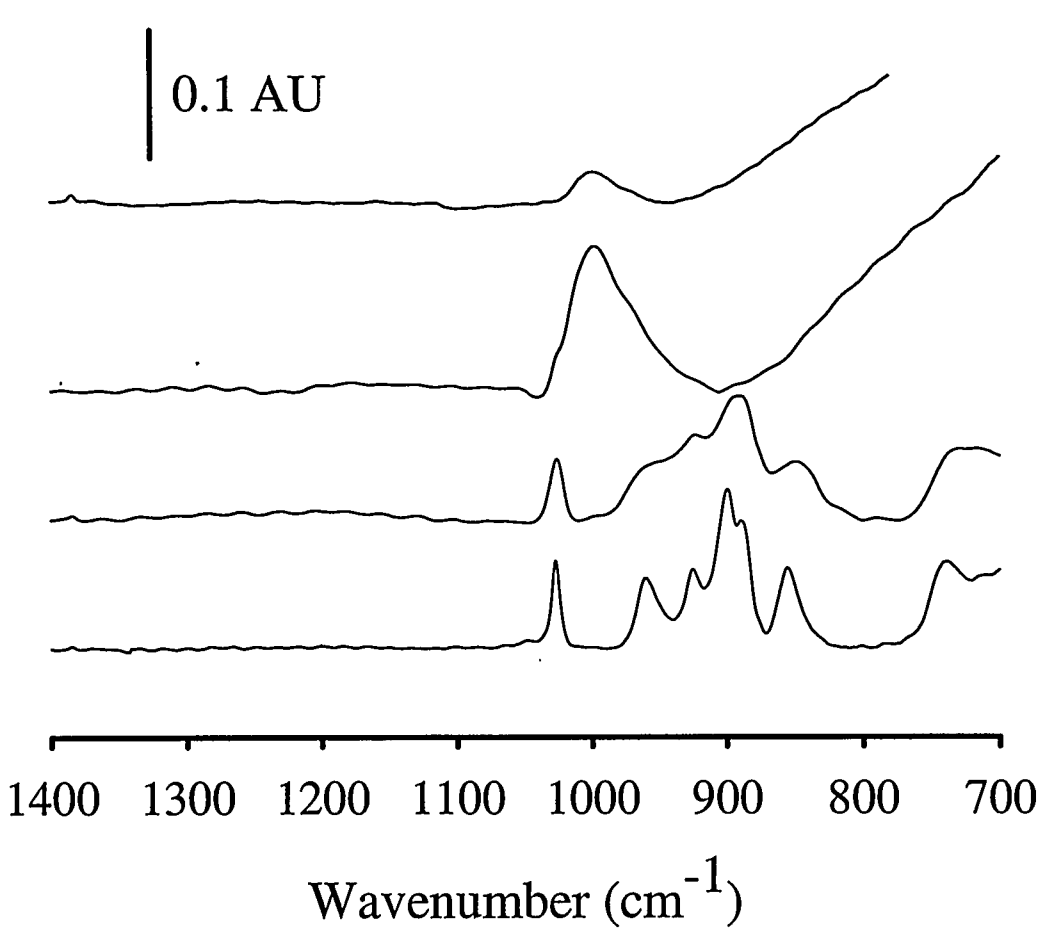
0.1 AU
A
B
C
D
1400
1300
1200
1100
1000
900
800
700
Wavenumber (cm-1)

Figure 4.

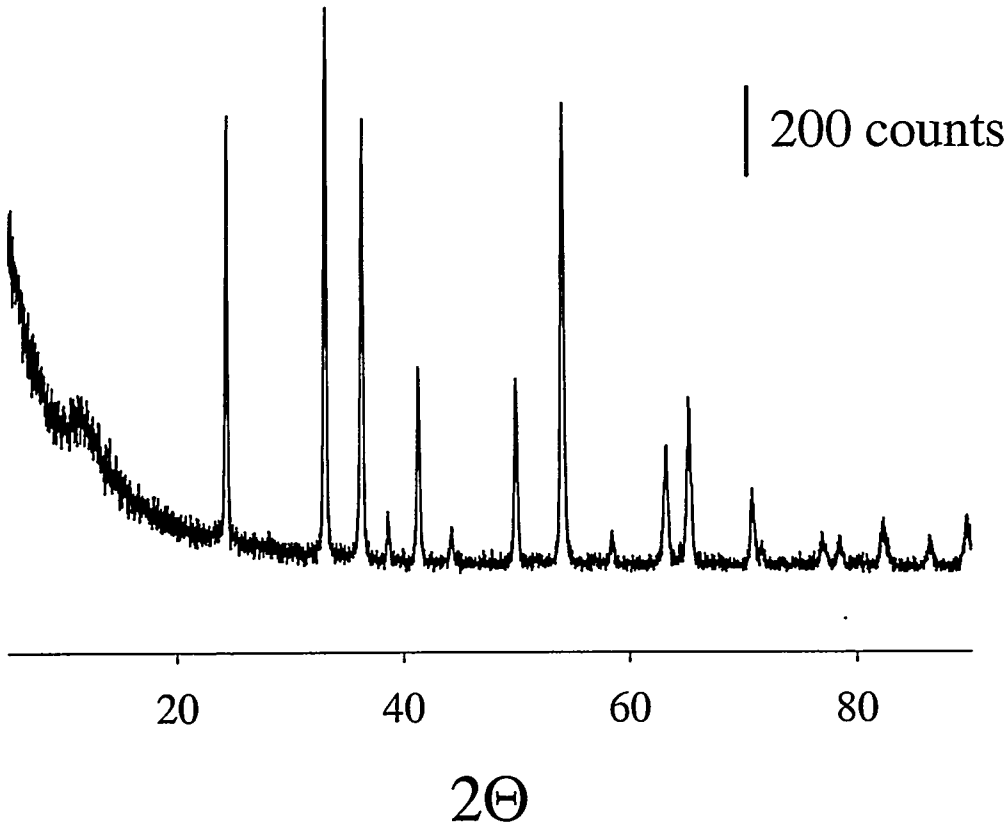

Figure 5.

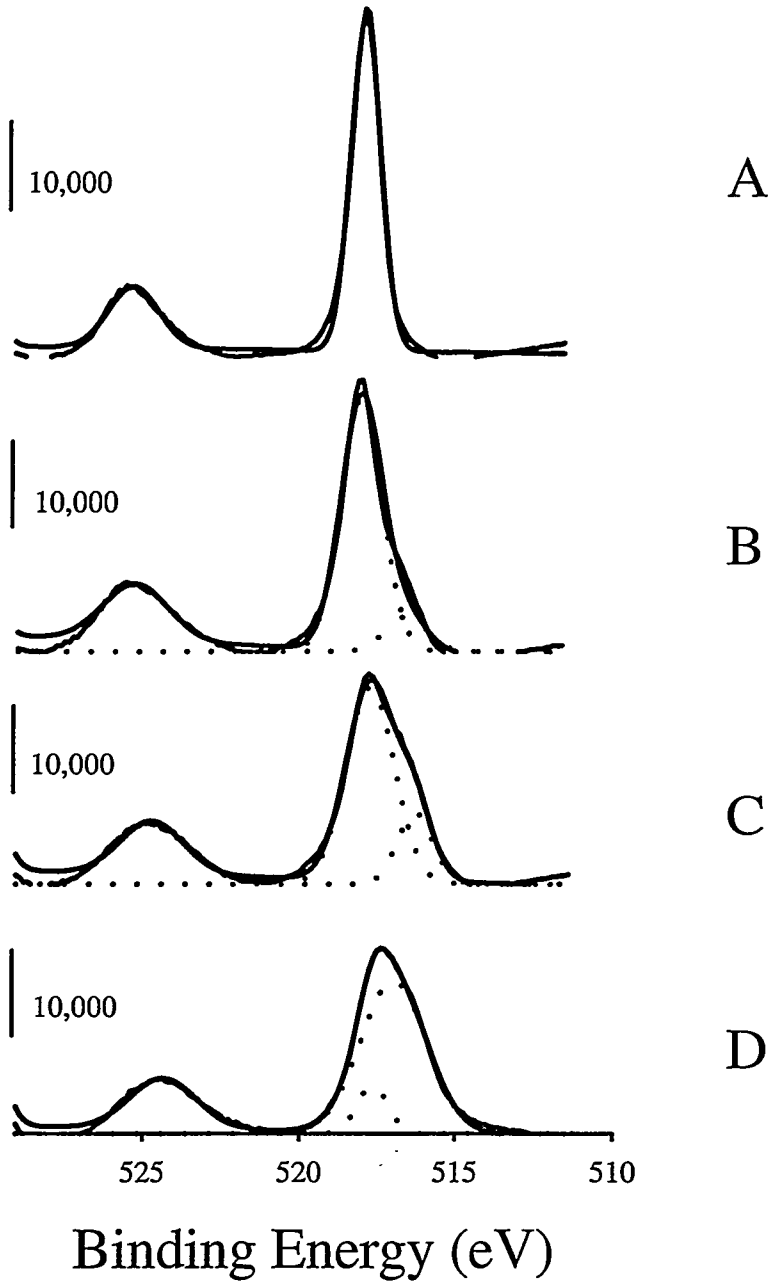
10,000
A
10,000
B
10,000
C
10,000
D
525
520
515
510
Binding Energy (eV)

Figure 6.

CHAPTER 3. IMMUNOSENSING PLATFORMS USING SPONTANEOUSLY ADSORBED ANTIBODY FRAGMENTS ON GOLD

A paper published in *Analytical Chemistry*[1]

Janese C. O'Brien,[2] Vivian W. Jones,[2] Marc D. Porter,[2,3] Curtis L. Mosher,[4] and Eric Henderson[4]

Abstract

This paper describes the construction and characterization of miniaturized antigenic immunosurfaces composed of spontaneously adsorbed Fab'-SH fragments on gold. Rabbit Fab'-SH fragments contain a free sulfhydryl group that forms a thiolate bond with a gold substrate as detailed by X-ray photoelectron spectroscopy. This approach creates surfaces of higher epitope density, a factor critical to the early detection of disease, than surfaces composed of adsorbed whole molecule IgG on gold. The viability and specificity of antigenic Fab'-SH immunosurfaces is demonstrated using atomic force microscopy and confocal fluorescence microscopy, and possible explanations for the larger epitope density are discussed.

---

[1] Reprinted with permission from *Anal. Chem.* **2000**, 72, 703-710.

[2] Microanalytical Instrumentation Center, Ames Laboratory-DOE, and Department of Chemistry, Iowa State University, Ames, Iowa 50011

[3] Corresponding author

[4] Microanalytical Instrumentation Center, Department of Zoology and Genetics, Iowa State University, Ames, Iowa 50011

Introduction

Early diagnosis of disease is critical in determining patient outcome. Early detection using immunological methods, however, is often complicated because low-affinity antibodies dominate the first stages of the immune response. The detection of low-affinity antibodies, moreover, is intimately linked to epitope density.[1-3] Indeed, a report using ELISA found that even modest increases in epitope density result in a marked improvement in the ability to detect lower affinity antibodies.[1] Maximizing epitope density is then critical to early disease detection.

We recently described an immunoassay concept that exploits the topographic imaging capabilities of the atomic force microscope (AFM).[4] The assay is based on the height change that results from the specific binding of a ligand in solution to its surface-immobilized receptor. We demonstrated the capability of this technique using compositionally patterned surfaces created by combining photolithography and self-assembled monolayer technologies. To this end, micrometer-sized domains of a monolayer of a gold-supported coupling agent were surrounded by micrometer-sized grids of a strongly hydrophobic monolayer. Thus, the coupling agent served as a means to tether IgG antigens in a spatially defined array, and the hydrophobic monolayer functioned as an internal reference plane for the height-based determination of specific binding. However, the large number of lysine residues, the target of the coupling agent, that are distributed throughout the IgG structure[5] resulted in a variety of orientational dispositions for immobilized IgG, a factor that influences the effective activity of immobilized antibodies.[5]

This paper investigates the use of spontaneously adsorbed Fab'-SH fragments for the

construction of an antigenic immunosurface. The immunosurface is formed as a patterned array by using rabbit IgG Fab' fragments, Fab'-SH, as a model test system. These fragments contain a free sulfhydryl group and were prepared by the controlled chemical reduction of rabbit $F(ab')_2$. We postulated that if the free sulfhydryl group influences the immobilization process by its chemisorption to gold, the attachment may regulate the orientation of adsorbed Fab'-SH as well as minimize the decreases in activity due to denaturation. If so, the immobilization of fragmented antigens rather than whole molecule analogues could potentially yield an immunosurface with a higher epitope density. Figure 1 idealizes this concept.

Previous reports have investigated the use of Fab'-SH fragments and various linking chemistries that target the free sulfhydryl group to create immunosurfaces where the fragments act as the antibody rather than the antigen.[6-10] These efforts, however, have produced mixed results in their ability to bind more antigen when compared to surfaces created from whole molecule IgG or from Fab'-SH immobilized through its amine functionalities. To our knowledge, there have been no previous reports on the use of spontaneously adsorbed Fab'-SH fragments for construction of antigenic surfaces. This strategy, which does not rely on any chemical linkers to attach Fab'-SH to our chosen substrate, may also prove useful in elucidating the role of the linkers in systems where the fragments act as the capture antibody. Of note, there has been a brief report on an AFM characterization of Fab'-SH coated on gold, but use in an assay was not discussed.[11]

We report herein the formation of a patterned array of immunospecific Fab'-SH surfaces. We show by applying thin-layer cell spectroscopy that immunosurfaces constructed

from the spontaneous adsorption of Fab'-SH on gold contain a higher epitope density when compared to those prepared by the adsorption of whole molecule analogues. Furthermore, the adsorbed fragments form viable immunosurfaces as is demonstrated using both AFM and fluorescence microscopy as readout methods. The potential merits of this strategy are briefly described.

Experimental Section

Gold Substrate Fabrication. Substrates were prepared using silicon wafers ((100) single crystals, Montco Silicon) or glass slides (Fisher). The silicon substrates were cleaned in an ultrasonic bath for 30 min in water and for 30 min in methanol. The glass substrates were cleaned in a dilute Micro (Cole-Parmer) solution and rinsed with deionized water and methanol. All substrates were then dried in a stream of high-purity argon (Air Products) and placed in a vacuum evaporator (Edwards High Vacuum Products). Next, the substrates were coated with 15 nm of chromium at 0.1 nm/s followed by 300 nm of gold (99.9%) at 0.3-0.4 nm/s. During coating, the pressure in the deposition chamber was ~8 x 10^{-6} Torr. The substrates were either used immediately upon removal from the evaporator or stored under dry nitrogen.

Monolayer Formation and Photopatterning (Steps 1 and 2). The preparation of the compositionally patterned monolayers paralleled the process previously described.[4] Step 1 involved the formation of a fluorinated monolayer by immersing the gold-coated substrates in a 10 mM solution of recrystallized ($SH(CH_2)_2(CF_2)_7CF_3$) for ~24 h.[12-14] These samples were then rinsed extensively with ethanol (Quantum, punctilious grade) and dried under a

stream of argon.

Step 2 entailed the photopatterning process and followed the guidelines described in the literature.[15] The patterns were prepared by sandwiching carefully a copper transmission electron microscopy (TEM) grid (2000 mesh, (hole size: 7.5 μm; bar size: 5.0 μm)) (Electron Microscopy Sciences) between the monolayer-coated sample and a quartz plate. A 200-W, medium-pressure mercury lamp (Oriel) was used as the light source. The beam was collimated, reflected off an air-cooled, dichroic mirror (220-260 nm), focused by a fused-silica lens, and passed through the TEM grid before impinging on the sample for ~20 min. During this process, the irradiated gold-bound thiolates are converted to various forms of oxygenated sulfur (e.g., RSO_3^-)[15-17] which are readily rinsed off the surface with most organic solvents.[17] Immediately following irradiation, the surfaces were rinsed extensively with deionized water and ethanol and dried under a stream of argon.

Preparation and Immobilization of Fab'-SH Fragments at Gold (Step 3). Fab'-SH fragments were obtained from the controlled chemical reduction of rabbit $F(ab')_2$, a truncated form of whole molecule IgG,[18] by using 2-mercaptoethylamine (2-MEA). This step cleaves the single disulfide bond which holds the two heavy chains of rabbit $F(ab')_2$ together to form two Fab'-SH fragments. We note that rabbit Fab'-SH fragments contain four disulfide bonds, some of which lie close to the antigen binding site. However, Fab'-SH fragments in which these disulfide bonds are reduced generally retain their structure and specific binding activity.[19] In addition, adjustment of the reaction conditions (e.g., concentration of 2-MEA and the duration and temperature of incubation) greatly minimizes the reduction of disulfide bonds near the antigen binding region.[20] We found that a 90-min

incubation at 37°C using 2-MEA at 50 mM was optimal for reducing rabbit $F(ab')_2$ at a concentration of 5 mg/mL to rabbit Fab'-SH with minimal cleavage of the disulfide bonds in the antigen binding region. Indeed, analysis of rabbit $F(ab')_2$ and its reduction product by matrix-assisted laser desorption/ionization mass spectrometry revealed the expected molecular weights of 89 189 ± 89 and 45 638 ± 46, respectively.

The progress of the reduction was followed by analyzing a small aliquot of the reaction mixture, which was first blocked with 5 μL of 700 mM iodoacetamide in 1.5 M Tris-HCl buffer (pH 8.5) to convert the free sulfhydryl to an amine-terminated thioether appendage and thus prevent the oxidation back to the disulfide, by nondenaturing sodium dodecyl sulfate polyacrylamide gel electrophoresis (SDS-PAGE). Upon completion of the reduction, the reaction mixture was transferred to a centrifuge tube containing a cellulose acetate filter with a nominal molecular weight limit of 5000 (Sigma) and spun at 6000 rpm to remove excess 2-MEA which stopped the reduction. Aliquots of phosphate buffer (PB; pH 6) were added to the sample during centrifugation to avoid precipitation of Fab'-SH and to minimize its adsorption on the filter. Centrifugation continued until the desired volume (~50 μL) was achieved. The patterning process was completed by injecting the solution of the Fab'-SH fragments into the AFM liquid cell, whereby Fab'-SH chemisorbs onto the exposed, square-shaped regions of the gold substrate which was mounted to the cell.

Instrumentation. (*i*). Atomic Force Microscopy (AFM). AFM experiments were performed on a Nanoscope IIIa AFM (Digital Instruments) equipped with a 150 μm scanner. Oxide-sharpened Si_3N_4 cantilevers were used for both contact and tapping mode imaging (Nanoprobes, Digital Instruments). The normal bending force constant of the cantilevers was

0.06 N/m. When tapping mode imaging was employed, the set point amplitude of the cantilever was maximized relative to its free space amplitude to minimize the imaging force applied to the surface. In situ imaging was conducted either in 50 mM phosphate buffered saline (PBS; pH 6) or in "binding buffer" (100 mM Tris, 100 mM $MgCl_2$, 50 mM NaCl, pH 7.6, and 1% (v/v) Tween 80). Tween 80 was used to minimize complications from nonspecific adsorption.[4] All images are presented without any subsequent data processing.

***(ii).* Confocal Fluorescence Microscopy.** Fluorescence images were acquired using an Odyssey confocal scanning laser microscope (Noran Instruments) in combination with an Axiovert 135 inverted microscope (Zeiss). For all fluorescence experiments, 16 confocal fluorescence images were collected and averaged using 488-nm excitation, a 515-nm low-pass barrier filter (rejection at 488 nm = 4×10^{-4}), and a 25-μm slit width.

***(iii).* X-Ray Photoelectron Spectroscopy (XPS).** A Physical Electronics Industries 5500 surface system was used for XPS characterizations. This system is equipped with a hemispherical analyzer, toroidal monochromator, and multichannel detector. A pass energy of 29.35 eV was used with a resolution of ~0.3 eV. Monochromatic Al Kα radiation (1486.6 eV) at 300 W was used for excitation. Photoelectrons were collected at 45° from the surface normal, with a 36-min acquisition time for the whole molecule IgG and Fab'-SH modified surfaces, 12 min for the alkanethiol- and alkanedithiol-modified surfaces, and 53 min for the thioether-modified version of our Fab'-SH surface. The Au($4f_{7/2}$) emission band served as an internal reference for binding energies. The base pressure of the XPS chamber was less than 9×10^{-10} Torr during all analyses, and the sampling area was ~2 mm^2. Spectral deconvolution used Gaussian profiles with a peak width constraint of 0.9 - 1.3 eV

and a relative area ratio of 2:1 ($(2p_{3/2}):(2p_{1/2})$).[21]

As with the samples used for thin-layer cell spectroscopy (see below), samples of whole molecule IgG were prepared by adsorbing the antibody from PBS onto an uncoated gold surface and then storing the sample overnight in a humidified chamber at room temperature. Samples of Fab'-SH and iodoacetamide-treated Fab'-SH were prepared in PB in an analogous manner. Samples of 1,9-nonanedithiol and 1-decanethiol were prepared by overnight immersion of gold substrates in ~1 mM ethanolic solutions. Prior to XPS characterization, all samples were rinsed in deionized water or ethanol and dried in an argon stream.

(iv). **Thin-Layer Spectroscopy.** A long optical path length thin-layer spectroscopy cell was constructed as previously described.[22] These cells, by virtue of their long optical pathlength and large gold surface area to solution volume ratio, provide ample sensitivity to monitor quantitatively a wide range of interfacial processes, including adsorption, desorption, and electrocatalysis.[23-26] Using these cells, experiments were conducted to determine whether the adsorption of Fab'-SH resulted in an immunosurface with a greater effective epitope density than found with whole molecule antibodies. The assessment was accomplished by monitoring the loss of both specific and nonspecific antibodies tagged with fluorescein isothiocyanate (FITC) upon injection into the cell with substrates coated with either whole molecule IgG or Fab'-SH. The exposed substrate area of the TLC was 2.54 cm^2. The spectroscopic data were collected using a Hewlett-Packard 8452A diode array spectrophotometer.

Reagents. Lyophilized polyclonal rabbit $F(ab')_2$ (Organon Teknica and ICN

Biomedical) and lyophilized polyclonal goat IgG and rabbit IgG (Sigma) were reconstituted according to vendor specifications. Affinity-isolated, antigen-specific, FITC-conjugated polyclonal goat anti-rabbit IgG and rabbit anti-goat IgG, 2-MEA, and iodoacetamide were purchased from Sigma and used as received. 1-Decanethiol and 1,9-nonanedithiol were purchased from Aldrich and used as received. Stock solutions of 2-MEA were prepared in PB. The vendor-specified extinction coefficients for the FITC-labeled goat anti-rabbit IgG and rabbit anti-goat IgG at 495 nm were 0.15 and 0.2 cm^{-1} $(mg/mL)^{-1}$, respectively.

Results and Discussion

XPS Characterizations. To assess whether the immobilization of Fab'-SH on gold results in the formation of a gold-bound thiolate, characterizations in the S(2p) binding energy region were conducted using XPS. The S(2p) region is characterized by a doublet (i.e., $2p_{3/2}$ and $2p_{1/2}$) between 160 and 180 eV that arises from spin-orbit coupling.[27] For most thiols and disulfides, this region is dominated by the more intense $2p_{3/2}$ band that lies between 163 and 165 eV and is ~1 eV lower in energy than the $2p_{1/2}$ band. In contrast, monolayers derived by the chemisorption of thiols and disulfides at gold have a binding energy for each component of the 2p doublet that is ~1 eV lower than those of their precursors.

The results of these characterizations are presented in Figure 2. Figure 2A is an XPS spectrum for gold modified with rabbit Fab'-SH, whereas Figure 2B is that for gold modified with whole molecule rabbit IgG. For comparison purposes, Figure 2C is an XPS spectrum for gold modified with 1,9-nonanedithiol and Figure 2D is that for gold modified with

1-decanethiol. All four spectra have been deconvoluted using the constraints described in the Experimental Section. The spectrum from the dithiol-modified surface (Figure 2C) contains two sets of doublets, indicating the presence of two chemically distinct forms of sulfur.[27,28] The higher binding energy doublet, centered at 164.9 and 163.7 eV, can be assigned respectively to the $2p_{1/2}$ and $2p_{3/2}$ of sulfur as a thiol, whereas the lower binding energy doublet, centered at 163.0 and 162.0 eV, can be respectively assigned to the $2p_{1/2}$ and $2p_{3/2}$ of sulfur as gold-bound thiolate. The latter assignment is confirmed by the single doublet present in the 1-decanethiol-modified surface (Figure 2D). In Figure 2D, the doublet, centered at 163.1 and 162.0 eV, arises from the $2p_{1/2}$ and $2p_{3/2}$ of sulfur as thiolate, the only detectable form of sulfur present in this adlayer.

Although difficult to dissect quantitatively, the envelope for gold modified with Fab'-SH (Figure 2A) is much broader than that for the gold modified with whole molecule IgG (Figure 2B). Importantly, the broadening for the Fab'-SH modified sample occurs on the low- energy side of the envelope for the whole molecule-modified sample. Deconvolution of the Fab'-SH surface reveals two sets of doublets; the lower energy doublet is centered at 162.9 and 161.9 eV and is in good agreement with the thiolate doublets in Figures 2C,D. The envelope in the spectrum for Figure 2B, which includes the $S(2p_{1/2})$ and $S(2p_{3/2})$ bands at 165.5 and 164.2 eV, respectively, is consistent with the presence of the sulfur that forms the intact disulfides of whole molecule IgG. Similarly, Figure 2A is diagnostic of the presence of adsorbed Fab'-SH that contains disulfides (165.2 ($2p_{1/2}$) and 163.9 eV ($2p_{3/2}$)) and gold-bound thiolates (162.9 ($2p_{1/2}$) and 161.9 eV ($2p_{3/2}$)). These results, while not quantifiable because of the low signal-to-noise ratio and considerations of XPS depth sensitivity, clearly

indicate that a portion of the sulfur in Fab'-SH is present in the adlayer as gold-bound thiolate.

The spectrum (Figure 2E) taken of gold modified with Fab'-SH fragments in which the sulfhydryl group was converted to a thioether by treatment with iodoacetamide supports the interpretation of Figures 2A,B. Thioethers adsorb on gold with both C-S linkages intact.[21] Moreover, the S(2p) couplet for an adsorbed thioether is indistinguishable from that of its precursor (164.4 ($2p_{1/2}$) and 163.2 eV ($2p_{3/2}$))[21] as well as that of unbound disulfide. The conversion of the sulfhydryl group to a thioether moiety can then be used to assess whether the presence of the gold-bound thiolate in the Fab'-SH adlayer is a consequence of a reaction of the sulfhydryl group or of the chemisorbed-induced cleavage of any of the four disulfides in the Fab'-SH fragment. These results reveal features strongly diagnostic of sulfur present as disulfides and thioethers and at most a hint of a feature suggestive of a small amount of sulfur as a thiolate. The low signal strength of the features in Figure 2E with respect to those in Figure 2A further indicates that the presence of the sulfhydryl group results in a larger coverage for Fab'-SH than for the thiolether-modified Fab'-SH. We therefore believe that the sulfhydryl species in Fab'-SH binds to gold as a chemisorbed thiolate and plays an important role in the adsorption process. The next several sections critically assess the viability of these potentially intriguing immunosurfaces.

Thin-Layer Cell Spectroscopy. To determine whether Fab'-SH forms an immunosurface with a higher epitope density than a coating of whole molecule IgG, experiments using thin-layer cell (TLC) spectroscopy[22,29-31] were performed. Using this technique, we monitored the change in the absorbance of FITC-labeled antibodies upon

injection into the small solution cavity of the TLC. The decrease in absorbance that is observed when the solution-based antibody binds to the antigenic surface is used to estimate the number of available epitopes on the coated surface.

Figure 3A is a representative absorbance versus time trace for a solution of FITC-conjugated goat anti-rabbit IgG that was injected into a TLC cell containing an antigenic rabbit Fab'-SH surface. As evident, the absorbance observed upon injection of the solution into the TLC gradually decreases to a lower constant level. This decrease corresponds to the average loss of $2.8 \times 10^{13} \pm 4.1 \times 10^{12}$ (n = 4) labeled IgG molecules from the solution cavity. Figure 3B is a representative trace for the same type of experiment except that the gold surface is modified with whole molecule goat IgG and the solution contains FITC-labeled rabbit anti-goat IgG. The decrease in absorbance for the whole molecule antigenic surface reflects the average loss of $8.1 \times 10^{12} \pm 1.5 \times 10^{12}$ (n = 3) labeled IgG molecules. The absorbance decreases in both cases are attributed to the specific binding of the labeled IgG to each of the antigenic surfaces. We note that the shapes of both curves, which are indicative of multiple-step adsorption processes,[32,33] are representative of repeated trials performed in each system and are similar to those previous reported.[32-35]

To confirm that the absorbance decreases result from the specific binding of the labeled IgG to the modified gold surfaces and not from nonspecific adsorption onto any other portion of the sample or the TLC, several control experiments were conducted. Figure 3C presents the results of one such an experiment whereby a solution of FITC-conjugated goat anti-rabbit was injected into the TLC containing a surface modified with whole molecule goat IgG. No detectable change in absorbance is observed over the course of the experiment. This

result confirms that the absorbance decreases in Figures 3A,B arise from the loss of labeled IgG because of its specific binding on the coated substrates.

The binding data indicate that the surface modified with a monolayer of Fab'-SH fragments contains nearly 4 times as many viable epitopes per square centimeter as the surface modified with whole molecule antibodies. In other words, a Fab'-SH modified surface has an average of 1.1×10^{13} epitopes/cm^2 whereas a whole molecule-modified surface has an average of 3.2×10^{12} epitopes/cm^2. We suspect that the lower number of epitopes on the whole molecule surface may be due, in part, to surface induced denaturation. Gold is a high free energy surface, and recent investigations[36-39] argue that globular proteins undergo conformational changes upon adsorption, some of which may degrade epitope structures. It is intriguing to consider that thiolate bond formation to gold may minimize the surface-induced denaturation of a population of adsorbed Fab'-SH fragments. It is, however, unclear as to how the presence of the sulfhydryl species results in this minimization. With such systems, adsorption is a complex mixing of enthalpic and entropic considerations,[40] and we have not yet identified the energetic factors of importance for Fab'-SH adsorption. We are also uncertain whether a thiolate-directed orientation of the adsorbate may play a role. Interestingly, Caruso and co-workers found that antibodies modified with Traut's reagent, a reagent that converts free amines to sulfhydryl groups, and adsorbed on gold could bind twice the number of solution antigens as unmodified antibodies directly adsorbed onto gold.[41] Because the amines and therefore the sulfhydryl groups are distributed throughout the antibody structure, we suspect that thiolate bond formation is most likely not conferring any orientational advantage but, rather, may be affecting the structural viability of the

immobilized antibodies. Our result with antigenic surfaces is in accord with their observations.

AFM and Confocal Fluorescence Imaging. Characterizations using AFM and confocal fluorescence microscopy were carried out to evaluate the effectiveness of each step in the array fabrication at a microscopic level. Figure 4 presents in situ AFM images of the photopatterned surfaces prepared in Steps 1 and 2, i.e., a gold substrate modified with a fluorinated alkanethiolate monolayer only in the grid regions. The topographic image at most hints at the presence of the patterned surface created in steps 1-2. As proposed in earlier investigations,[4,42] the inability to detect the 1.5–2.0 nm[12] difference in the height of the uncoated squares and the fluorinated monolayer-coated grids likely arises from the simultaneous contact of the tip with both parts of the array at the boundary between the squares and grids.

In contrast to the topographic image, the concurrent friction image in Figure 4B reveals an array composed of squares and grids. The shapes and the dimensions of the two elements of the image (grids, ~5 μm wide and squares, ~7.5 μm wide) are consistent with the expected photopattern created using a 2000-mesh TEM grid. Moreover, the friction image confirms a compositional difference between the grids and the squares, with the squares having a higher friction than the grids. Several laboratories,[43-45] including our own,[46] have recently shown that the friction observed at the microcontact formed between a high surface free energy Si_3N_4 tip (i.e., an uncoated tip) and a sample with high surface free energy is larger than the friction observed for a sample with low surface free energy. Since the uncoated gold squares have a higher surface free energy than the fluorinated grids,[12] it

follows that the exposed gold squares of the photopatterned surfaces should exhibit a higher friction than the fluorinated grids. This result confirms the validity of steps 1 and 2 in the patterning process.

We next examined the effectiveness of step 3, i.e., the reliability of immobilizing viable rabbit Fab'-SH in the square regions of the pattern. This assessment was conducted using tapping mode AFM (TM-AFM) in order to reduce any contact-induced distortion of the topographic image.[47-49] This concern results from our earlier assessments of this immunoassay readout strategy[4] whereby the detected height changes were consistently larger when determined in tapping mode.

Figure 5A is an in situ TM-AFM height image for a patterned gold surface ~30 min after injection of a Fab'-SH solution into the cell. The height of the Fab'-SH layer is 4.4 nm larger than the fluorinated alkanethiolate monolayer in the grids (~1.5– 2 nm[12]). This value is consistent with the molecular dimensions of Fab'-SH determined by others[50] after accounting for image distortions that arise from the finite size and shape of the probe tip.[51] This magnitude in the change in topography was observed in images of several samples and for different locations on each sample.

To demonstrate the viability of the Fab'-SH array, an antibody specific to the Fab'-SH surface was introduced into the imaging cell. Figure 5B is an in situ tapping mode height image of a different location of the same sample used in Figure 5A that was obtained ~15 min after injection of a dilute binding buffer solution of FITC-labeled goat anti-rabbit IgG into the cell. Cross section analysis of Figure 5B reveals a height difference of 8.6 nm, approximately double that obtained with only Fab'-SH fragments on the surface. This

increase is consistent with the specific binding of goat anti-rabbit to the Fab'-SH-based array, thereby documenting that the Fab'-SH array is viable and contains intact epitopes.

Another confirmation of the viability and specificity of the immobilized Fab'-SH array is provided by the confocal fluorescence microscopic images presented in Figure 6. Figure 6A is an in situ fluorescence image (75 μm x 75 μm) obtained after the exposure of an antigenic Fab'-SH array to FITC-labeled specific antibody. As evident, the image is composed of a defined fluorescent pattern of 7.5-μm squares that are surrounded by nonfluorescent 5-μm-wide grids. This result indicates that the Fab'-SH array is viable as an immunosensing surface, with the regions of strong fluorescence corresponding to those displaying the height changes in Figure 5B that are diagnostic of the specific binding of the antibody to the antigenic array.

Figure 6B is a fluorescence image of a Fab'-SH array after the addition of FITC-labeled nonspecific antibodies. The absence of a detectable fluorescent pattern demonstrates that the Fab'-SH array contains viable epitopes that are only recognizable by the antibody raised against the immobilized antigen. Therefore, the cleavage process and subsequent immobilization of the fragments to the bare gold squares produces a viable immunosurface.

Conclusions and Future Work

Rabbit Fab'-SH fragments have been used to construct viable antigenic immunosurfaces on gold. X-ray photoelectron spectroscopy (XPS) argues that the immobilization of Fab'-SH fragments involves the free sulfhydryl group created in the fragment during the controlled reduction process of rabbit $F(ab')_2$ and results in the formation

of a gold-bound thiolate. TLC spectroscopic investigations reveal that an antigenic Fab'-SH monolayer on gold contains ~4 times more intact epitopes per square centimeter than an antigenic monolayer of whole molecule antibodies, a property that may prove useful in the detection of lower affinity antibodies and, therefore, earlier detection of disease. These studies suggest that thiolate bond formation regulates adsorption in a way that results in immunosurfaces of larger epitope density than those prepared with adsorbed whole molecule antibodies. Furthermore, attachment through spontaneous chemisorption to gold eliminates the need for chemical linkers, simplifying the array fabrication process. Finally, both in situ AFM characterizations and fluorescence assays conducted on compositionally patterned surfaces of Fab'-SH fragments demonstrated that the coatings are viable immunosurfaces. Experiments to further assess the role of the sulfhydryl group in controlling orientation, along with evaluations of whether higher epitope densities enhance the detection of lower affinity antibodies, are planned.

Acknowledgements

J.C.O. gratefully acknowledges the support of a Phillips Petroleum Corporation graduate research fellowship. We also express our appreciation to James Anderegg and Chuan-Jian Zhong for the XPS characterizations as well as N. J. Simmons and G. B. Dawson for assistance in the thin-layer cell measurements. We further acknowledge J. A. Harnish for synthesizing the fluorinated monolayer and J. R. Kenseth and J. D. Burgess for their insightful discussions during the preparation of this manuscript. This work was supported in part by the National Science Foundation (Grant No. BIR-9601789), the Microanalytical

Instrumentation Center and the Laboratory for Cellular Signaling of Iowa State University, and the Office of Basic Energy Science, Chemical Sciences Division of the U.S. Department of Energy. The Ames Laboratory is operated for the U.S. Department of Energy by Iowa State University under Contract W-7405-eng-82.

References

(1) Lew, A. M. *J. Immunol. Methods* **1984**, *72*, 171.

(2) Nimmo, G. R.; Lew, A. M.; Stanley, C. M.; Steward, M. W. *J. Immunol. Methods* **1984**, *72*, 177.

(3) Werthen, M.; Nygren, H. *J. Immunol. Meth.* **1988**, *115*, 71.

(4) Jones, V. W.; Kenseth, J. R.; Porter, M. D.; Mosher, C. L.; Henderson, E. *Anal. Chem.* **1998**, *70*, 1233.

(5) Wimalasena, R. L.; Wilson, G. S..*J. Chromatogra.* **1991**, *572*, 85.

(6) Nakanishi, K.; Muguruma, H.; Karube, I. *Anal. Chem.* **1996**, *68*, 1695.

(7) Lu, B.; Xie, J.; Lu, C.; Wu, C.; Wei, Y. *Anal. Chem.* **1995**, *67*, 83.

(8) Prisyazhnoy, V. S.; Fusek, M.; Alakhov, Y. B. *J. Chromatogra.* **1988**, *424*, 243.

(9) Vikholm, I.; Albers, W. M. *Langmuir* **1998**, *14*, 3865.

(10) Alarie, J. P.; Sepaniak, M. J.; Vo-Dinh, T. *Anal. Chim. Acta* **1990**, *229*, 169.

(11) Droz, E.; Taborelli, M.; Descouts, P.; Wells, T. N. C.; Werlen, R. C. *J. Vac. Sci. Technol. B.* **1996**, *14*, 1422.

(12) Alves, C. A.; Porter, M. D. *Langmuir* **1993**, *9*, 3507.

(13) Porter, M. D.; Bright, T. B.; Allara, D. L.; Chidsey, C. E. D. *J. Am. Chem. Soc.* **1987**, *109*, 3559.

(14) Somogyi, A.; Kane, T. E.; Ding, J.-M.; Wysocki, V. H. *J. Am. Chem. Soc.* **1993**, *115*, 5275.

(15) Tarlov, M. J.; Burgess, Jr. D. R. F.; Gillen, G. *J. Am. Chem. Soc.* **1993**, *115*, 5305.

(16) Huang, J.; Hemminger, J. C. *J. Am. Chem. Soc.* **1993**, *115*, 3342.

(17) Lewis, M.; Tarlov, M.; Carron, K. *J. Am. Chem. Soc.* **1995**, *117*, 9574.

(18) Jeske, D. J.; Capra, J. D. In *Fundamental Immunology*; Paul, W. E., Ed.; Raven Press: New York, 1984; p 131.

(19) Parham, P. In *Handbook of Experimental Immunology*; 4 ed.; Weir, D. M., Ed.; Blackwell Scientific Publications: Oxford, 1986; Vol. 1; p 14.1.

(20) Stanworth, D. R.; Turner, M. W. In *Handbook of Experimental Immunology*; 3 ed.; Weir, D. M., Ed.; Blackwell Scientific Publications: Oxford, 1978; p 6.1.

(21) Zhong, C.-J.; Brush, R. C.; Anderegg, J.; Porter, M. D. *Langmuir* **1999**, *15*, 518.

(22) Simmons, N. J.; Porter, M. D. *Anal. Chem.* **1997**, *69*, 2866.

(23) Zak, J.; Porter, M. D.; Kuwana, T. *Anal. Chem.* **1983**, *55*, 2219.

(24) Gui, Y.-P.; Porter, M. D.; Kuwana, T. *Anal. Chem.* **1985**, *57*, 1474.

(25) Gui, Y.-P.; Kuwana, T. *Langmuir* **1986**, *2*, 471.

(26) Gui, Y.; Kuwana, T. *J. Electroanal. Chem.* **1987**, *222*, 321.

(27) Castner, D. G.; Hinds, K.; Grainger, D. W. *Langmuir* **1996**, *12*, 5083.

(28) Tour, J. M.; Jones III, L.; Pearson, D. L.; Lamba, J. J. S.; Burgin, T. P.; Whitesides, G. M.; Allara, D. L.; Parikh, A. N.; Atre, S. V. *J. Am. Chem. Soc.* **1995**, *117*, 9529.

(29) Yao, C. L.; Capdevielle, F. J.; Kadish, K. M.; Bear, J. L. *Anal. Chem.* **1989**, *61*, 2805.

(30) Flowers, P. A.; Mamantov, G. *Anal. Chem.* **1989**, *61*, 190.

(31) Rubinson, K. A.; Mark, Jr., H. B. *Anal. Chem.* **1982**, *54*, 1204.

(32) Yang, M.; Chung, F. L.; Thompson, M. *Anal. Chem.* **1993**, *65*, 3713.

(33) Sarkar, D.; Chattoraj, D. K. *Indian J. Biochem. Biophys.* **1992**, *29*, 135.

(34) Caruso, F.; Rodda, E.; Furlong, D. N. *J. Colloid Interface Sci.* **1996**, *178*, 104.

(35) Hook, F.; Rodahl, M.; Brzezinski, P.; Kasemo, B. *Langmuir* **1998**, *14*, 729.

(36) Liedberg, B.; Ivarsson, B.; Hegg, P.-O.; Lundstrom, I. *J. Colloid Interface. Sci* **1986**, *114*, 386.

(37) Sundgren, J.-E.; Bodo, P.; Ivarsson, B.; Lindstrom, I. *J. Colloid Interface Sci.* **1986**, *113*, 530.

(38) Nicholov, R.; Lum, N.; Veregin, R. P. N.; DiCosmo, F. In *Proteins at Interfaces II: Fundamentals and Applications*; Horbett, T. A., Brash, J. L., Eds.; American Chemical Society: Washington, D.C., 1995; p 280.

(39) Atkinson, P. J.; Dickinson, E.; Horne, D. S.; Richardson, R. M. In *Proteins at Interfaces II: Fundamentals and Applications*; Horbett, T. A., Brash, J. L., Eds.; American Chemical Society: Washington, D.C., 1995; p 311.

(40) Yan, G.; Li, J.-T.; Huang, S.-C.; Caldwell, K. D. In *Proteins at Interfaces II: Fundamentals and Applications*; Horbett, T. A., Brash, J. L., Eds.; American Chemical Society: Washington, D.C., 1995; p 256.

(41) Caruso, F.; Rodda, E.; Furlong, D. N. *J. Colloid Interface. Sci.* **1996**, *178*, 104.

(42) Hayes, W. A.; Kim, H.; Yue, X.; Perry, S. S.; Shannon, C. *Langmuir* **1997**, *13*, 2511.

(43) Wilbur, J. L.; Biebuyck, H. A.; MacDonald, J. C.; Whitesides, G. M. *Langmuir* **1995**, *11*, 825.

(44) Zhou, Y.; Fan, H.; Fong, T.; Lopez, G. P. *Langmuir* **1998**, *14*, 660.

(45) Frisbie, C. D.; Rozsnyai, L. F.; Noy, A.; Wrighton, M. S.; Lieber, C. M. *Science* **1994**, *265*, 2071.

(46) Green, J.-B. D.; McDermott, M. T.; Porter, M. D.; Siperko, L. M. *J. Phys. Chem.* **1995**, *99*, 10960.

(47) Magonov, S. N.; Reneker, D. H. *Annu. Rev. Mater. Sci.* **1997**, *27*, 175.

(48) Finot, M. O.; McDermott, M. T. *J. Am. Chem. Soc.* **1997**, *119*, 8564.

(49) Noy, A.; Sanders, C. H.; Vezenov, D. V.; Wong, S. S.; Lieber, C. M. *Langmuir* **1998**, *14*, 1508.

(50) Luginbuhl, R.; Collioud, A.; Seigenthaler, H.; Sigrist, H. In *Forces in Scanning Probe Methods*; Guntherodt, H. J., Ed.; Kluwer Academic Publishers: New York, 1995; p 615.

(51) Vesenka, J.; Miller, R.; Henderson, E. *Rev. Sci. Instrum.* **1994**, *65*, 2249.

Figure Captions

Figure 1. Idealized representation of Fab'-SH fragments chemisorbed to gold.

Figure 2. XPS data in the S(2p) binding regions for rabbit Fab'-SH (A), whole molecule rabbit IgG (B), and iodoacetamide-treated rabbit Fab'-SH (E) modified gold substrates. The spectra for 1,9-nonanedithiol (C) and 1-decanethiol (D) on gold are included for comparison. Spectra A and B were acquired in 36 min, spectra C and D

in 12 min, and spectrum E in 53 min.

Figure 3. Absorbance versus time traces at 495 nm using a thin-layer cell for (A) rabbit Fab'-SH modified gold exposed to FITC-labeled goat anti-rabbit IgG (extinction coefficient : 0.15 cm^{-1} $(mg/mL)^{-1}$) and (B &C)) whole molecule goat IgG modified gold exposed to (B) FITC-labeled rabbit anti-goat (extinction coefficient: 0.2 cm^{-1} $(mg/mL)^{-1}$) and (C) FITC-labeled goat anti-rabbit IgG (extinction coefficient: 0.15 cm^{-1} $(mg/mL)^{-1}$).

Figure 4. AFM contact mode height (A) and friction (B) images (70 μm x 70 μm) obtained in binding buffer of the patterned array (i.e., step 2). The cross-sectional analysis was performed by averaging the individual line scans contained in the boxed area of the array contained in the images.

Figure 5. (A) AFM tapping mode height image and height cross section of a rabbit Fab'-SH array (40 μm x 40 μm) obtained in binding buffer ~30min after injection (5 μL of 5 μg/μL) of Fab'-SH fragments (final concentration in cell: 0.5 μg/μL). The cross-sectional analysis was performed by averaging the height of the individual line scans contained in the boxed area of the array. (B) AFM tapping mode height image and height cross-section of a rabbit Fab'-SH array (40 μm x 40 μm) after the addition of goat anti-rabbit FITC-tagged secondary antibodies (5 μL injection of 0.1 mg/mL; final concentration in cell: 0.01 μg/μL). The cross-sectional analysis was performed by averaging the height of the individual line scans contained in the boxed area of the array.

Figure 6. Fluorescence images (75 μm x 75 μm) of a rabbit Fab'-SH array after the addition

of goat anti-rabbit (A) or goat anti-mouse (B) FITC-tagged secondary antibodies. The images were obtained under deionized water.

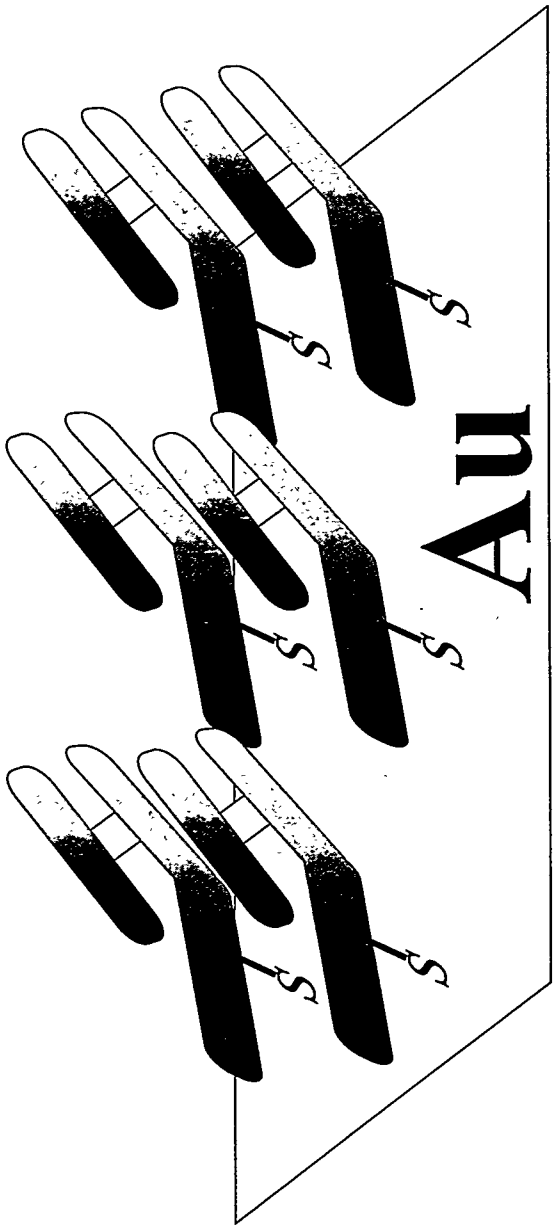

Figure 1.

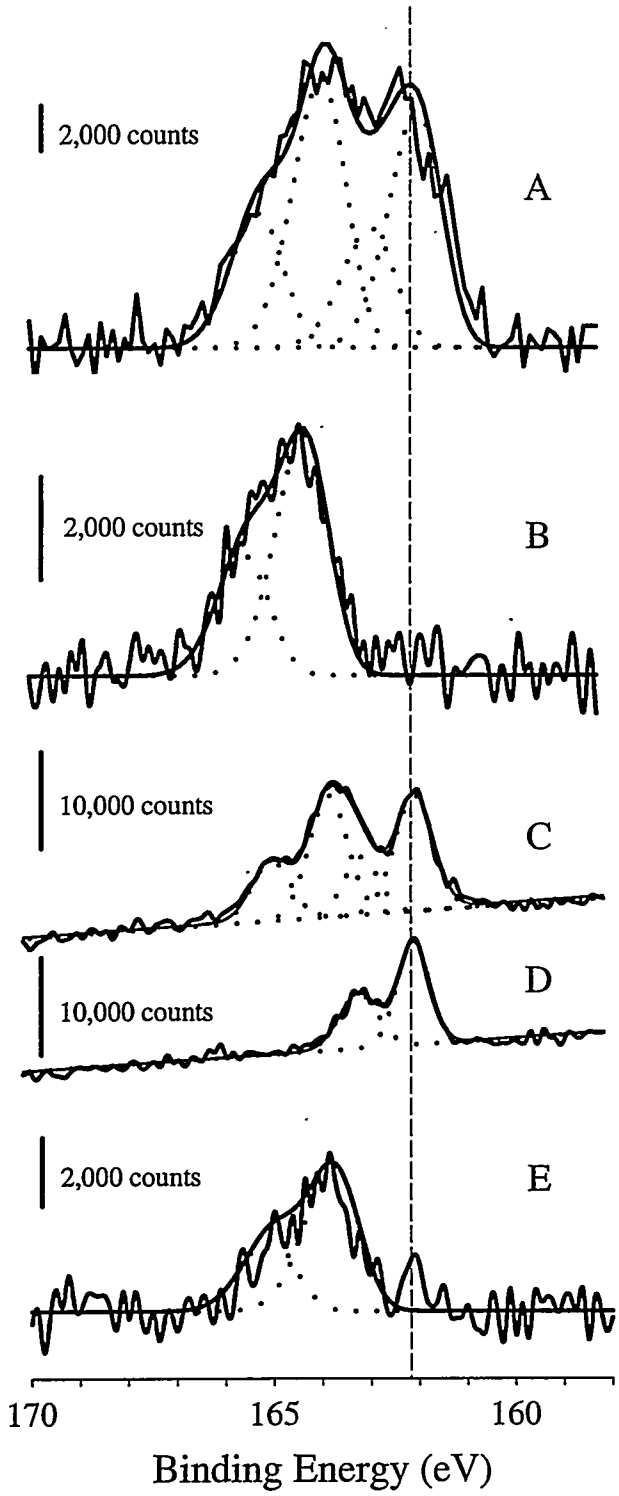
2,000 counts
A
2,000 counts
B
10,000 counts
C
10,000 counts
D
2,000 counts
E
170
165
160
Binding Energy (eV)

Figure 2.

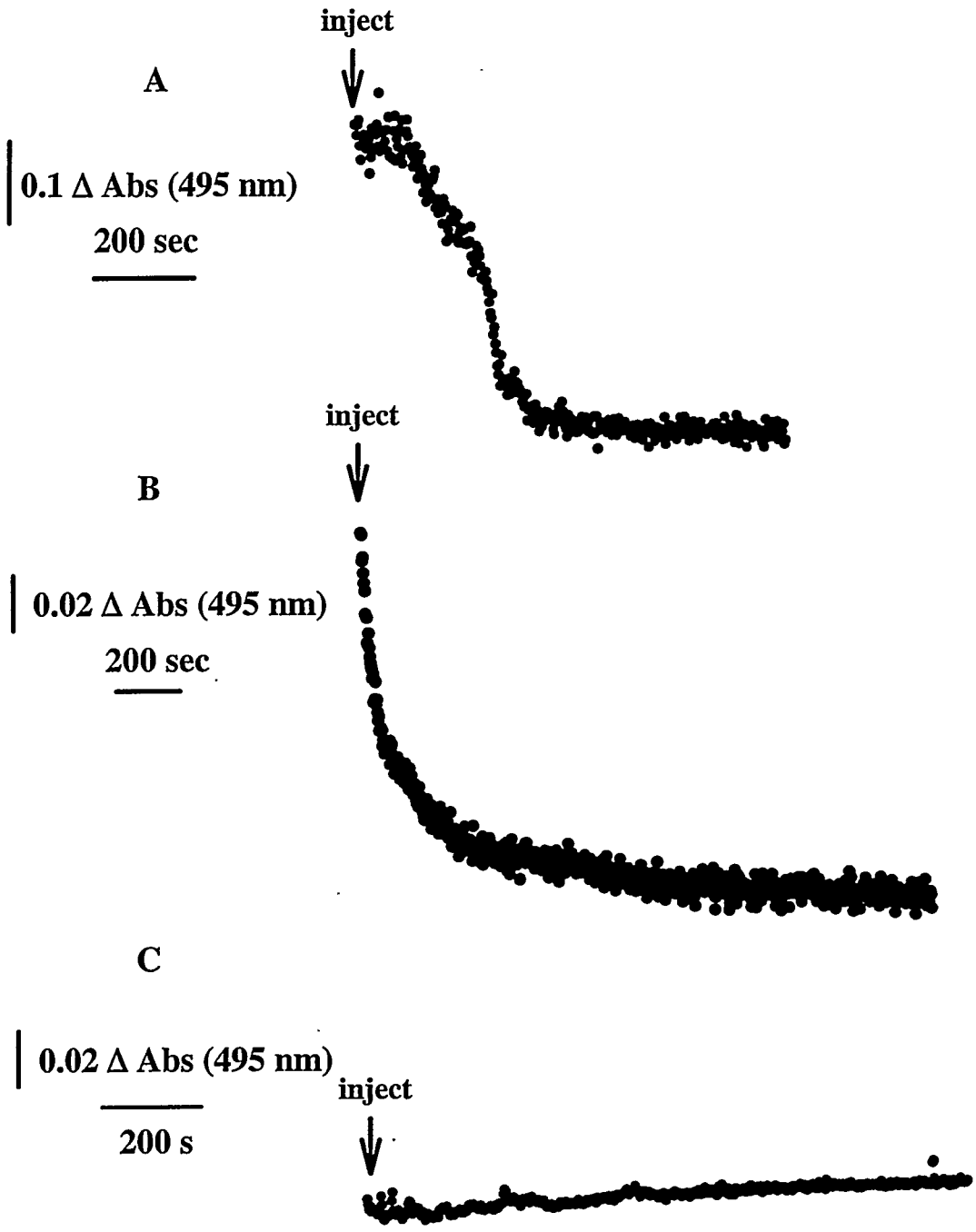
inject
A
0.1 Δ Abs (495 nm)
200 sec
inject
B
0.02 Δ Abs (495 nm)
200 sec
C
0.02 Δ Abs (495 nm)
200 s
inject

Figure 3.

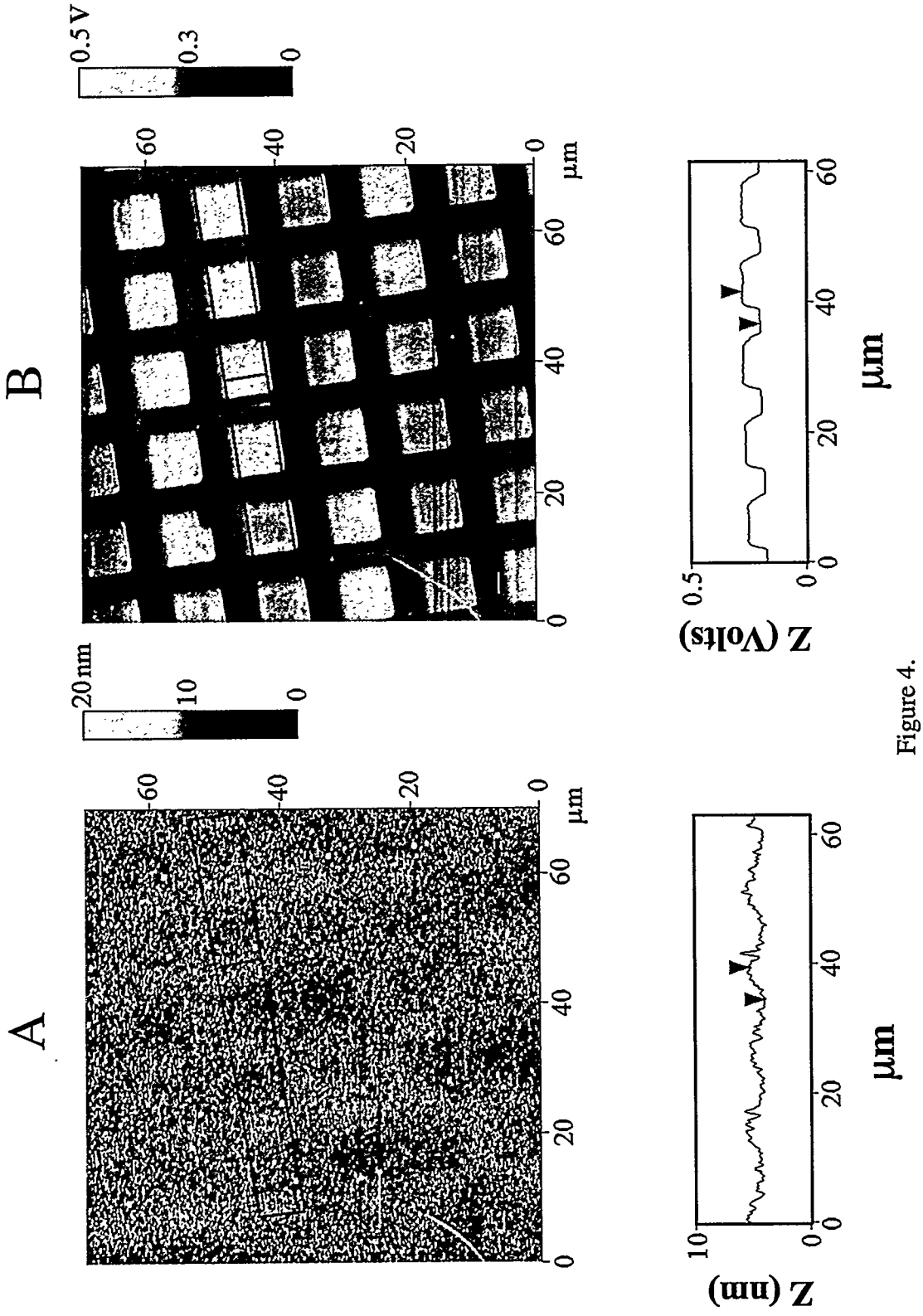

Figure 4.

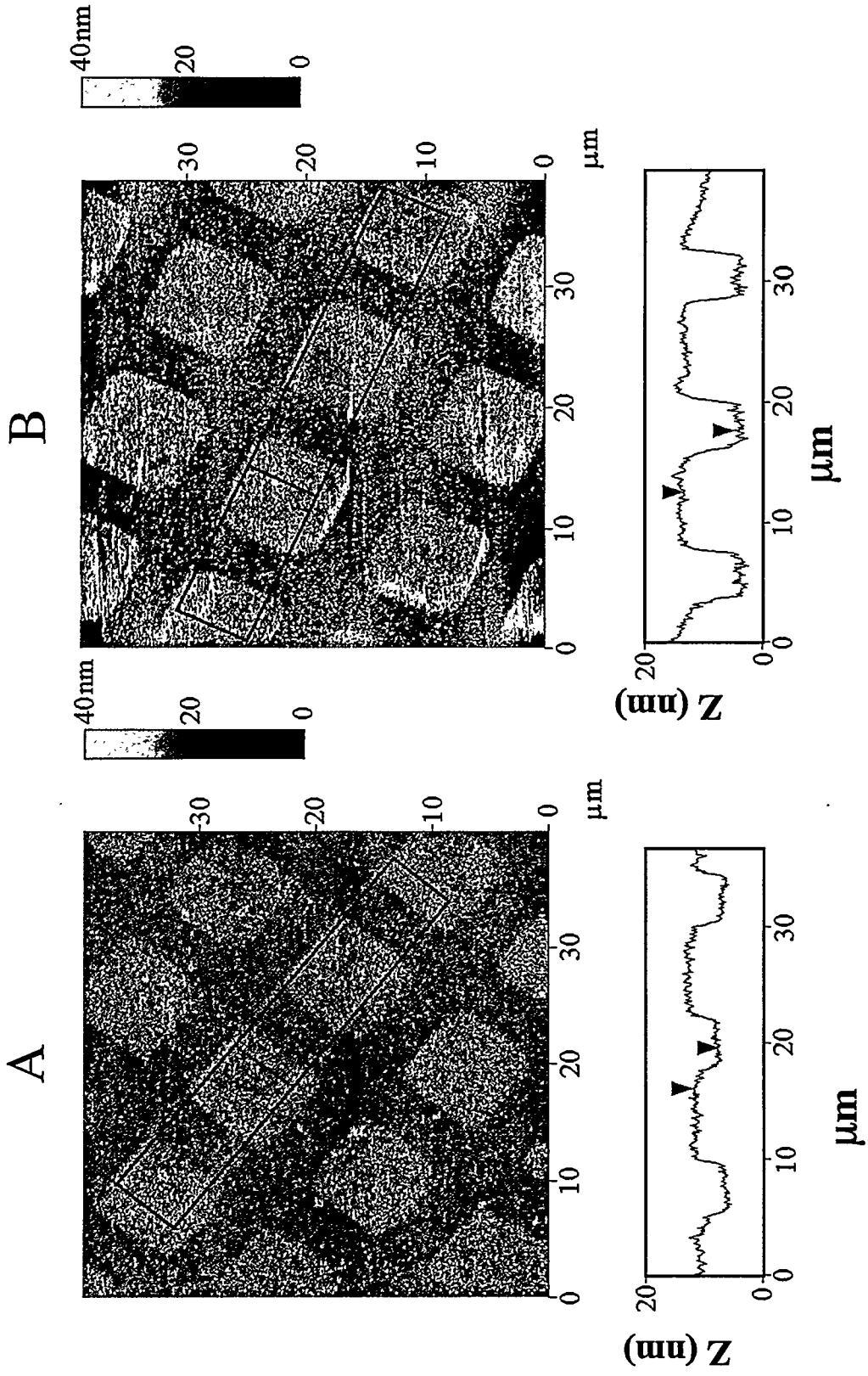

Figure 5.

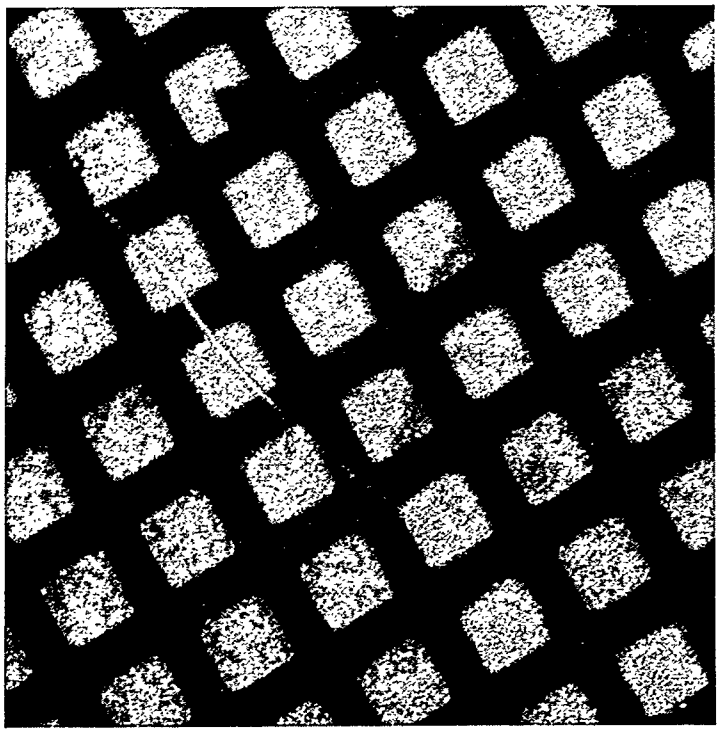

A

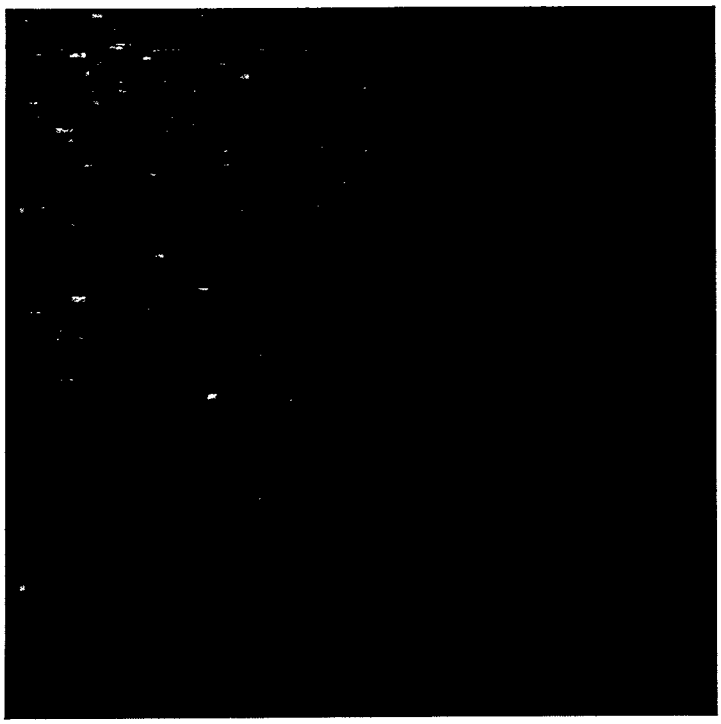

B

Figure 6.

CHAPTER 4. SELF-ASSEMBLED DOUBLE-STRANDED DNA (dsDNA) MICROARRAYS FOR PROTEIN:dsDNA SCREENING USING ATOMIC FORCE MICROSCOPY

A communication accepted to *The Journal of the American Chemical Society*

Janese C. O'Brien,[1] John T. Stickney,[2] and Marc D. Porter [1,3]

Abstract

A novel method for creating and interrogating double-stranded DNA (dsDNA) microarrays suitable for screening protein:dsDNA interactions is described. The approach combines the ease of self-assembled monolayer technology with the high resolution imaging capability of atomic force microscopy (AFM). The arrays are formed by the direct deposition of intact dsDNA that contains a disulfide modifier and a restriction enzyme recognition sequence. The disulfides drive duplex self-assembly onto array elements photopatterned in a gold-bound fluorinated alkanethiolate monolayer. Importantly, the position of the recognition sequence within a duplex is such that the topographic change after enzymatic cleavage is readily detectable by AFM, with the surrounding fluorinated monolayer acting as an internal height reference plane. Results are presented that demonstrate concept feasibility. Issues related to manipulating the architecture for assay optimization are discussed, and strategies for use of this concept as a tool for the rapid and facile screening of multiple protein reactions are briefly described.

---

[1] Microanalytical Instrumentation Center, Ames Laboratory-DOE, and Department of Chemistry, Iowa State University, Ames, Iowa 50011
[2] Department of Biochemistry, Biophysics, and Molecular Biology, Iowa State University, Ames, IA 50011
[3] Corresponding author

A novel method for creating and interrogating dsDNA microarrays suitable for screening protein:dsDNA interactions is described. Our strategy combines the ease of self-assembled monolayer technology with the ability of the atomic force microscope (AFM) to detect changes in surface topography at a subnanometer length scale. The methodology involves the direct deposition of double-stranded oligonucleotides (Fig. 1A) synthesized by exploiting the higher efficiency of off-chip phosphoramidite chemistry to 1) contain asymmetrically substituted disulfide functionalities[1] which direct their self-assembly onto gold in a single step,[2] 2) include a recognition sequence specific to a given restriction enzyme, 3) position the recognition sequence within the duplex such that enzymatic cleavage results in a topographic change readily detectable by AFM (Fig. 1B), and 4) contain a fluorescent tag[3] positioned above the recognition sequence to optically verify cleavage. The as-assembled arrays are further modified by exchange with a short chain thiol[2b] to decrease duplex density. Taken together, these steps form an adlayer in which the spatial orientation and packing density of dsDNA are well suited to function as microarrays for protein screening.

We have adopted a five-step microarray fabrication process that draws on concepts presented in our reports on height-based immunoassays[4] and on modifications to a strategy for the self-assembly of ssDNA onto gold.[5] Briefly, Step 1 forms a thiol-derived ($CF_3(CF_2)_7(CH_2)_2SH$) fluorinated monolayer on gold which serves, after photopatterning, as an internal reference plane for detection of topographic changes; its low surface free energy also minimizes nonspecific adsorption.[4b] Step 2 is the photopatterning process whereby a metallic grid (hole size: 7.5 μm, grid size: 5.0 μm) acts as a mask. Irradiation of the sample

converts the thiolate to oxygenated forms of sulfur that are rinsed off the gold surface with most organic solvents.[6] Step 3 removes the oxygenated adlayer by rinsing with ethanol to expose square-shaped regions on the underlying gold. Step 4 exposes the patterned surface to a dsDNA solution[7] and coats the exposed regions of gold with a mixed monolayer through cleavage of the disulfide linkage[2,8] attached to both duplex strands (Fig. 1A). Step 5 exchanges a portion of immobilized dsDNA with a short chain alkanethiol (i.e., $HO(CH_2)_6SH$, (MCH)).[9] This step reduces duplex density, a key factor in increasing enzymatic accessibility to specific recognition sequences within individual addresses (see below).[10]

Figs. 2 and 3 present in situ AFM topographic images and cross-sectional plots that demonstrate the diagnostic capability of our strategy. Fig. 2A shows an image for an array comprised of double-stranded 26-mers containing a recognition sequence specific for the enzyme *ECo*R1 (Fig. 1A). The 8.8 ± 1.5 nm (n=5) difference in height between grid and square regions agrees with the X-ray crystallographic prediction of 8.8 nm for a double-stranded 26-mer in its B-conformation.[11] This result demonstrates that our approach effectively immobilizes dsDNA with its strands extending along the surface normal.

Fig. 2B shows an image for an array after digestion with *ECo*R1.[12] Importantly, the difference in height between dsDNA addresses and the reference adlayer has decreased to 4.3 ± 0.8 nm (n=14). This difference is consistent with the prediction based on the position of the recognition sequence (Fig. 1) and agrees with the topographic difference found after the self-assembly of the products produced from off-chip solution digestion. The lack of a detectable optical signal from the fluorescein tag after on-chip digestion also confirms

enzymatic cleavage of the target sequence.[13] We note that digestions of microarrays with *ECo*R1 prior to exchange with MCH proved unsuccessful. This finding argues that duplex density is critical for enzymatic access to the recognition sequence.

Fig. 3 presents images acquired for an array comprised of double-stranded 26-mers containing the recognition sequence specific for the restriction enzyme *Hae*III. The heights before (8.9 nm ± 1.5 nm (n=5)) and after (8.3 nm ± 1.4 nm (n=5)) exposure to *ECo*R1 are effectively indistinguishable. There was also no detectable change in the intensity of the fluorescence pattern.[13] Both sets of data are diagnostic of the absence of the sequence specific for *ECo*R1, confirming that the observed height decrease in Fig. 2 is a direct consequence of the enzymatic cleavage of the specific recognition sequence for *ECo*R1.

Our results show that self-assembled dsDNA microarrays can be readily fabricated and used to screen protein:dsDNA interactions using the topographic imaging capabilities of AFM. As such, our approach to dsDNA microarray construction has several noteworthy attributes with respect to earlier work.[14] First, array fabrication is completely self-assembling in nature (i.e., does not require use of coupling agents), and is therefore readily amenable to mass production. Second, our double-stranded oligonucleotide sequences are prepared off-chip using conventional phosphoramidite chemistry and, as a consequence, potentially have higher fidelities than those synthesized on-chip using light-directed chemistries.[15-16] The use of AFM also potentially increases the amount of information obtained from screening by extending the conventional two-dimensional read-out of fluorescence imaging to three dimensions. By quantifying the topographic data, it may be possible to determine whether cleavage is highly specific (i.e., targets a specific recognition sequence) or nonspecific (i.e.,

exhibits star activity). Topographic increases, on the other hand, could be used to discriminate against nonspecific adsorption. Experiments that explore issues of array density, digestion time minimization, and the fabrication of smaller, uniquely-modified addresses, are currently underway.

Acknowledgements

We thank J. Harnisch for synthesizing the fluorinated alkanethiol and J.R. Kenseth for helpful discussion. This work was supported in part by the National Science Foundation, the Microanalytical Instrumentation Center, and the Office of Basic Energy Science, Chemical Sciences Division of the U.S. Department of Energy. The Ames Laboratory is operated for the U.S. Department of Energy by Iowa State University under Contract W-7405-eng-82.

References and Notes

1). C6 S-S, Glen Research.

2). (a). Nuzzo, R. G.; Zegarski, B. R.; Dubois, L. H. *J. Am. Chem. Soc.* **1987**, *109*, 733-740. (b). Biebuyck, H. A.; Whitesides, G. M. *Langmuir* **1993**, *9*, 1766-70.

3). 5'-Fluorescein Phosphoramidite, 6-FAM, Glen Research.

4). (a). Jones, V. W.; Kenseth, J. R.; Porter, M. D.; Mosher, C. L.; Henderson, E. *Anal. Chem.* **1998**, *70*, 1233-1241. (b). O'Brien, J. C.; Jones, V. W.; Porter, M. D.; Mosher, C. L.; Henderson, E. *Anal. Chem.* **2000**, 72, 703-710.

5). (a). Herne, T. M.; Tarlov, M. J. *J. Am. Chem. Soc.* **1997**, *119*, 8916-8920. (b). Peterlinz, K. A.; Georgiadis, R. M.; Herne, T. M.; Tarlov, M. J. *J. Am. Chem. Soc.* **1997**, *119*, 3401-3402.

6). Lewis, M.; Tarlov, M.; Carron, K. *J. Am. Chem. Soc.* **1995**, *117*, 9574-9575.

7). Oligonucleotides were exposed to an array formed after Step 3 for 2 hours in 1 M THAM (tris(hydroxymethyl)aminomethane) (pH 7.4).

8). Nuzzo, R. G.; Fusco, F. A.; Allara, D. L. *J. Am. Chem. Soc.* **1987**, *109*, 2358-2368.

9). Arrays created after Step 4 were exposed to 10 μM MCH (Fluka) (1 M THAM (pH 7.4), 0.1 M $MgCl_2$) for 1 h.

10). We estimate the density of dsDNA after MCH treatment to be 60% of its original value. Experiments are underway to more fully characterize oligonucleotide density.

11). Voet, D.; Voet, J. G. *Biochemistry*; 2 ed.; John Wiley and Sons, Inc.: New York, 1995, p. 853.

12). 5 μL of *ECo*R1 (12 U/μL, Promega) was diluted to 50 μL with enzyme reaction buffer (90 mM THAM (pH 7.4), 10 mM $MgCl_2$, and 50 mM NaCl) and placed on the array. Arrays were incubated in a dark, humid environment for 20 h at room temperature. Samples were then rinsed with deionized water and dried with argon. Next, 30 μL of 1 M THAM (pH 7.4) was placed on the array for 1 h at room temperature. Samples were again rinsed with deionized water and dried with argon prior to imaging.

13). O'Brien, J. C.; Stickney, J. T.; Porter, M. D., manuscript in preparation.

14). Bulyk, M. L.; Gentalen, E.; Lockhart, D. J.; Church, G. M. *Nat. Biotechnol.* **1999**, *17*, 573-577.

15). (a). Fodor, S. P. A.; Read, J. L.; Pirrung, M. C.; Stryer, L.; Lu, A. T.; Solas, D. *Science* **1991**, *251*, 767-773. (b). McGall, G. H.; Barone, A. D.; Diggelmann, M.; Fodor, S. P. A.; Gentalen, E.; Ngo, N. *J. Am. Chem. Soc.* **1997**, *119*, 5081-5090.

16). Pease, A. C.; Solas, D.; Sullivan, E. J.; Cronin, M. T.; Holmes, C. P.; Fodor, S. P. A. *Proc. Natl. Acad. Sci. USA* **1994**, *91*, 5022-5026.

Figure Captions

Figure 1. (A) Disulfide-modified double-stranded 26-mer containing the recognition sequence (in bold) specific for *ECo*R1. X-ray crystallography predicts the lengths of 8.8 nm and 4.4 nm for the intact and cleaved oligonucleotides in their B-conformation,[11] respectively. Each 26-mer was labeled with fluorescein (F*) at the 5'-end for use in optical verification of sequence specific cleavage. The "T" on end of the 3'-thiol-modified oligonucleotide was the "dummy base" used to make the 3'-modification. (B) Conceptualized topographic change after exposure of dsDNA microarray to *ECo*R1.

Figure 2. In situ AFM topographic images (80 μm x 80 μm) of a dsDNA microarray containing the recognition sequence specific for *ECo*R1. The images were collected before (A) and after (B) digestion with *ECo*R1. The cross-sectional contours below each image reflect the average of the individual scan lines contained in the area of a single row of the array. The in situ images were obtained in 10 mM THAM (pH 7.4) at a scan rate of 1 Hz.

Figure 3. In situ AFM topographic images (80 μm x 80 μm) of a dsDNA microarray containing the recognition sequence specific (in bold) for *Hae*III (5'-GGG AAA GGG AGG CCC AAA GGG AAA GG-3'). The images were collected before (A) and after (B) digestion with *ECo*R1. See Fig. 2 caption for further details.

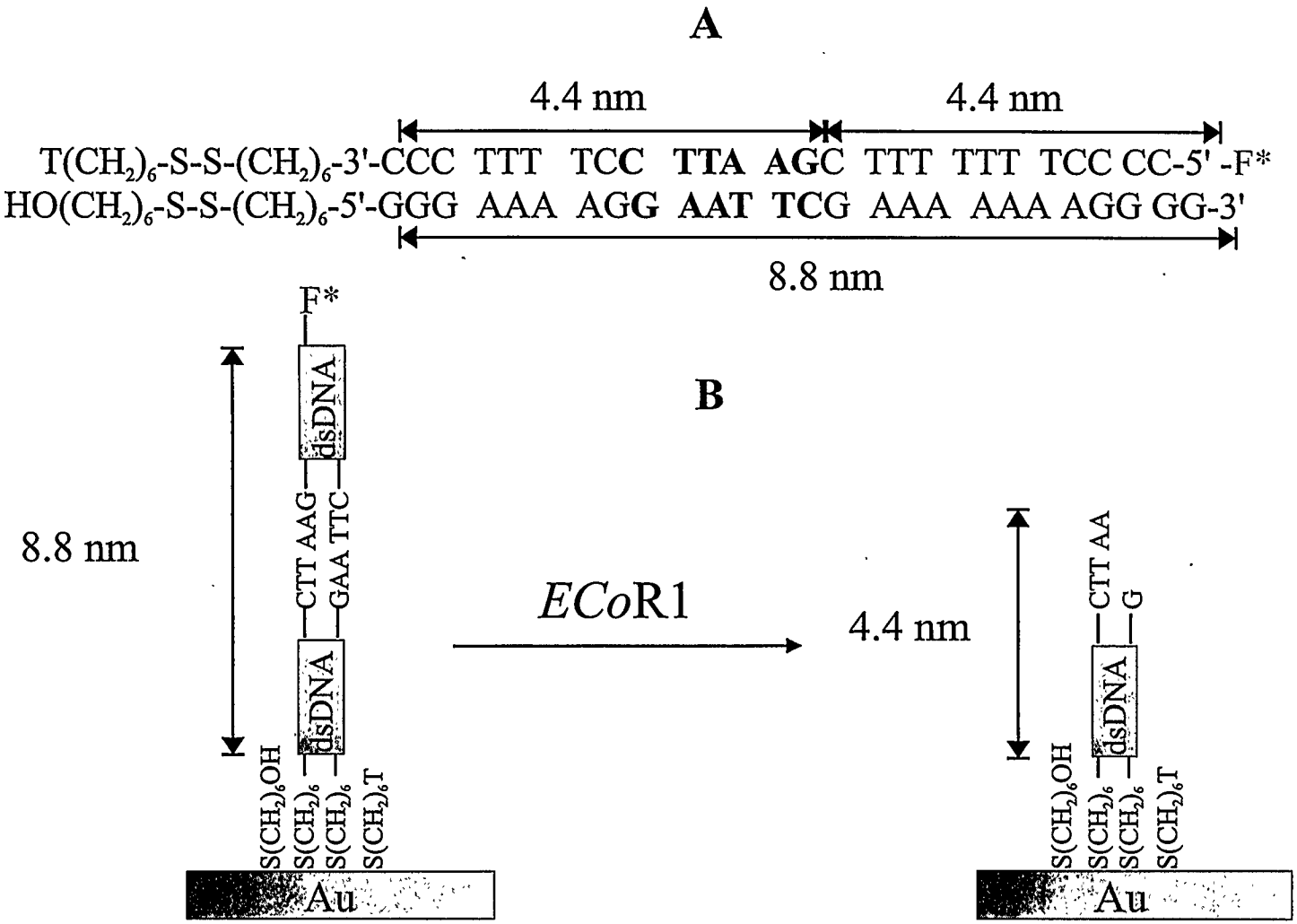
A
4.4 nm
4.4 nm
T(CH2)6-S-S-(CH2)6-3'-CCC TTT TCC TTA AGC TTT TTT TCC CC-5' -F*
HO(CH2)6-S-S-(CH2)6-5'-GGG AAA AGG AAT TCG AAA AAA AGG GG-3'
8.8 nm
B
8.8 nm
F*
dsDNA
CTT AAG
GAA TTC
dsDNA
S(CH2)6OH
S(CH2)6
S(CH2)6
S(CH2)6T
Au
ECoR1
4.4 nm
CTT AA
G
dsDNA
S(CH2)6OH
S(CH2)6
S(CH2)6
S(CH2)6T
Au

Figure 1.

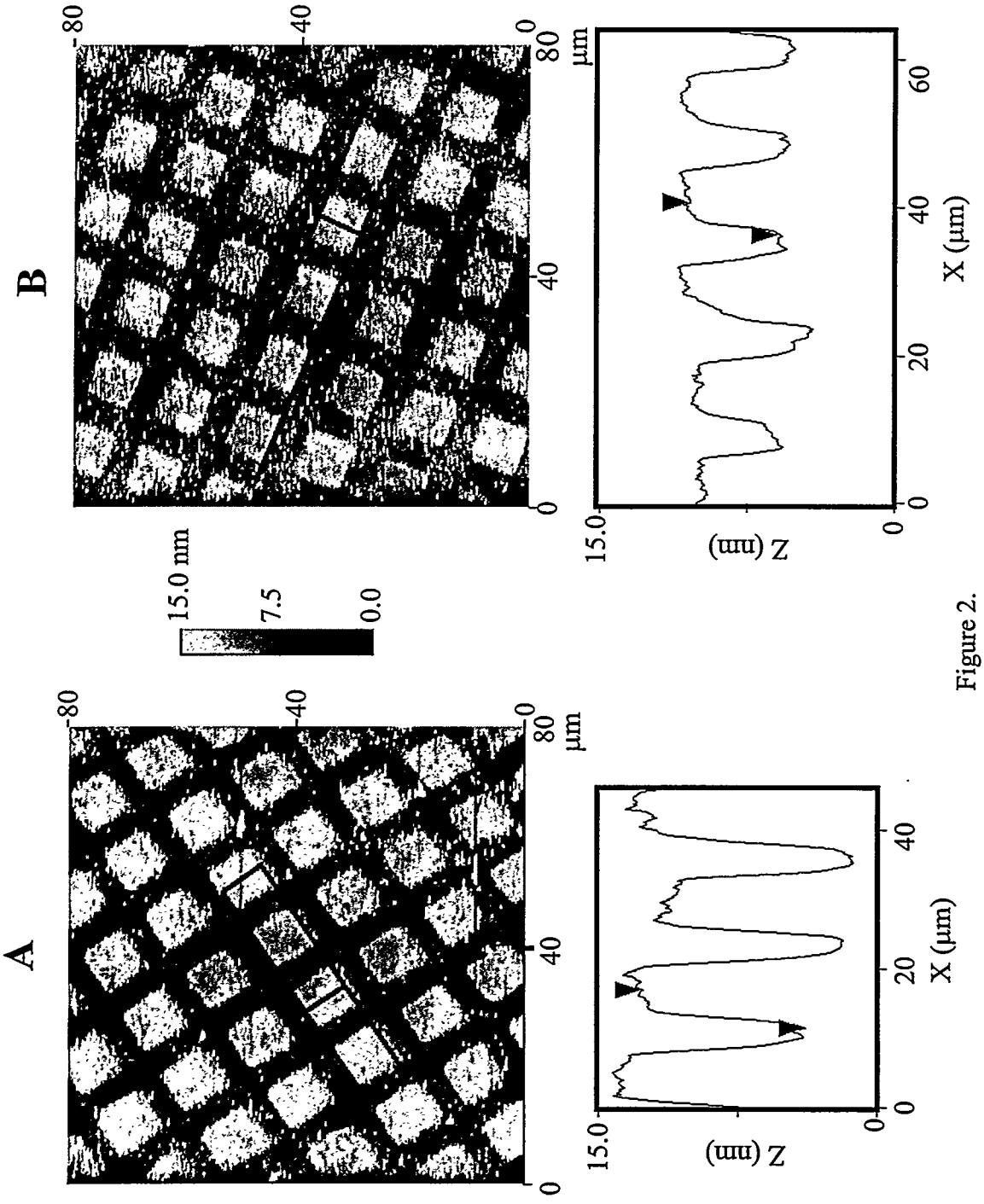

Figure 2.

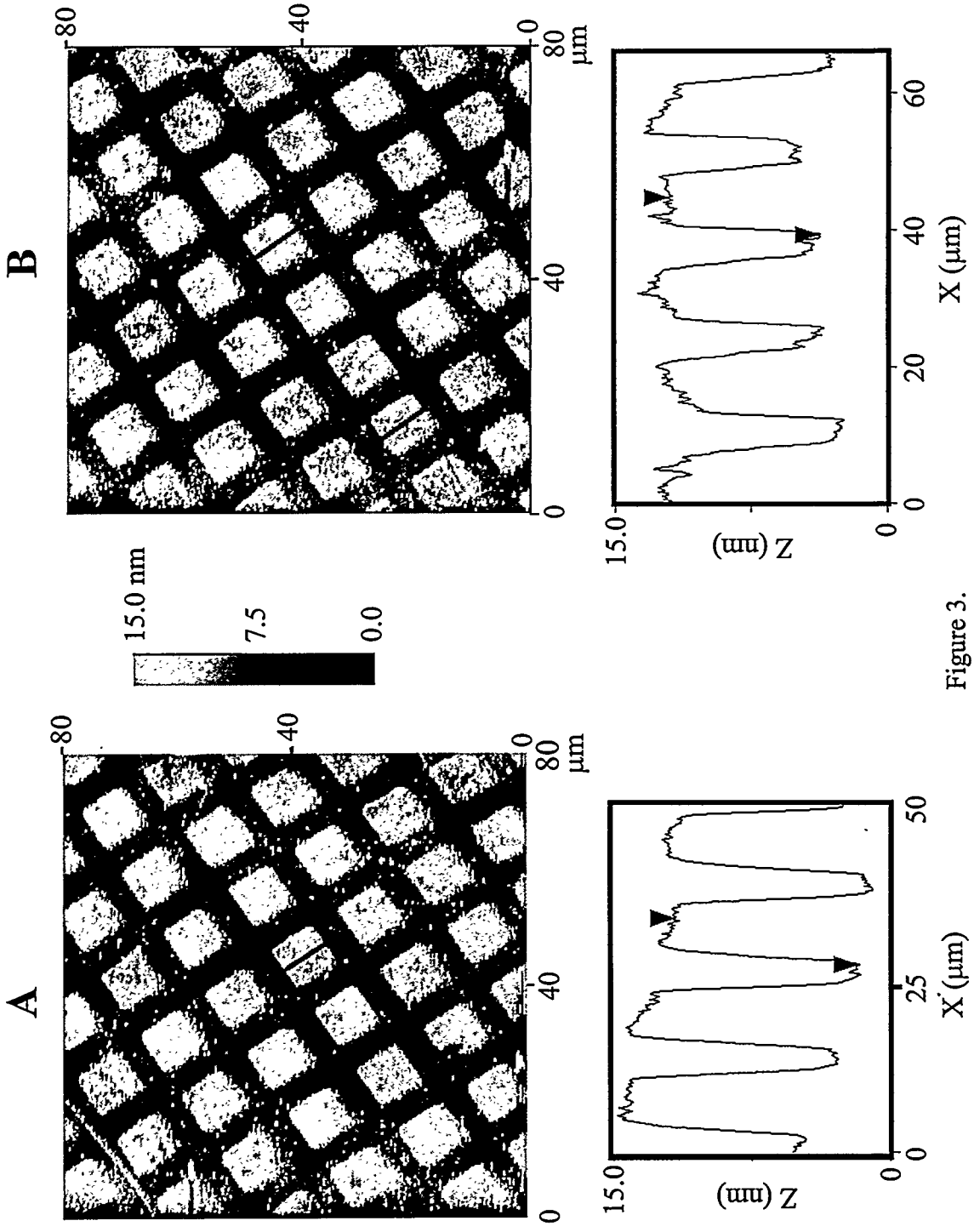

Figure 3.

CHAPTER 5. PREPARATION AND CHARACTERIZATION OF SELF-ASSEMBLED DOUBLE-STRANDED DNA (dsDNA) MICROARRAYS FOR PROTEIN:dsDNA SCREENING USING ATOMIC FORCE MICROSCOPY

A manuscript submitted to *Langmuir*

Janese C. O'Brien,[1] John T. Stickney,[2] and Marc D. Porter[1,3]

ABSTRACT

We report details on our development of a self-assembled, double-stranded DNA (dsDNA) microarray fabrication strategy suitable for protein:dsDNA screening using the atomic force microscope (AFM). Using disulfide-modified dsDNA (26-mer) synthesized using off-chip phosphoramidite chemistry to contain the recognition sequence for *ECo*R1, we have created micron-sized mixed monolayer surfaces where both the spatial orientation and packing density of the immobilized oligonucleotides, two critical parameters for screening protein:dsDNA interactions, are controlled. Before exposure to *ECo*R1, the topography of microarrays comprised of 26-mers containing the recognition sequence for *Eco*R1 was 8.8 nm ± 1.5 nm (n = 5), a value consistent with that predicted by X-ray diffraction studies. After enzyme digestion, the topography of the microarray decreased to 4.3 nm ± 0.8 nm (n = 14), a value consistent with predictions based on the position of the recognition sequence within the oligonucleotides. In contrast, the topography of microarrays comprised of 26-mers that did not contain the recognition sequence for *ECo*R1 remained essentially the same before (8.9 nm ± 1.5 nm (n=5)) and after (8.3 nm ± 1.4 nm (n=5)) exposure to *ECo*R1.

---

[1] Microanalytical Instrumentation Center, Ames Laboratory-DOE, and Department of Chemistry, Iowa State University, Ames, IA 50011
[2] Department of Biochemistry, Biophysics, and Molecular Biology, Iowa State University, Ames, IA 50011
[3] Corresponding author

Furthermore, because the dsDNA were synthesized to include a fluorescein moiety above the recognition sequence, the loss of fluorescence after exposure to *ECo*R1 was also used to detect enzymatic cleavage. We believe that this technology holds tremendous promise as a tool for the rapid and facile screening of multiple protein interactions using massively parallel dsDNA microarrays.

INTRODUCTION

Single-stranded DNA (ssDNA) microarrays have been used extensively as chip-scale platforms for interrogation of gene expression (1), polymorphism analysis (2), and mutation screening (3). Advancements in areas such as transcription, replication, and restriction enzyme engineering, however, require arrays of double-stranded DNA (dsDNA). Thus, approaches to construct dsDNA microarrays as well as to interrogate their sequence specific interactions are of major significance to many facets of biotechnology.

In a recent breakthrough investigation, Church and co-workers formed dsDNA microarrays by using enzymes to extend complimentary primers annealed to surface-immobilized ssDNA (4). Furthermore, enzymatic cleavage at a specific sequence within the immobilized dsDNA was demonstrated by monitoring the loss of a fluorescent label incorporated above the cleavage site. There are, however, two limitations to the overall accuracy of this fabrication strategy, both of which are related to the complications of on-chip synthesis. First, the average efficiencies of the most reliable method for on-chip single-stranded oligonucleotide synthesis (5, 6) are 92-94% per nucleotide (6). This level of efficiency can potentially compromise the construction of sequences for large n-mers (6, 7).

For example, only 4 - 9% of a 40-mer will be of the desired length and sequence. Second, adjacent strands of immobilized ssDNA can impede the transformation into dsDNA by sterically interfering with the action of extension enzymes and/or the annealing of template oligonucleotides. As a consequence, only a portion of the immobilized ssDNA may be converted to dsDNA (8). Steric effects may also reduce the effectiveness of any on-chip labeling (e.g., fluorescent tagging) process. Together, these limitations can potentially impact the effectiveness of an assay (8).

In a recent preliminary paper, we described a fabrication strategy for creating dsDNA microarrays (9) which draws on earlier work in constructing ssDNA surfaces (10, 11) and addresses these limitations. Our strategy combines the ease of self-assembled monolayer technology with the ability of the atomic force microscope (AFM) to detect changes in topography at subnanometer lengths scales. In this work, we extend the concept of an AFM height-based assay for the detection of specific antibody-antigen binding (12, 13) to the detection of changes in topography indicative of specific protein:dsDNA interactions. We also show that sequence-specific cleavage can be detected optically by positioning a fluorescent moiety at a position in the duplex above the cleavage site and monitoring the presence or absence of the optical signal as a function of enzyme exposure.

EXPERIMENTAL

A. Oligonucleotides. Thiol-Modifier C6 S-S and 5'-Fluorescein Phosphoramidite (6-FAM) were purchased from Glen Research and used in the synthesis of two sets of complimentary 26-mer oligonucleotides. These oligonucleotides were synthesized using an ABI 394 automated synthesizer at the Iowa State University DNA Sequencing and Synthesis

Facility via phosphoramidite chemistry to contain the disulfide modification on the 3'-end of one strand and on the 5'-end of the compliment strand (Fig. 1A,B). One complimentary pair of oligonucleotides contained the recognition sequence (in bold) for the *ECo*R1 restriction enzyme (Fig. 1A) and the other contained the recognition sequence (in bold) for the *Hae*III restriction enzyme (Fig. 1B). "T" was the "dummy" base used to make the 3'-modification. For cleavage experiments, a 5'-fluorescein functionality (designated as F*) was added to each oligonucleotide strand containing the 3'-disulfide group (Fig. 1A,B). Complimentary oligonucleotide strands were then annealed in deionized water by heating to 95 °C for 15 min and then cooling to room temperature for ~1 h. All samples were subsequently protected from light to minimize any optically-induced degradation of the fluorescently-labeled materials.

Based on X-ray diffraction studies, the predicted length of a 26-mer double-stranded oligonucleotide in its B-conformation is 8.8 nm (14). From the position of the *ECo*R1 recognition sequence within the oligonucleotides illustrated in Fig. 1A, exposure of arrays comprised of these oligonucleotides to *ECo*R1 should result in a topography decrease of 4.4 nm (Fig. 1C).

B. Reagents. 6-mercaptohexanol (MCH) was purchased from Fluka and used as received. *ECo*R1 was purchased from Promega. Stock solutions of enzyme reaction buffer (90 mM tris(hydroxymethyl)aminomethane (THAM) (pH 7.4), 10 mM $MgCl_2$, and 50 mM NaCl) were prepared in Millipore deionized water.

C. Gold Substrate Fabrication. Substrates were prepared using silicon wafers ((100) single crystals, Montco Silicon). The silicon substrates were cleaned in an ultrasonic bath for 30 min in water and for 30 min in methanol and then dried in a stream of high purity

argon (Air Products) and placed in a vacuum evaporator (Edwards High Vacuum Products). Next, the substrates were coated with 15 nm of chromium at 0.1 nm/s followed by 300 nm of gold (99.9%) at 0.3-0.4 nm/s. During coating, the pressure in the deposition chamber was ~8 x 10^{-6} Torr. The substrates were used either immediately upon removal from the evaporator or stored under dry nitrogen.

D. Monolayer Formation and Photopatterning. The five-step microarray fabrication process is summarized in Figure 2. The preparation of the compositionally patterned monolayers paralleled the process previously described (12). Step 1 involved the formation of a fluorinated monolayer by immersing the gold coated substrates in a 10 mM ethanolic solution of recrystallized ($SH(CH_2)_2(CF_2)_7CF_3$) for ~24 hr. These samples were then rinsed extensively with ethanol (Quantum, punctilious grade) and dried under a stream of argon.

Step 2 entailed the photopatterning process and followed guidelines previously described in the literature (15). The patterns were prepared by sandwiching carefully a copper transmission electron microscopy (TEM) grid (2000 mesh (hole size: 7.5 μm; bar size: 5.0 μm)) (Electron Microscopy Sciences) between the monolayer-coated sample and a quartz plate. A 200-watt, medium pressure mercury lamp (Oriel) was used as the light source. The beam was collimated, reflected off an air-cooled, dichroic mirror (220-260 nm), focused by a fused silica lens, and passed through the TEM grid before impinging on the sample for ~20 min. During this process, the irradiated gold-bound thiolates are converted to various forms of oxygenated sulfur (e.g. RSO_3^-) that are readily rinsed off the surface with most organic solvents (16). Immediately following irradiation, Step 3 entailed the extensive

rinsing of the surfaces with deionized water and ethanol and their subsequent drying under a stream of argon to expose square-shaped regions on the underlying gold.

E. DNA Array Fabrication. In Step 4, one nanomole of dsDNA was diluted with 30 μL of buffer and deposited onto substrates prepared in Step 3. Our most reliable results were obtained using 30 μL of 1 M THAM (pH 7.4) as the buffer (see Results and Discussion). The samples were then incubated in a humid environment at room temperature for 2 h. After incubation, samples were rinsed with copious amounts of deionized water and dried with argon. For enzyme cleavage experiments, dsDNA arrays were then exposed to 10 μM MCH in 1 M THAM (pH 7.4) containing 0.1 M $MgCl_2$ for various lengths of time. This step displaces a portion of the adsorbed dsDNA from the surface, reducing the duplex density and facilitating enzyme access to the recognition sequence. We note that a 1-h exposure appeared to maintain the height integrity of the array as well as allow enzymatic access to the recognition sequence (see Results and Discussion).

F. Enzyme Cleavage of Surface-Immobilized Oligonucleotides. The digestion media, which was prepared using 5 μL of *ECo*R1 (12 U/μL) diluted to 50 μL with enzyme reaction buffer, was placed on the immobilized oligonucleotide array. Arrays were incubated in a dark, humid environment for 20 h at room temperature. After digestion, samples were rinsed with copious amounts of deionized water and dried with argon. Next, 30 μL of 1 M THAM (pH 7.4) was placed on the array and incubated for 1 h. Given the sensitivity of oligonucleotide topography to ionic strength (see Results and Discussion), we found that this step was necessary to restore oligonucleotide topography to its original value after exposure to the rather low ionic strength of the enzyme reaction buffer. Samples were again rinsed with deionized water and dried with argon prior to imaging.

G. Instrumentation. ***(i).*** **Atomic Force Microscopy (AFM).** In situ tapping mode AFM experiments (10 mM THAM (pH 7.4)) were performed on a Nanoscope IIIa AFM (Digital Instruments) equipped with a 150 μm scanner. Oxide-sharpened Si_3N_4 cantilevers with a normal bending force constant of 0.06 N/m were used (Nanoprobes, Digital Instruments), with the set point amplitude of the cantilever maximized relative to its free space amplitude in order to minimize the force applied to the surface by the tip.

(ii). **X-ray Photoelectron Spectroscopy (XPS).** A Physical Electronics Industries 5500 surface system was used for XPS characterizations. This system is equipped with a hemispherical analyzer, toroidal monochromator, and multichannel detector. A pass energy of 29.35 eV was used with a resolution of ~0.3 eV. Monochromatic Al Kα radiation (1486.6 eV) at 300-W was used for excitation. Photoelectrons were collected at 45° from the surface normal, with a 5-min acquisition time for all samples. The Au($4f_{7/2}$) emission band served as an internal reference for binding energies. The base pressure of the XPS chamber was less than 9×10^{-10} Torr during all analyses, and the sampling area was ~2 mm^2. Spectral deconvolution in the S(2p) binding energy region used Gaussian profiles with a peak width constraint of 1.0 eV and a relative area ratio of 2:1 (($2p_{3/2}$):($2p_{1/2}$)) (17). Spectral deconvolution in the N(1s) binding energy region used a two-component Gaussian profile.

(iii). **Fluorescence Microscopy.** Fluorescence images were acquired using an Olympus BX50WI epi fluorescence microscope equipped with a SenSys 1400 digital camera (Photometrix) and a mercury bulb excitation source. All images were collected using an exciter filter (BP 470 nm – 480 nm), a dichromatic beamsplitter (DM 500 nm), and a bandpass barrier filter (BA 515 nm – 550 nm).

RESULTS AND DISCUSSION

Concept. To create double-stranded oligonucleotide microarrays suitable for protein:dsDNA screening, an immobilization strategy that controls the orientation and packing density of the oligonucleotides is essential. If the oligonucleotides are oriented such that access by the protein to the target sequence is hindered by the substrate, the performance of the assay may be compromised. Orientation is also important from an AFM read-out perspective. If oligonucleotides are immobilized on a surface with their long axis parallel to the substrate, the effectiveness of the topographic detection of several sequence-specific interactions could be reduced as well. A second critical issue when designing oligonucleotide microarrays for screening efforts is oligonucleotide packing density. If packed too closely, adjacent duplexes may sterically limit access of the protein to its target sequence. Addressing these issues is critical to the creation of arrays suitable for protein:dsDNA screening.

Our methodology for constructing dsDNA microarrays was developed to incorporate the above architectural attributes, and draws on concepts presented in our earlier reports on height-based immunoassays (12, 13) and on modifications to a strategy for the self-assembly of ssDNA onto gold (10, 11, 18). The methodology involves the direct deposition of double-stranded oligonucleotides (Fig. 1A,B) that were synthesized by exploiting off-chip phosphoramidite chemistry. The oligonucleotides were engineered to 1) contain asymmetrically substituted disulfide functionalities which direct their self-assembly onto gold in a single preparative step (19, 20), 2) include a recognition sequence that is specific to a given restriction enzyme, 3) position the recognition sequence within the duplex such that enzymatic cleavage will exhibit a topographic change readily detectable by AFM (Fig. 1C),

and 4) contain a fluorescent tag positioned above the recognition sequence to verify cleavage by optical microscopy. After exchange with a short chain thiol to reduce duplex density, either AFM or fluorescence microscopy can be used to detect oligonucleotide cleavage that results when a dsDNA array comprised of individual oligonucleotide addresses is exposed to a restriction enzyme that recognizes a specific palendromic sequence pre-engineered within the immobilized oligonucleotides (Fig. 1C).

The preparation of compositionally patterned microarrays on gold uses the five-step fabrication process shown in Figure 2. Briefly, Step 1 forms a thiol-derived ($CF_3(CF_2)_7(CH_2)_2SH$) fluorinated monolayer on gold. This portion of the adlayer serves, after photopatterning, as an internal reference plane for detection of topographic changes; its low surface free energy also minimizes complications from nonspecific adsorption (13). Step 2 is the photopatterning process. This process uses a metallic grid (hole size: 7.5 μm, grid size: 5.0 μm) as a lithographic mask. Irradiation of the sample converts the thiolate to various oxygenated forms of sulfur that are readily washed off the gold surface with most organic solvents (21). Step 3 removes the oxygenated adlayer by rinsing with copious amounts of ethanol. This procedure exposes square-shaped regions on the underlying gold that are subsequently modified in Step 4. Step 4 exposes the patterned surface to a dsDNA solution. This step coats the exposed regions of gold with a mixed monolayer through cleavage of the disulfide linkages (19, 20, 22) that were covalently attached to both duplex strands by off-chip phosphoramidite synthesis (23). Step 5 exchanges a portion of immobilized dsDNA with a short chain alkanethiol (i.e., $HO(CH_2)_6SH$, (MCH). This step reduces duplex density, a key factor in increasing enzymatic accessibility to specific recognition sequences within individual addresses.

Effect of Deposition Conditions. Having already established the reliability of Steps 1-3 (Fig. 2) in previous reports on the preparation of antigenic arrays (12, 13), we began by examining the factors that affect the architecture produced in Step 4 (Fig. 2), i.e., the deposition of dsDNA onto the array elements exposed in Step 3. As discussed, oligonucleotide orientation and packing density are critical from both a protein:dsDNA interaction perspective and from a topographic read-out perspective and as such, we first sought to identify the conditions necessary to achieve the desired oligonucleotide architecture. Guided by the earlier findings of Herne and Tarlov regarding the assembly of ssDNA adlayers as a function of the ionic strength of the assembly solution (10), Figure 3 presents a series of images that illustrate the effect of deposition solution on the vertical extension of the dsDNA adsorbates. The images are composed of a pattern of topographic differences consistent with the expectations of the photolithographic process, noting that the presence of the alkanethiolate monolayer in the grids that surround each address serves as an internal height reference plane.

When dsDNA was deposited in 1 M THAM (pH 7.4) (Fig. 3A), a difference between the squares and grids of 6.8 nm was measured, a value less than the 8.8 nm predicted for a 26-mer by X-ray crystallography (14). Because Mg^{2+} induces conformational changes in dsDNA (24) and is also a required co-factor for the restriction enzyme used in this study (25), we also added 0.1 M $MgCl_2$ to 1 M THAM (pH 7.4) to determine if higher topography could be obtained. However, the addition of 0.1 M $MgCl_2$ produced arrays of slightly reduced topography, 5.2 nm (Fig. 3B). We note that oligonucleotide deposition in 1 M KH_2PO_4 (pH 3.8), conditions similar to that initially reported by others (10, 11) for the successful immobilization of thiol-modified ssDNA onto gold, produced arrays with a height

difference between the squares and grids of only 1.3 nm (Fig. 3C). Furthermore, arrays deposited in deionized water showed little, if any, detectably measurable topographic differences (data not shown), possibly due to a low level of dsDNA adsorption and/or an absorbed orientation not amenable for topographic detection. The former explanation is supported by a report that found that the surface coverage of ssDNA onto gold was strongly dependent upon the ionic strength of the deposition solution (10).

We tested several other dsDNA modification strategies to determine if further improvements in topographic difference could be obtained. In one such series of experiments, we examined the topography of arrays comprised of double-stranded oligonucleotides in which only one strand of the duplex contained the disulfide modifier. Heights of these arrays were consistently lower than those constructed with dsDNA containing the disulfide modification on both strands of the duplex. For example, heights of 2.4 nm, 0.6 nm, and 0.4 nm were determined for surfaces deposited from 1 M THAM (pH 7.4), 1 M KH_2PO_4 (pH 3.8), and deionized water, respectively (data not shown).

We also explored the use of arrays prepared using a procedure similar to that of Herne and Tarlov (10). These experiments employed dsDNA in which only one strand of the duplex contained the disulfide modification. We treated these oligonucleotides with dithiothreitol to cleave the disulfide within the modifier by its reduction to a thiol and then passed the dithiothreitol-dsDNA mixture over a size-exclusion column (Nap 10, Sephadex G-25 DNA grade, Pharmacia Biotech) to remove the portion of the modifier reduced from the duplex as well as excess reducing agent. Next, the resulting thiol-modified dsDNA was placed onto compositionally-patterned surfaces created in Step 3 (Fig. 2). Surfaces were then exposed to 1 mM 6-mercaptohexanol (MCH) in deionized water, the rationale for this step

being that oligonucleotide displacement by MCH promotes a more perpendicular orientation of the remaining ssDNA (10) by reducing nonspecific contacts between the dsDNA backbone and the gold surface (18).

The topography of dsDNA microarrays formed in this manner was actually lower than that measured prior to MCH treatment (data not shown). It is unclear if the very low ionic strength of the MCH solution played a part in the measured topographic decrease, given the sensitivity of the oligonucleotides to solution ionic strength as illustrated earlier, or if a significant amount of dsDNA was displaced from the surface by MCH, making topographic detection difficult. Nevertheless, we determined that the approach used successfully for ssDNA immobilization by Herne and Tarlov was not effective for constructing dsDNA microarrays amenable to topographic detection. In all subsequent experiments, we used the first array fabrication method, i.e. deposition of dsDNA containing the disulfide modification on both strands in 1 M THAM (pH 7.4) (Fig. 3A).

Compositional Verification. To characterize the surface composition of gold modified with a dsDNA adlayer, characterizations using XPS were conducted. Figure 4 presents the S(2p) (A) and N(1s) (B) binding energy regions for bare gold modified with an adlayer of dsDNA formed under the buffer conditions illustrated in Fig. 3A and containing the disulfide modification on both strands. The S(2p) region (Fig. 4A) displays a single doublet (i.e., $2p_{3/2}$ and $2p_{1/2}$) that arises from spin-orbit coupling (17) and signals the presence of only one form of sulfur in the adlayer. Moreover, the position of the doublet (163.1 eV ($2p_{1/2}$) and 161.9 eV ($2p_{3/2}$) is consistent with sulfur as thiolate (26), the form of sulfur expected after the self-assembly of disulfides on gold (20, 22, 27). In contrast, the N(1s) region (Fig. 4B) displays a single feature centered at 400.9 eV. The feature contains a hint of

broadening on the low-energy side, suggesting the presence of two chemically distinct forms of nitrogen in the adlayer. We attribute this to the presence of nitrogen in two chemical forms, i.e., as $-NH_2$, which gives rise to the feature centered at 399.3 eV, and as heterocyclic aromatic amines, which gives arise to the feature centered at 400.8 eV, as predicted by examination of DNA nucleotide structure.

Optimizing dsDNA Array Density. Adlayers created in the single deposition step illustrated in Fig. 3A could not be cleaved by *ECo*R1 under any experimental conditions attempted. We attribute the lack of cleavage to duplex density. The size of the *ECo*R1-dsDNA complex is ~5 nm (14) and we believe that duplexes created in the manner illustrated in Fig. 3A are too dense, inhibiting enzymatic access to the recognition sequence.

To reduce duplex density such that enzymatic access is enhanced and yet the integrity of the microarray is preserved for topographic detection of cleavage, we adopted a two-step approach for creating dsDNA microarrays. After Step 4 in Fig. 2, we exposed the arrays to a dilute solution of MCH for various lengths of time, i.e., Step 5 in Fig. 2. As shown by others with single-stranded oligonucleotides immobilized on gold (10), we speculated that such treatment would displace a portion of adsorbed dsDNA and create a lower duplex density, thereby facilitating enzymatic access to the recognition sequence.

Because dsDNA is the only species involved in microarray fabrication that contains nitrogen, examination of the nitrogen signal by XPS was used to evaluate the amount of dsDNA on the surface. Figure 5 examines Step 5 (Fig. 2) of the array fabrication process and shows the normalized XPS N(1s) peak area for a series of dsDNA microarrays plotted as a function of exposure to 10 μM MCH in 1 M THAM (pH 7.4) containing 0.1 M $MgCl_2$. As evident, the N(1s) signal decreases as a function of immersion time in MCH, reaching a near

constant level after ~6 h. Even modest exposure times (15 min) to such a dilute solution displaced a measurable amount of dsDNA. We found that a 1 h exposure, where ~40% of dsDNA initially deposited onto the microarray was removed, was optimal for our experiments. Under these conditions, the topography of individual dsDNA addresses within the array was consistent with that based on crystallographic predictions for a double-stranded 26-mer (8.8 nm). This finding suggests that oligonucleotide displacement by MCH promoted a more perpendicular orientation of the remaining dsDNA, perhaps due to a reduction of electronic repulsion between adjacent highly negatively charged duplexes (10).

Given the diameter of a dsDNA duplex (~2 nm) (14), the van der Waals diameter of an alkanethiol (0.42 nm) (28), and the ratio of 2:1 alkanethiolate molecules:dsDNA duplex before MCH treatment (arising from the use of the disulfide modifier on both duplex strands), we estimate the coverage of dsDNA on the surface to be 2.9×10^{13} duplexes/cm^2 and 1.8×10^{13} duplexes/cm^2 before and after a 1 hr exposure to 10 μM MCH (1 M THAM (pH 7.4), 0.1 M $MgCl_2$), respectively. This estimate assumes a closest-pack monolayer that adopts an orientation perpendicular to the substrate. Additional structural investigations are necessary in order to refine this rough estimate further.

We note that a topography consistent with the crystallographic prediction (8.8 nm) was only achieved when MCH displacement was performed in 1 M THAM (pH 7.4), 0.1 M $MgCl_2$, suggesting that ionic strength plays a role in oligonucleotide displacement. When exposed to 10 μM MCH in deionized water for 1 h, the topography diminished from that observed prior to MCH exposure (~6 nm) to ~2 nm. In an important observation, we note that the height of an array treated in this manner could be restored to its height measured before MCH treatment (~6 nm) by exposure to 1 M THAM (pH 7.4) for 1 h. This finding

suggests that the transient reduction in topography was most likely not due to severe dsDNA displacement but, rather, to the low ionic strength of the MCH solution.

We believe the observed dependence of microarray topography on ionic strength reflects the highly charged nature of DNA at the experimental pH. We theorize that solutions of high ionic strength may be required to shield the strongly negatively-charged phosphate backbone of dsDNA from adjacent duplexes. This electrostatic shielding may allow neighboring duplexes to form a denser monolayer than that formed in the absence of counterions, thereby allowing dsDNA to adopt a more perpendicular orientation on the gold substrate. When exposed to low ionic strength conditions, we suspect that electrostatic repulsion between adjacent phosphate backbones dominates, disrupting the orientation of the oligonucleotides and compromising the height of the array. This finding concurs with our previous observations regarding array fabrication (see previous section).

***ECo*R1 Cleavage of Surface-Immobilized Oligonucleotides.** Figure 6A shows an AFM topographic image for an array formed from the double-stranded 26-mer containing a recognition sequence specific for the enzyme *ECo*R1 (Fig. 1A) after exposure to 10 μM MCH (1 M THAM (pH 7.4), 0.1 M $MgCl_2$). The 8.8 ± 1.5 nm (n=5) difference in height between grid and square regions agrees with the X-ray crystallographic prediction of 8.8 nm for a double-stranded 26-mer in its B-conformation (14). This result demonstrates that after MCH displacement, our approach effectively immobilizes dsDNA with its strands extending along the surface normal. Figure 6B shows an image for an array after digestion with *ECo*R1. Importantly, the difference in height between dsDNA addresses and the reference adlayer has decreased to 4.3 ± 0.8 nm (n=14). This difference is consistent with the prediction based on the position of the recognition sequence (Fig. 1A,C). It also agrees with

the topographic difference found after the self-assembly of the products produced from off-chip solution digestion (data not shown).

Figure 7 presents the results of a control experiment. These images were acquired for an array comprised of double-stranded 26-mers prepared in the same fashion as those in Figure 6 except that the dsDNA contained a recognition sequence specific for the restriction enzyme *Hae*III. The heights before (8.9 nm ± 1.5 nm (n=5)) and after (8.3 nm ± 1.4 nm (n=5)) exposure to *ECo*R1 are effectively indistinguishable. This confirms that the enzymatic cleavage of immobilized dsDNA observed in Fig. 6 is the result of specific protein:dsDNA interactions and not the result of nonspecific enzymatic activity.

To confirm enzyme cleavage, fluorescence microscopy was used. Because the fluorescent label is positioned above the recognition sequence (Fig. 1A,B), the presence or absence of the fluorophore can be used to confirm enzymatic cleavage. Figure 8A shows the fluorescence image of a dsDNA microarray containing the recognition sequence for *Hae*III after incubation with *ECo*R1. As evident, the image is composed of a defined fluorescent pattern of 7.5 μm squares that are surrounded by nonfluorescent 5 μm-wide grids. This result indicates that dsDNA immobilized in the square regions of the microarray is intact and has not been cleaved by *ECo*R1. Figure 8B is the fluorescent image obtained from an array comprised of dsDNA containing the recognition sequence for *ECo*R1 specific DNA after incubation with *ECo*R1. The image only hints at the presence of a fluorescent pattern, indicating the loss of the fluorescent label after enzyme exposure. Taken with the AFM topography data, the fluorescence interrogation of the oligonucleotide arrays confirms the specific cleavage of surface immobilized oligonucleotides by *ECo*R1.

CONCLUSIONS AND FUTURE WORK

We have successfully constructed a dsDNA microarray fabrication scheme suitable for protein:dsDNA screening using the atomic force microscope. Using disulfide-modified dsDNA (26-mer) containing the recognition sequence for *ECo*R1 plus alkanethiol molecules used to adjust array density, we have created micron-sized mixed monolayer surfaces where both oligonucleotide orientation and packing density, two critical parameters for enzymatic access and cleavage of the immobilized oligonucleotides, are controlled. AFM investigations reveal that the pH and ionic strength of the deposition solution, as well as the degree of disulfide modification on the oligonucleotides, greatly affects the measured topography of the array. After exposure to *ECo*R1, the height of arrays comprised of oligonucleotides containing the *ECo*R1 restriction sequence was approximately half of that measured on arrays containing oligonucleotides that did not have the recognition sequence. Furthermore, the disappearance of the fluorescein label upstream of the recognition sequence was used to confirm enzymatic cleavage of the target dsDNA microarray. We believe this technology holds tremendous promise as a tool for the rapid and facile screening of multiple protein interactions using massively parallel dsDNA microarrays. Experiments that explore issues of array density, digestion time minimization, and fabrication of smaller, uniquely addressed elements are underway.

ACKNOWLEDGEMENTS

We express our appreciation to James Anderegg for the XPS characterizations as well as to Gary Polking and the staff at the Iowa State University DNA Sequencing and Synthesis Facility for their assistance with oligonucleotide synthesis. We also acknowledge Jennifer

Harnisch for synthesizing the fluorinated monolayer and Jeremy R. Kenseth for insightful discussions. This work was supported in part by the National Science Foundation (Grant No. BIR-9601789), the Microanalytical Instrumentation, and the Office of Basic Energy Science, Chemical Sciences Division of the U.S. Department of Energy. The Ames Laboratory is operated for the U.S. Department of Energy by Iowa State University under Contract W-7405-eng-82.

REFERENCES

(1) Bassett, Jr. D. E.; Eisen, M. B.; Boguski, M. S. *Nat. Genet.* **1999,** *21 (Suppl)*, 51.

(2) Wang, K.; Gan, L.; Jeffery, E.; Gayle, M.; Gown, A. M.; Skelly, M.; Nelson, P. S.; Ng, W. V.; Schummer, M.; Hood, L.; Mulligan, J. *Gene* **1999,** *229*, 101.

(3) Hacia, J. G. *Nat. Genet.* **1999,** *21 (Suppl)*, 42.

(4) Bulyk, M. L.; Gentalen, E.; Lockhart, D. J.; Church, G. M. *Nat. Biotechnol.* **1999,** *17*, 573.

(5) Fodor, S. P. A.; Read, J. L.; Pirrung, M. C.; Stryer, L.; Lu, A. T.; Solas, D. *Science* **1991,** *251*, 767.

(6) McGall, G. H.; Barone, A. D.; Diggelmann, M.; Fodor, S. P. A.; Gentalen, E.; Ngo, N. *J. Am. Chem. Soc.* **1997,** *119*, 5081.

(7) Southern, E.; Mir, K.; Shchepinov, M. *Nat. Genet.* **1999,** *21 (Suppl)*, 5.

(8) Carlson, R.; Brent, R. *Nat. Biotechnol.* **1999,** *17*, 536.

(9) O'Brien, J. C.; Stickney, J. T.; Porter, M. D. *J. Am. Chem. Soc.*, in press.

(10) Herne, T. M.; Tarlov, M. J. *J. Am. Chem. Soc.* **1997,** *119*, 8916.

(11) Peterlinz, K. A.; Georgiadis, R. M.; Herne, T. M.; Tarlov, M. J. *J. Am. Chem. Soc.* **1997,** *119*, 3401.

(12) Jones, V. W.; Kenseth, J. R.; Porter, M. D.; Mosher, C. L.; Henderson, E. *Anal. Chem.* **1998,** *70*, 1233.

(13) O'Brien, J. C.; Jones, V. W.; Porter, M. D.; Mosher, C. L.; Henderson, E. *Anal. Chem.* **2000,** *72*, 703.

(14) Voet, D.; Voet, J. G. In *Biochemistry*; John Wiley and Sons, Inc.: New York, 1995, p 853.

(15) Tarlov, M. J.; Burgess, Jr. D. R. F.; Gillen, G. *J. Am. Chem. Soc.* **1993,** *115*, 5305.

(16) Lewis, M.; Tarlov, M.; Carron, K. *J. Am. Chem. Soc.* **1995,** *117*, 9574.

(17) Castner, D. G.; Hinds, K.; Grainger, D. W. *Langmuir* **1996,** *12*, 5083.

(18) Levicky, R.; Herne, T. M.; Tarlov, M. J.; Satija, S. K. *J. Am. Chem. Soc.* **1998,** *120*, 9787.

(19) Nuzzo, R. G.; Zegarski, B. R.; Dubois, L. H. *J. Am. Chem. Soc.* **1987,** *109*, 733.

(20) Biebuyck, H. A.; Whitesides, G. M. *Langmuir* **1993,** *9*, 1766.

(21) Lewis, M.; Tarlov, M.; Carron, K. *J. Am. Chem. Soc.* **1995,** *117*, 9574.

(22) Nuzzo, R. G.; Fusco, F. A.; Allara, D. L. *J. Am. Chem. Soc.* **1987,** *109*, 2358.

(23) Brown, T.; Brown, D. J. S. In *Oligonucleotides and Analogues: A Practical Approach*; Eckstein, F., Ed.; IRL Press: Oxford, 1991, p 1.

(24) Yokota, H.; Johnson, F.; Lu, H.; Robinson, R. M.; Belu, A. M.; Garrison, M. D.; Ratner, B. D.; Trask, B. J.; Miller, D. L. *Nucleic Acids Res.* **1997,** *25*, 1064.

(25) Rosenberg, J. M.; McClarin, J. A.; Frederick, C. A.; Grable, J.; Boyer, H. W.; Greene, P. J. *Gene Amplif. Anal.* **1987,** *5*, 119.

(26) Walczak, M. M.; Alves, C. A.; Lamp, B. D.; Porter, M. D. *J. Electroanal. Chem.* **1995,** *396*, 103.

(27) Ishida, T.; Yamamoto, S.; Mizutani, W.; Motomatsu, M.; Tokumoto, H.; Hokari, H.; Azehara, H.; Fujihara, M. *Langmuir* **1997,** *13*, 3261.

(28) Ulman, A.; Eilers, J. E.; Tillman, N. *Langmuir* **1989**, 1147.

FIGURE CAPTIONS

Figure 1. Self-assembling double-stranded DNA (dsDNA) suitable for AFM-based screening. Disulfide-modified double-stranded 26-mer containing the recognition sequence (in bold) specific for cleavage by *ECo*R1 (A) or *Hae*III (B) were synthesized using standard phosphoramidite chemistry. X-ray crystallography predicts the lengths of 8.8 nm and 4.4 nm for the intact and cleaved oligonucleotides in their B-conformation (14), respectively. Oligonucleotides used in cleavage experiments were labeled with fluorescein (F*) at the 5'-end (i.e., above the recognition sequence) for use in an optical verification of sequence specific cleavage. The "T" indicated on end of the 3'-disulfide-modified oligonucleotide was the "dummy base" used to make the 3'-modification. C. Conceptualized topographic change after exposure of a surface-immobilized dsDNA microarray containing the oligonucleotides illustrated in (A) to *ECo*R1.

Figure 2. Schematic of the five-step array fabrication process. Solution-annealed, double-stranded 26-mer oligonucleotides containing the recognition sequence for *ECo*R1 (Fig. 1A) or *Hae*III (Fig. 1B) are deposited onto the square-shaped addresses formed after Step 3 (see Experimental section). When exposed to gold, the disulfides cleave

and chemisorb as thiolates to create the densely-packed, two-component monolayer depicted by a portion of an array element below Step 4. Step 5 creates dsDNA microarrays suitable for screening efforts and adjusts the density and orientation of the immobilized oligonucleotides by displacing a portion of dsDNA with 6-mercaptohexanol (MCH) to facilitate enzymatic access to the immobilized oligonucleotides. This process is depicted conceptually by a small segment of an array element below Step 5.

Figure 3. Effect of deposition conditions on the topography of dsDNA microarrays. dsDNA (1 nmol) was diluted with 30 μL of (A) 1 M THAM (pH 7.4), (B) 1 M THAM (pH 7.4), 0.1 M $MgCl_2$, or (C) 1 M KH_2PO_4 (pH 3.8), placed on a compositionally-patterned array created after Step 3 (Fig. 2), and allowed to react for 2 h at room temperature. Surfaces were then rinsed extensively with deionized water and dried with argon prior to imaging.

Figure 4. XPS characterizations in the S(2p) (A) and N(1s) (B) binding energy regions for bare gold modified with an adlayer of dsDNA containing the disulfide modification on both strands. The adlayer was formed in 1 M THAM (pH 7.4). Restricted deconvolution of the S(2p) doublet and the N(1s) envelope was performed using the parameters described in the Experimental section.

Figure 5. Normalized N(1s) XPS signal for dsDNA microarrays as a function of exposure to 10 μM 6-mercaptohexanol (MCH) in 1 M THAM (pH 7.4), 0.1 M $MgCl_2$.

Figure 6. In situ AFM topographic images (80 μm x 80 μm) of a dsDNA microarray containing the recognition sequence specific for *ECo*R1 (Fig. 1A). The images were collected before (A) and after (B) digestion with *ECo*R1. The cross-sectional

contours below each image reflect the average of the individual scan lines contained in the area of a single row of the array. The in situ images were obtained in 10 mM THAM (pH 7.4) at a scan rate of 1 Hz.

Figure 7. In situ AFM topographic images (80 μm x 80 μm) of a dsDNA microarray containing the recognition sequence specific for *Hae*III (Fig. 1B). The images were collected before (A) and after (B) digestion with *ECo*R1. The cross-sectional analysis found below each image was performed by averaging the individual scan lines contained in the area of a single row of the array. The images were obtained in 10 mM THAM (pH 7.4) at a scan rate of 1 Hz.

Figure 8. Fluorescence images (125 μm x 125 μm) of dsDNA microarray containing the recognition sequence specific for (A) *Hae*III or (B) *ECo*R1 after incubation with *ECo*R1. The images were obtained under deionized water.

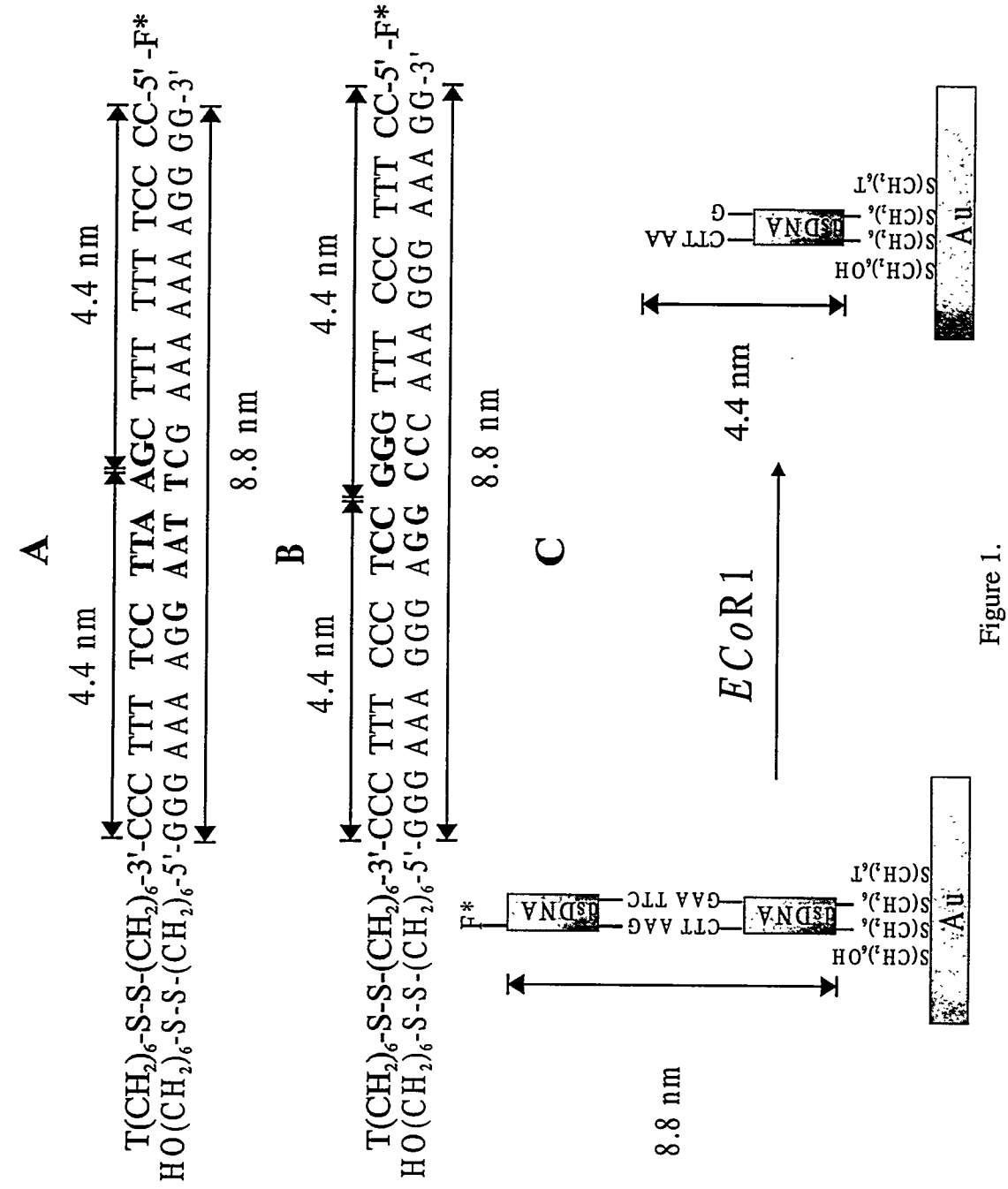
A
4.4 nm
4.4 nm
8.8 nm
T(CH2)6-S-S-(CH2)6-3'-CCC TTT TCC TTA AGC TTT TTT TCC CC-5' -F*
HO(CH2)6-S-S-(CH2)6-5'-GGG AAA AGG AAT TCG AAA AAA AGG GG-3'
B
4.4 nm
4.4 nm
8.8 nm
T(CH2)6-S-S-(CH2)6-3'-CCC TTT CCC TCC GGG TTT CCC TTT CC-5' -F*
HO(CH2)6-S-S-(CH2)6-5'-GGG AAA GGG AGG CCC AAA GGG AAA GG-3'
C
F*
dsDNA
GAA TTC
CTT AAG
dsDNA
S(CH2)6OH
S(CH2)6
S(CH2)6
S(CH2)6T
Au
8.8 nm
EcoR1
4.4 nm
CTT AA
G
dsDNA
S(CH2)6OH
S(CH2)6
S(CH2)6
S(CH2)6T
Au

Figure 1.

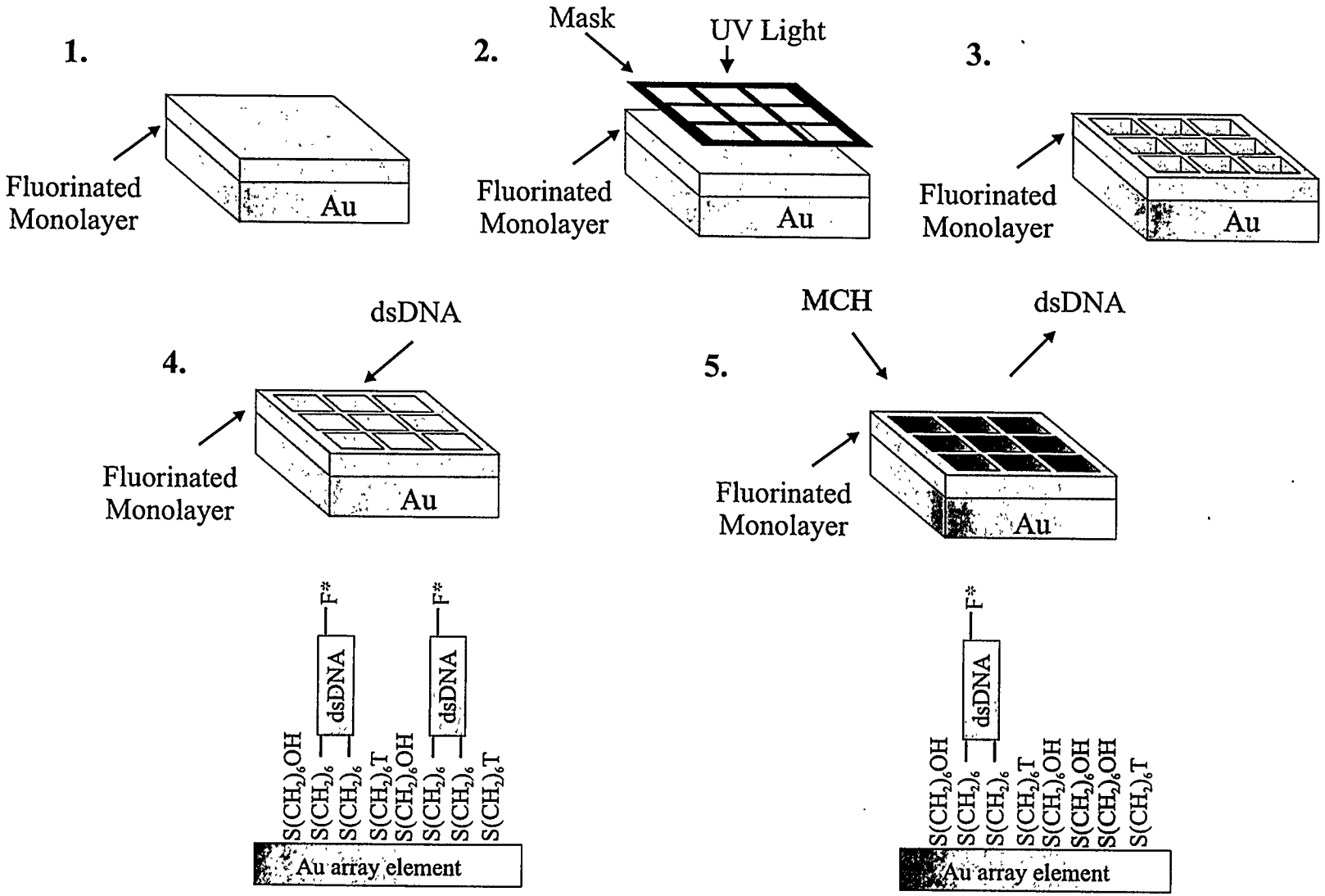
1.
Fluorinated Monolayer
Au
2.
Mask
UV Light
Fluorinated Monolayer
Au
3.
Fluorinated Monolayer
Au
4.
dsDNA
Fluorinated Monolayer
Au
F*
dsDNA
S(CH2)6OH
S(CH2)6
S(CH2)6T
Au array element
5.
MCH
dsDNA
Fluorinated Monolayer
Au
F*
dsDNA
S(CH2)6OH
S(CH2)6T
Au array element

Figure 2.

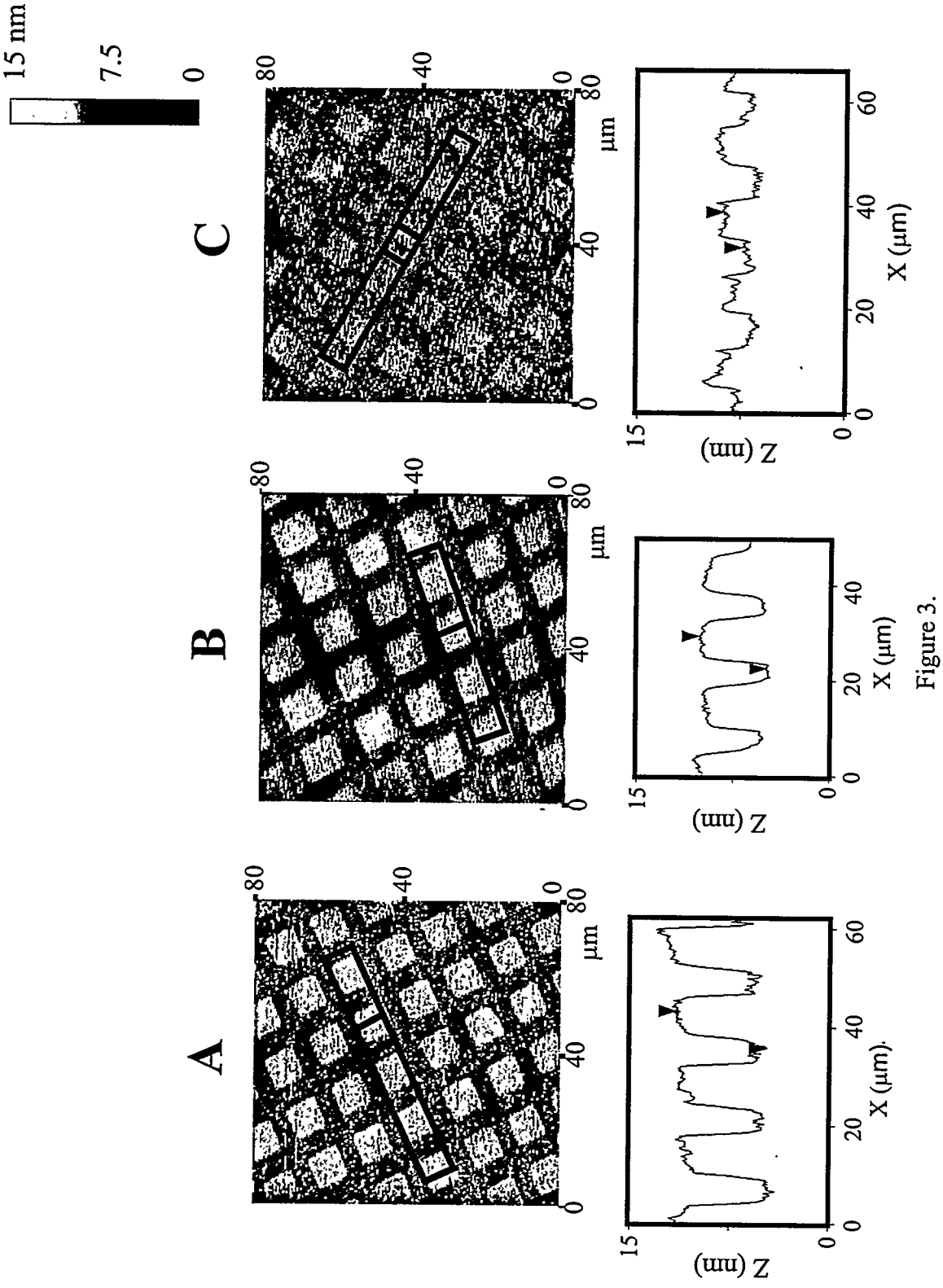

Figure 3.

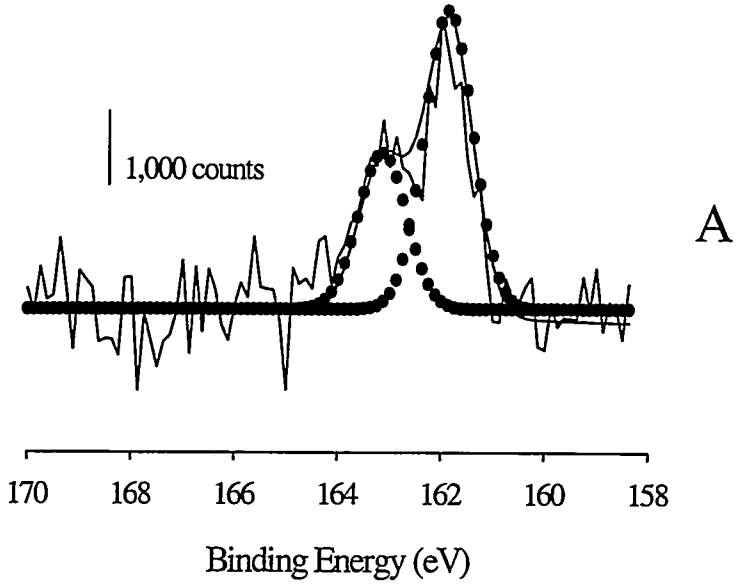
1,000 counts
A
170
168
166
164
162
160
158
Binding Energy (eV)

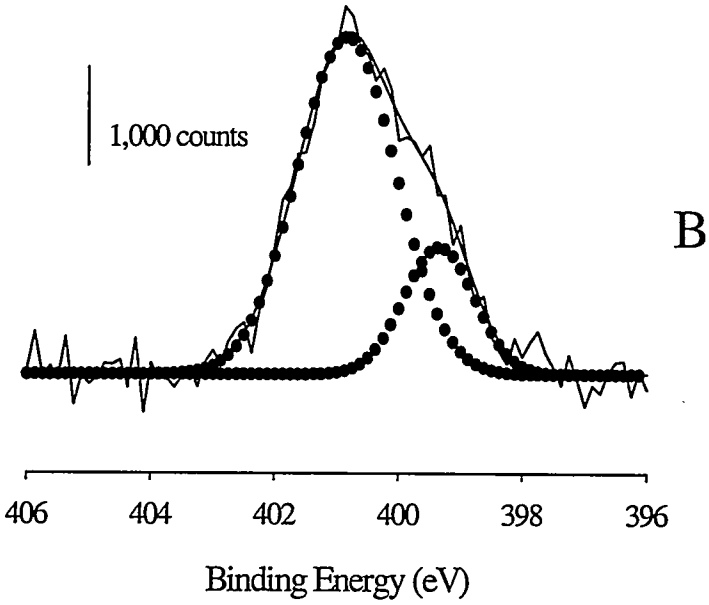
1,000 counts
B
406
404
402
400
398
396
Binding Energy (eV)

Figure 4.

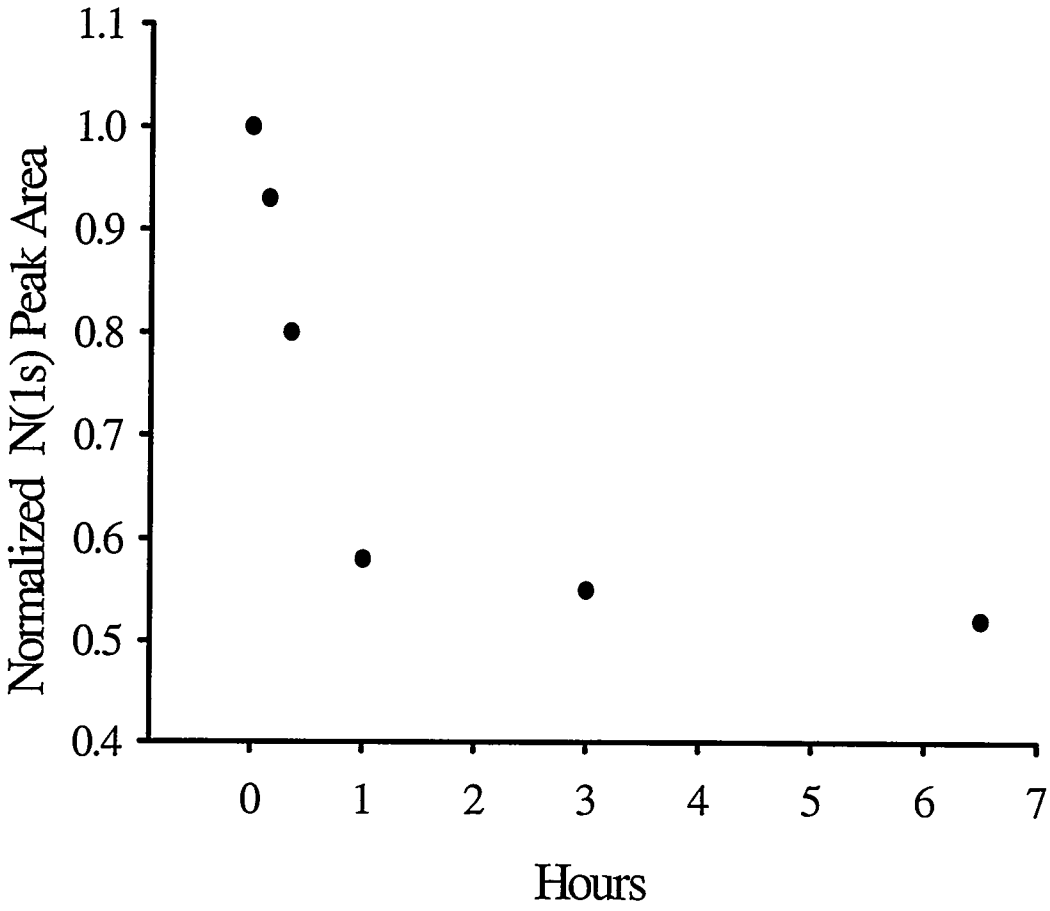
1.1
1.0
0.9
0.8
0.7
0.6
0.5
0.4
Normalized N(1s) Peak Area
0
1
2
3
4
5
6
7
Hours

Figure 5.

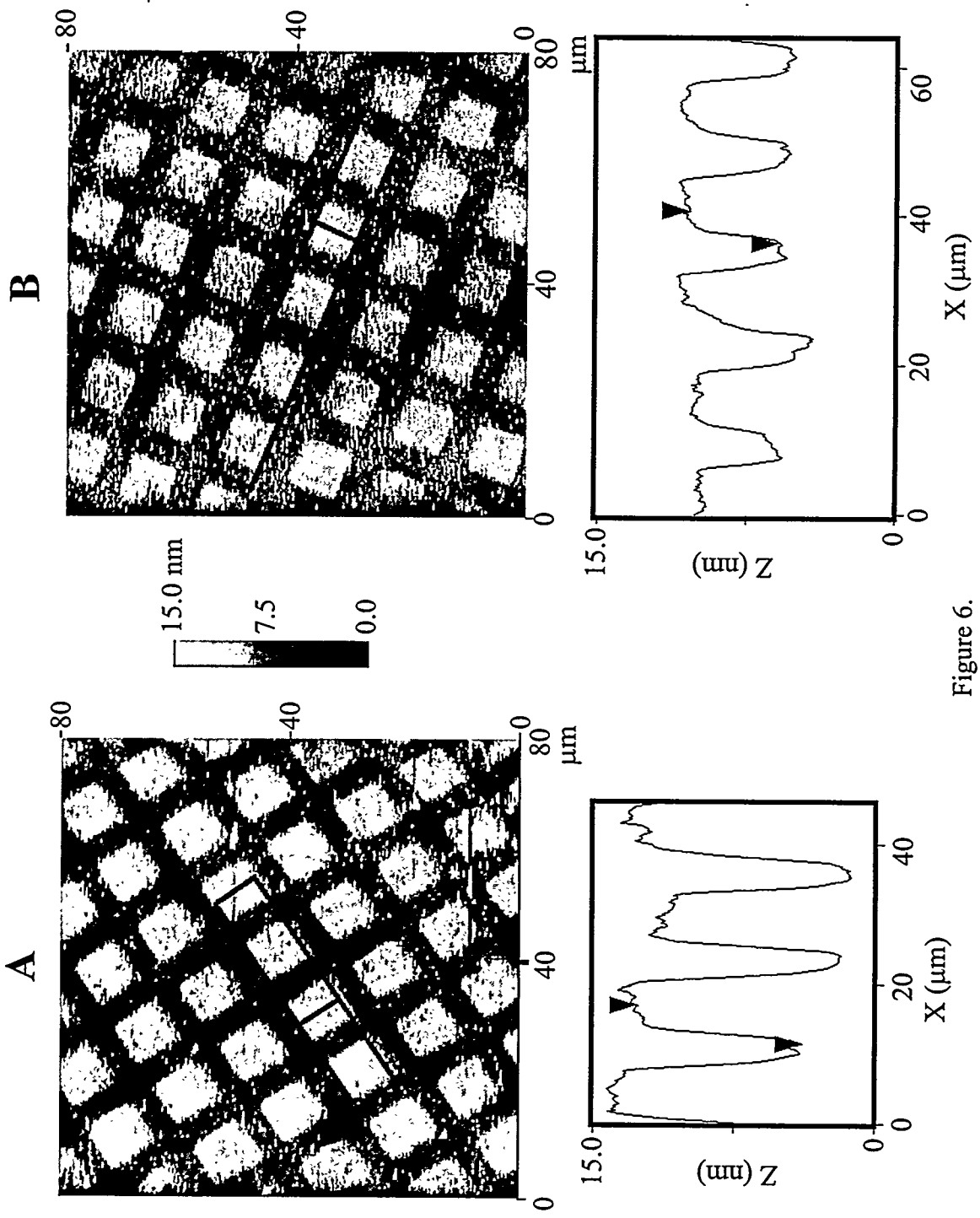

Figure 6.

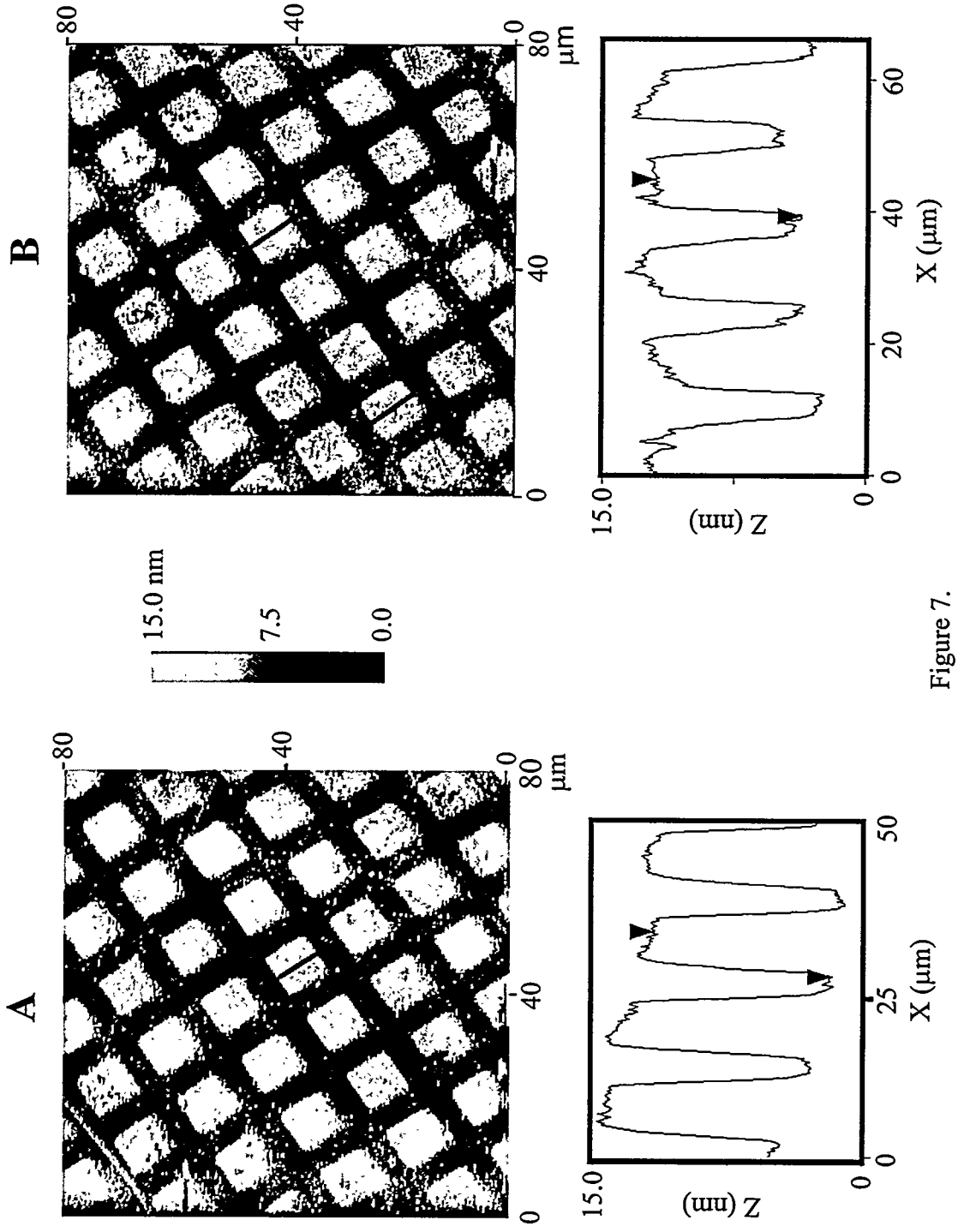

Figure 7.

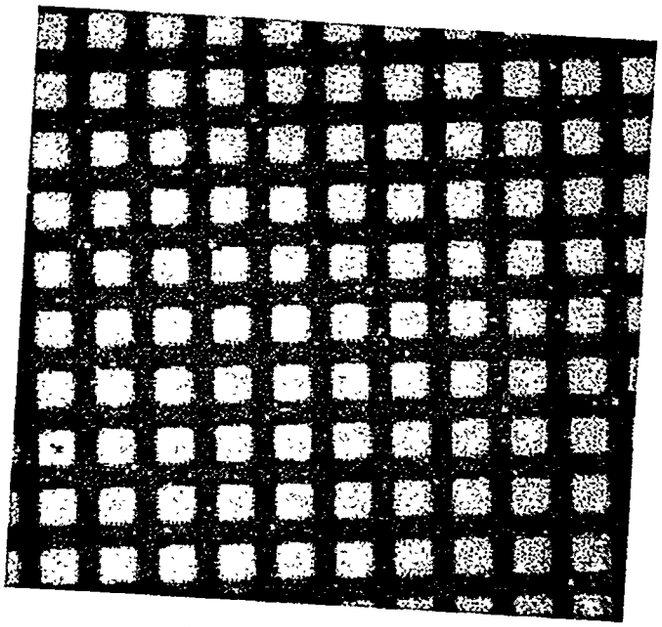

A

50 μm

B

50 μm

Figure 8.

CHAPTER 6. GENERAL CONCLUSIONS AND FUTURE PROSPECTUS

The work presented in this dissertation represents some of analytical chemistry's cross-disciplinary efforts within the areas of materials science and biology. In the area of materials science, Chapter 2 described the synthesis and characterization of electrically conductive sol-gel materials derived from the acid-catalyzed hydrolysis of a vanadium alkoxide. Specifically, this chapter investigated the effect of the acidic and drying conditions used during synthesis on conductivity and reported that the conductivity of vanadium sol-gels could be enhanced ~100,000 times by manipulating these two parameters.

In the area of biology, Chapters 3-5 described the fabrication of novel biological platforms suitable for topographic investigation by the scanning force microscope (SFM), also known as the atomic force microscope (AFM). Specifically, Chapter 3 described the construction of novel antigenic immunosensing platforms using spontaneously adsorbed antibody fragments on gold. Here, immunosurfaces constructed by the spontaneous adsorption of rabbit Fab'-SH on gold contained ~4 times as many intact epitopes per square centimeter as surfaces constructed from the spontaneous adsorption of whole molecule IgG. Epitope density is critical to the early detection of disease and, as such, surfaces that display increased epitope density may prove valuable for diagnostic screening efforts.

Perhaps the most notable work contained in this dissertation is that found in Chapters 4 and 5. Chapter 4 introduced a novel fabrication scheme for creating self-assembled double-stranded DNA (dsDNA) microarrays suitable for protein:dsDNA screening using the atomic force microscope. Chapter 5 explored this strategy and characterized more fully the preparation of these microarrays. Such work expands existing microarray fabrication

technologies by utilizing higher efficiency synthesis strategies and relying solely on molecular self-assembly. We believe that this advancement may lead to more cost-effective strategies for microarray mass production efforts as well as reduce the overall cost of the fabrication process, thereby potentially enabling researchers to make significant inroads in the areas of genomics, expression analysis, and protein engineering.

While Chapters 4-5 represent a novel development in the area of dsDNA microarray fabrication technology, significant work is yet to be done. Perhaps the most important future work in this area is expansion of the fabrication scheme to permit independent addressing of individual elements within the array. More specifically, schemes which allow the placement of different dsDNA probes with varying sequences on adjacent regions of the surface is necessary if this technology is to be useful from a high-throughput screening perspective.

Once approach that may prove useful is to localize the oxidation chemistry used currently to create our arrays. The light source used in Chapters 4-5, a mercury bulb, irradiates several square millimeters of substrate. When using a transmission electron microscopy (TEM) grid as a mask and after rinsing in the appropriate solvent, multiple bare gold regions are created and, consequently, are modified by the same probe. Localization of the oxidative process would potentially create only one bare gold region that would then be modified by the desired probe. Such localization could be achieved without the use of masks by using a UV laser capable of irradiating only small regions of a surface. After deposition of the dsDNA probe, the laser could then irradiate an adjacent region that could be subsequently modified with a second probe. Such selective irradiation could be accomplished either by rastering the laser beam across an alkanethiol-modified surface or using arrays of micromirrors to reflect laser light to the desired region of the surface.

Multiple cycles of irradiation followed by deposition would create an array with different dsDNA probes on adjacent regions of the surface.

Future work can also be done in the area of modifier chemistry. The disulfide modifier used in Chapters 4-5 directs duplex self-assembly onto gold via thiolate bond formation and creates a mixed monolayer surface in a single preparative step. Future changes in the structure of the modifier could be done to include, for example, a moiety to minimize nonspecific adsorption of proteins onto areas separating duplex addresses. In another approach, the modifier could be engineered to contain a metal colloid or magnetic particle whereby the properties of the metallic label (size, magnetic susceptibility, etc) serve as a label to identify the adjacent oligonucleotide sequence. This would eliminate the need for individual element addressing as well as enable non-AFM-based read-out methodologies.

Similarly, advances in detection technology will undoubtedly compliment future advances in array fabrication and modifier design. Furthermore, advances in the areas of laser spectroscopy and magnetism may also lead to new microarray read-out schemes, such as fluorescence or magnetics, that may prove more sensitive and cost-effective than AFM-based detection. Advances in these areas and others will surely move forward the field of microarray fabrication and miniaturized analytical detection.

This work was performed at Ames Laboratory under contract no. W-7405-Eng-82 with the U. S. Department of Energy. The United States Government has assigned the DOE Report Number IS-T 1904 to this thesis.